

**Automatic near real-time flood detection in high resolution
X-band synthetic aperture radar satellite data using
context-based classification on irregular graphs**

Dissertation
der Fakultät für Geowissenschaften
der Ludwig-Maximilians-Universität München



Sandro Martinis

Eingereicht am: 15.09.2010

1. Gutachter: Prof. Dr. Ralf Ludwig
2. Gutachter: Prof. Dr. Richard Bamler

Tag der Disputation: 06.12.2010

Abstract

This thesis is an outcome of the project “Flood and damage assessment using very high resolution SAR data” (SAR-HQ), which is embedded in the interdisciplinary oriented RIMAX (Risk Management of Extreme Flood Events) programme, funded by the Federal Ministry of Education and Research (BMBF). It comprises the results of three scientific papers on automatic near real-time flood detection in high resolution X-band synthetic aperture radar (SAR) satellite data for operational rapid mapping activities in terms of disaster and crisis-management support.

Flood situations seem to become more frequent and destructive in many regions of the world. A rising awareness of the availability of satellite based cartographic information has led to an increase in requests to corresponding mapping services to support civil-protection and relief organizations with disaster-related mapping and analysis activities. Due to the rising number of satellite systems with high revisit frequencies, a strengthened pool of SAR data is available during operational flood mapping activities. This offers the possibility to observe the whole extent of even large-scale flood events and their spatio-temporal evolution, but also calls for computationally efficient and automatic flood detection methods, which should drastically reduce the user input required by an active image interpreter.

This thesis provides solutions for the near real-time derivation of detailed flood parameters such as flood extent, flood-related backscatter changes as well as flood classification probabilities from the new generation of high resolution X-band SAR satellite imagery in a completely unsupervised way. These data are, in comparison to images from conventional medium-resolution SAR sensors, characterized by an increased intra-class and decreased inter-class variability due to the reduced mixed pixel phenomenon. This problem is addressed by utilizing multi-contextual models on irregular hierarchical graphs, which consider that semantic image information is less represented in single pixels but in homogeneous image objects and their mutual relation. A hybrid Markov random field (MRF) model is developed, which integrates scale-dependent as well as spatio-temporal contextual information into the classification process by combining hierarchical causal Markov image modeling on automatically generated irregular hierarchical graphs with noncausal Markov modeling related to planar MRFs. This model is initialized in an unsupervised manner by an automatic tile-based thresholding approach, which solves the flood detection problem in large-size SAR data with small *a priori* class probabilities by statistical parameterization of local bi-modal class-conditional density functions in a time efficient manner.

Experiments performed on TerraSAR-X StripMap data of Southwest England and ScanSAR data of north-eastern Namibia during large-scale flooding show the effectiveness of the proposed methods in terms of classification accuracy, computational performance, and transferability. It is further demonstrated that hierarchical causal Markov models such as hierarchical maximum *a posteriori* (HMAP) and hierarchical marginal posterior mode (HMPM) estimation can be effectively used for modeling the inter-spatial context of X-band SAR data in terms of flood and change detection purposes. Although the HMPM estimator is computationally more demanding than the HMAP estimator, it is found to be more suitable in terms of classification accuracy. Further, it offers the possibility to compute marginal posterior entropy-based confidence maps, which are used for the generation of flood possibility maps that express the uncertainty in labeling of each image element. The supplementary integration of intra-spatial and, optionally, temporal contextual information into the Markov model results in a reduction of classification errors. It is observed that the application of the hybrid multi-contextual Markov model on irregular graphs is able to enhance classification results in comparison to modeling on regular structures of quadrees, which is the hierarchical representation of images usually used in MRF-based image analysis.

X-band SAR systems are generally not suited for detecting flooding under dense vegetation canopies such as forests due to the low capability of the X-band signal to penetrate into media. Within this thesis a method is proposed for the automatic derivation of flood areas beneath shrubs and grasses from TerraSAR-X data. Furthermore, an approach is developed, which combines high resolution topographic information with multi-scale image segmentation to enhance the mapping accuracy in areas consisting of flooded vegetation and anthropogenic objects as well as to remove non-water look-alike areas.

Contents

List of figures	I
List of tables	II
List of acronyms	III
1 Introduction	1
1.1 Motivation.....	1
1.2 Objectives.....	6
1.3 Structure.....	7
2 Synthetic Aperture Radar.....	8
2.1 Basic principles and properties of imaging radar systems.....	8
2.1.1 Basic principles of imaging radar systems	8
2.1.2 Resolution in range.....	9
2.1.3 Resolution in azimuth.....	9
2.2 SAR Signal.....	11
2.2.1 Radar equation.....	11
2.2.2 System specific properties	12
2.2.3 Object specific properties	13
2.2.4 Speckle effect.....	15
2.3 Geometric effects	15
2.4 TerraSAR-X.....	16
3 Interaction between SAR signal and water bodies	18
3.1 Smooth open water.....	18
3.2 Rough open water	20
3.3 Flooded vegetation.....	22
3.4 Floods in urban areas	25
4 State of the art in SAR-based water detection	27

5 Publications	34
5.1 Paper 1.....	34
5.2 Paper 2.....	47
5.3 Paper 3.....	61
6 Summary and outlook.....	81
References	86
Acknowledgments.....	99
Curriculum Vitae	100

List of figures

Fig. 1: Number of natural disasters reported 1900-2009 (EM-DAT 2010, modified).	2
Fig. 2: Launch of civil spaceborne SAR missions since 1978 in dependance of system's wavelength (based on Lillesand et al. 2004).	5
Fig. 3: a) Imaging geometry of a spaceborne SAR sensor; b) Principle of SAR systems. Targets on the ground are less frequently viewed at near range than in far range. Therefore, point A has a proportional shorter effective antenna length L_A than B (L_B) and C (L_C).	10
Fig. 4: Radar reflection of a) smooth, b) moderately roughened and c) strongly roughened surfaces (Lillesand et al. 2004, modified).	13
Fig. 5: Effects of terrain relief on SAR images (Lillesand et al. 2004, modified).	16
Fig. 6: Scattering mechanisms of water and land surfaces under different conditions as well as specular and diffuse components of surface scattered radiation as a function of incidence angle and surface roughness.	18
Fig. 7: Separability of classes water (left populations) and land (right populations) in histograms of TerraSAR-X StripMap data in dependance of polarization: HH vs. VV polarization on a a) smooth and b) slightly roughened water surface, c) HH vs. HV and d) VV vs. VH polarization on a smooth water surface.	20
Fig. 8: Fourier spectral components of a rough water surface and resonant Bragg scattering (Elachi 1988, modified).	21
Fig. 9: Conceptual illustration of the major sources of backscatter from vegetation (Kasischke et al. 1997 and Lang et al. 2008, modified) and effect of flooded vegetation on X- and L-band SAR (Ormsby et al. 1985, modified).	23
Fig. 10: Relative radar return responses for different wavelengths and flooded vegetation types (Ormsby et al. 1985, modified).	24
Fig. 11: Layover (AL) and shadow (SB) areas in a flooded street (AB) between adjacent buildings as well specular reflection from water surfaces (R) and double bounce effects between roads and buildings in flooded (C_1C_2) and non-flooded (C_3C_4) conditions (Mason et al. 2010, modified).	26

List of tables

Tab. 1: Flood statistics for the years 1900-1980, 1981-1990, 1991-2000, and 2001-2010, global and in Europe. In this database only flood disasters are listed which fulfil at least one of the following criteria: 10 or more people reported killed, 100 people reported affected, a call for international assistance, declaration of a state of emergency (EM-DAT 2010).....	3
Tab. 2: Parameters of SpotLight (SL) and High-resolution SpotLight (HS) modes.	17
Tab. 3: Parameters of StripMap (SM) and ScanSAR (SC) modes.....	17

List of acronyms

Acronym Description

ACM	Active Contour Model
ATB-CD	Automatic Tile-based Change Detection
ALOS	Advanced Land Observation Satellite
ANN	Artificial Neural Network
ASAR	Advanced Synthetic Aperture Radar
BMBF	Bundesministerium für Bildung und Forschung (Federal Ministry of Education and Research)
CNES	Centre National d'Etudes Spatiales (National Centre of Space Research)
CNN	Cable News Network
CRED	Centre for Research of the Epidemiology of Disasters
CRF	Conditional Random Fields
DEM	Digital Elevation Model
DLR	Deutsches Zentrum für Luft- und Raumfahrt (German Aerospace Center)
DN	Digital Number
DRF	Discriminative Random Fields
DRK	Deutsches Rotes Kreuz (German Red Cross)
DSM	Digital Surface Model
EM	Expectation-maximization
ENVISAT	Environmental Satellite
ERS	European Remote Sensing
ESA	European Space Agency
FAR	False Alarm Rate
FNEA	Fractal Net Evolution Approach
FP	Flood Possibility
GG	Generalized Gaussian
GIS	Geographic Information Systems
GM	Global Minimum
HMAP	Hierarchical Maximum a Posteriori
HMC	Hidden Markov Chain
HMPM	Hierarchical Marginal Posterior Mode
HS	High-resolution SpotLight
ICM	Iterated Conditional Modes
IPCC	Intergovernmental Panel on Climate Change
JERS	Japanese Earth Resources Satellite
JPM	Joint Probability Mask
KI	Kittler and Illingworth
LAI	Leaf Area Index
LIDAR	Light Detection and Ranging

LULC	Land Use/Land Cover
MAP	Maximum a Posteriori
MDR	Missed Detection Rate
ML	Maximum Likelihood
MRF	Markov Random Field
NCI	Normalized Change Index
NRT	Near Real-time
OER	Overall Error Rate
PCC	Post-Classification Comparison
PDF	Probability Density Function
PFV	Potentially Flooded Vegetation
PRF	Pulse Repetition Frequency
QI	Quality Index
RADAR	Radio Detection and Ranging
RAR	Real Aperture Radar
RIMAX	Risk Management of Extreme Flood Events
SAR	Synthetic Aperture Radar
SBA	Split-based Approach
SC	ScanSAR
SETES	SAR End-To-End Simulator
SIR	Spaceborne Imaging Radar
SL	SpotLight
SM	StripMap
SNR	Signal to Noise Ratio
SOM	Self-organizing Maps
SRTM	Shuttle Radar Topography Mission
TPM	Transition Probability Mask
THW	Technisches Hilfswerk (German Federal Agency for Technical Relief)
ZKI	Zentrum für satellitengestützte Krisensinformation (Center for Satellite Based Crisis Information)

1 Introduction

1.1 Motivation

The demand for crisis information on natural disasters, humanitarian emergency situations and civil endangerment has substantially increased during recent years worldwide (Voigt et al. 2007). For this reason, the European Space Agency (ESA) and the National Centre of Space Research (CNES) of France initiated the International Charter “Space and Major Disasters” at the UNISPACE III conference in 1999, a consensus of major space agencies and civilian governmental satellite operators providing remotely sensed data in terms of natural, humanitarian and technical disasters. A rising awareness of the availability of satellite based cartographic information has led to an increase in requests to corresponding mapping services such as the Center for Satellite Based Crisis Information (ZKI) of the German Aerospace Center (DLR) to support civil-protection and relief organizations with disaster-related mapping and analysis.

Flood is not only one of the most wide spread natural disasters, which regularly causes large numbers of casualties with rising economic loss, extensive homelessness and disaster-induced disease, but is also the most frequent disaster type (Fig. 1). In 2009, ~43 % of all natural disasters worldwide were related to flooding (Vos et al. 2010). Comparable figures show the statistics of the International Charter “Space and Major Disaster” where ~46 % of the total number of activations (current as of August 19, 2010) are related to flood situations.

Floods may have many different origins. By definition, flood is “...the temporary covering by water of land normally not covered by water. This shall include floods from rivers, mountain torrents, Mediterranean ephemeral water courses, and floods from the sea in coastal areas, and may exclude floods from sewerage systems” (EC 2007, pp. 29). Flooding is a complex phenomenon that can result from multiple mechanisms, such as intense and/or longlasting rainfall, snowmelt, dike or dam break, reduced conveyance due to ice jams or landsliding, or glacial lake outbursts (Kundzewicz 2008). River flooding strongly depends on antecedent conditions of rivers and their catchment areas; i.e. soil-moisture, presence of snow and ice, the degree of soil sealing, and existence of dikes, dams and storage reservoirs (IPCC, 2007a). Estuary flooding can be caused by storm surges (Kundzewicz 2008).

Flood situations seem to become more frequent (Fig. 1) and destructive in many regions of the world (e.g. Berz 2001, Milly et al. 2002, Kundzewicz 2008). According to the Centre for Research of the Epidemiology of Disasters (CRED), inundations affected nearly one

billion people in the decade 2001-2010 globally (Tab. 1) and resulted in estimated damages of about 142 billion US\$ through the destruction of houses, infrastructure, crop- and livestock, etc. Even if the number of affected people as well as economic losses decreased both at about 40 % within 2001-2010 in comparison to the previous decade 1991-2000, the number of flood events increased by ~65 %. Within the 20-year period 1991-2010, the number of flood events more than doubled, the number of affected people nearly tripled and the damage multiplied by a factor of more than seven in comparison to the 91-year period 1900-1990 (Tab. 1). Within the period 1900-1990, ~9.2 % of the worldwide flood events occurred in Europe. This proportion significantly increased within the decades 1991-2000 (~15.2 %) and 2001-2010 (~13.1 %).

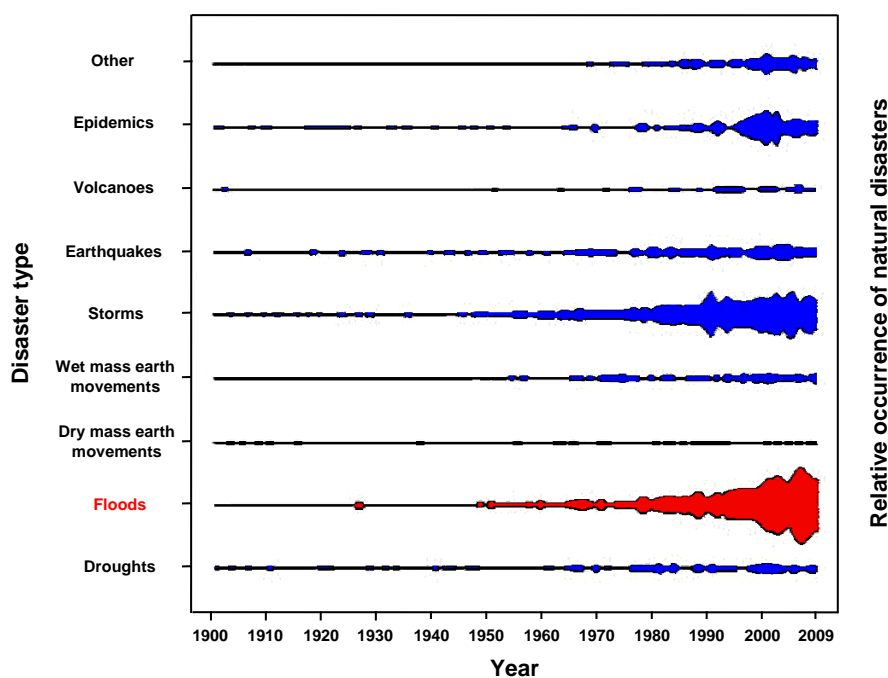


Fig. 1: Number of natural disasters reported 1900-2009 (EM-DAT 2010, modified).

The opinion exists that these upward trends are related to a so called “CNN (Cable News Network) effect” caused by a higher coverage in the media. Nevertheless, the worldwide flood risk and vulnerability is indeed on the rise, influenced by changes coupled to climate, terrestrial and socio-economic effects (Kundzewicz 2008). According to IPCC (2001, pp. 395), “the most widespread serious potential impact of climate change on human settlements is believed to be flooding”. Although a significant climate-related trend in extreme river flows has not yet been observed (EEA 2008), global warming is projected to intensify the hydrological cycle. As the atmosphere’s water holding capacity increases with temperature, the intensified potential for extreme precipitation events augments the risk of

inundations caused by sustained rainfall over most land areas (IPCC 2007b), especially in areas where flooding is typically triggered by intense summer rain (Kundzewicz 2005).

Tab. 1: Flood statistics for the years 1900-1980, 1981-1990, 1991-2000, and 2001-2010, global and in Europe. In this database only flood disasters are listed which fulfil at least one of the following criteria: 10 or more people reported killed, 100 people reported affected, a call for international assistance, declaration of a state of emergency (EM-DAT 2010).

Period	Nr. of events		Nr. of affected people		Damage (in 1 000 US\$)	
	World	Europe	World	Europe	World	Europe
1900-1980	581	53	407 380 734	594 454	2 496 946	658 250
1981-1990	546	51	469 855 416	839 522	46 648 071	10 482 300
1991-2000	966	147	1 463 420 671	4 679 707	233 075 277	41 674 964
2001-2010	1 592	209	874 495 941	3 205 507	141 949 993	41 793 882

On the other side, decreases in snow and river-ice cover reduce the frequency and severity of snowmelt-related and ice-jam floods (e.g. Mudelsee et al. 2003, Brázdil et al. 2006, Cyberski et al. 2006, Kundzewicz 2008). However, flood hazard will probably increase during wetter and warmer winters with more frequent rain and less frequent snow (Palmer & Räisänen 2002). Flash floods and urban flooding, caused by local extreme rainfall events, are also likely to be more frequent (Christensen & Christensen 2003, Kundzewicz et al. 2006).

A significant portion of the increase in flood hazards can be related to non-climatic anthropogenic factors. These include land-use changes such as deforestation, urbanization, elimination of floodplains and wetlands as well as river regularizations (e.g. Kundzewicz & Schellnhuber 2004), which lead to a reduction in water storage and infiltration capacity and an increasing runoff coefficient (Schumann et al. 2007).

Since future flood risks will be intensified by a steady population growth causing rising numbers of human settlements and economic assets within flood-prone areas, flood disaster management is of particular social, economic and political interest. It involves the assessment of vulnerability and risk, which focus on prevention, protection and preparedness, the monitoring of hazard prone zones, the planning and management of rescue operations and post disaster damage assessment (EC 2007).

Floods often cover large regions, which are difficult to access from the ground. Spaceborne remote sensing data are a well-suited information source to obtain a synoptic view about large-scale flood situations and their spatio-temporal evolution in a time- and cost-efficient manner, especially for regions where hydrological information is difficult to obtain due to inaccessibility or sparse distribution of gauging stations (Solbø & Solheim 2004). Satellite based flood extent maps can thus be a critical means for an effective flood disaster

management by supporting political decision makers and humanitarian relief organizations (Voigt et al. 2007) such as German Red Cross (DRK) or German Federal Agency for Technical Relief (THW). Further, they provide valuable distributed calibration and validation data for hydraulic models of river flow processes (e.g. Bates et al. 1995, Bates et al. 1997, Horritt 2000, Aronica et al. 2002, Matgen et al. 2004, Hunter 2005, Horritt 2006, Schumann et al. 2006, Pappenberger et al. 2007, Schumann et al. 2009, Hostache et al. 2009) and support the derivation of spatially accurate hazard maps in terms of flood prevention activities, insurance risk management, and area planning (e.g. De Moel et al. 2009).

Optical satellite imagery have been successfully used in the past to derive inundation areas (e.g. Blasco et al. 1992, Smith 1997, Wang et al. 2002, Van der Sande 2003, Ahtonen et al. 2004, Brakenridge & Anderson 2005) and, if available, they are the preferred data for flood mapping due to their straightforward interpretability and rich information content. As flooding often occurs during long-lasting precipitation and persistent cloud cover periods, in many cases a systematic monitoring by optical imaging instruments is prohibit. This fact drastically decreases the regular usability of optical sensors in an operational rapid mapping context. This is particularly an obstacle in small- to medium-sized drainage basins where inundations often recede before meteorological conditions improve (Schumann et al. 2007). Synthetic Aperture Radar (SAR) systems offer some clear advantage compared to sensors operating in the visible, infrared or thermal range of the electromagnetic spectrum: Being an active monostatic instrument and therefore providing its own source of illumination in the microwave range, it is characterized by near all-weather/day-night acquisition capabilities as the radar signal is able to penetrate clouds and the imaging process is independent from solar radiation. Thus, each acquired image can be used for flood detection. The radar sensor capabilities strongly enhance the monitoring frequency and therefore the real-time utilization for emergency situations, as the Earth's surface can be observed in a repetitive manner within each overpass, both in ascending and descending orbit. Further, SAR has proven to be an effective tool for detecting flooding beneath vegetation canopies in certain conditions (e.g. Richards et al. 1987, Hess et al. 1990, Townsend 2002, Kasischke et al. 2003).

Over the last years, spaceborne SAR systems (Fig. 2) have increasingly been used for mapping flood extent. While past and current medium-resolution SAR satellite and space shuttle radar missions have a proven track-record for large-scale flood mapping in the X- (SIR-C/X-SAR, SRTM), C- (ERS-1/2 AMI, Envisat ASAR, RADARSAT-1/2, SIR-C/X-SAR), and L-band domain (SEASAT-1, JERS-1, ALOS PALSAR, SIR-A/B/C/X-SAR), their potential for deriving flood parameters in complex and small-scaled scenarios is clearly

limited. Since 2007, the successful launch of the European polar orbiting platforms TerraSAR-X, three COSMO-SkyMed satellites and actually TanDEM-X (Fig. 2) marks a new generation of X-band SAR systems suitable for flood monitoring purposes. These satellites provide data up to the one meter pixel spacing class, permitting an operational derivation of detailed hydrological parameters from space.

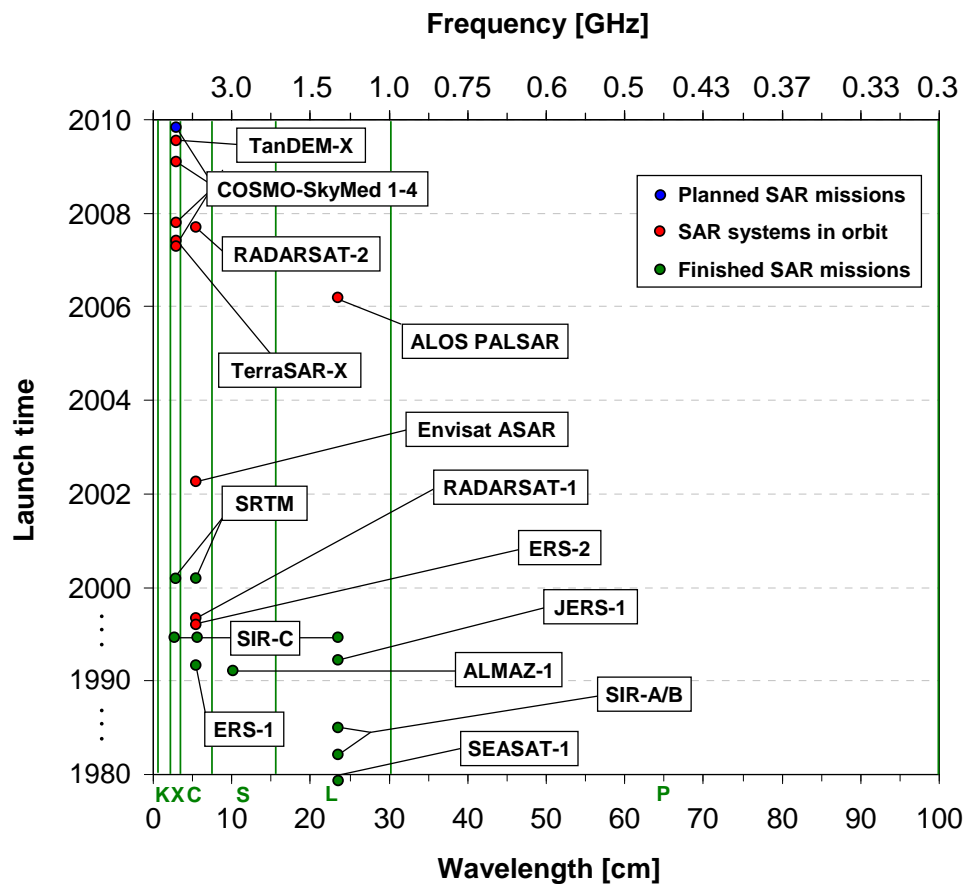


Fig. 2: Launch of civil spaceborne SAR missions since 1978 in dependence of system's wavelength (based on Lillesand et al. 2004).

In contrast to optical imagery, normal SAR data exhibit lower information content, since e.g. only one channel is available in single-polarized data. Further, the SAR data inherent speckle effect as well as the complex imaging geometry of side-looking radar systems complicate the data interpretation and automatic information extraction. The utilization of SAR data for an effective flood monitoring not only requires powerful high resolution sensors, but also optimized image analysis techniques adapted to the increased intra-class and decreased inter-class variability of the data (Bruzzone and Carlin 2006). This new data generation, in comparison to data acquired from medium-resolution SAR sensors, is characterized by higher variance in backscattering properties of different land-cover classes due to the reduced mixed pixel phenomenon. Semantic image information is hence less represented in single pixels but in homogeneous image objects and their mutual relations

(Baatz & Schäpe 1999, Benz et al. 2004). Therefore, the use of per-parcel methods describing the spatial, hierarchical and temporal contextual relationship seems promising to solve this problem.

1.2 Objectives

Against this background, the project “Flood and damage assessment using very high resolution SAR data” (SAR-HQ), which is embedded in the interdisciplinary oriented RIMAX programme (Risk Management of Extreme Flood Events; funded by the German Federal Ministry of Education and Research), aims at integrating X-band SAR data into operational processing and flood mapping workflows to ensure a fast and reliable access to detailed crisis information. In the frame of this project, the objective of this thesis is the development, application and validation of automatic methods for the detection of flooding in single-temporal as well for the extraction of flood dynamics in multi-temporal SAR data.

Following requirements have to be fulfilled by a flood detection method used in the context of rapid mapping:

- Due to the increasing number of flood situations and the rising number of SAR data-sets provided during a rapid mapping activity, the classification process should be accomplished fully automatic without any input of an active image interpreter.
- The methods should be characterized by high computational performance to enable a near real-time overview of the extent of the crisis.
- Due to the variability of flood crisis scenarios, the transferability of the methods with respect to different geographical conditions, data types and spatial resolutions is recommended.
- To ensure a simple integration into geographic information systems (GIS), the final flood and flood change masks have to exhibit high geometric accuracy. As the products will be provided to crisis management authorities to coordinate their activities in the field, the thematic accuracy should be as good as possible, even if the analysis is done under tight time constraints.
- If available, auxiliary data in form of digital elevation models (DEMs) should be integrated into the flood detection process for classification improvement.
- To enhance the information content of the classification result, methods for the generation of flood possibility (FP) maps shall be implemented, which provide supplementary information about the uncertainties related to the labeling of each image element.

1.3 Structure

In the subsequent chapter 2, the basic principles of synthetic aperture radar with a special focus on the properties of SAR data are presented. Further, a short overview about the TerraSAR-X sensor is given, whose data are predominantly used in this work.

The physical basics of the interaction of the radar signal with water surfaces under different conditions (smooth and rough open water areas, flooded vegetation, and floods in urban areas) as well as the difficulties which may arise in detecting water using SAR data are described in chapter 3.

Chapter 4 gives an overview about the state of the art concerning SAR-based water detection.

In chapter 5, the developed methodologies and the according results are presented in form of three scientific peer-reviewed papers: In chapter 5.1, a near real-time flood mapping procedure based on single-temporal TerraSAR-X data is proposed. This method combines a tile-based automatic thresholding procedure under the Gaussian distribution assumption with subsequent refinement steps using classification on a three-scaled irregular hierarchical graph and the optional integration of digital elevation information. In chapter 5.2, the automatic thresholding approach is extended to solve the three-class change detection problem in large-size feature maps represented by normalized change index (NCI) data with histogram parameterization under the generalized Gaussian assumption. An unsupervised initialized hybrid Markov model is developed on irregular hierarchical graphs for integrating scale-dependent as well as spatial contextual information into the bi-temporal change detection process in a time efficient manner. In chapter 5.3, an unsupervised flood and change detection approach is presented. This method uses a multi-contextual Markov model, which combines causal hierarchical marginal posterior mode (HMPM) estimation for inference on hierarchical graphs with noncausal spatio-temporal modeling performing a bi-directional information exchange between multi-temporal irregular planar Markov random fields (MRFs). This chapter also focuses on the issue of extracting flooded vegetation areas from X-band SAR satellite data and on the generation of flood possibility maps using marginal posterior-based entropies.

Chapter 6 gives a concluding evaluation of the proposed methods. Finally, open and unsolved problems as well as possible further investigations are pointed out.

2 Synthetic Aperture Radar

This section serves as an introduction to the essential basics of synthetic aperture radar and its imaging capabilities. Starting with the description of the basic principles of imaging radar systems, the geometric, radiometric and statistical properties of SAR data are illustrated. Finally, a short description of the TerraSAR-X sensor is given, which is the main data source for the research performed within this thesis.

2.1 Basic principles and properties of imaging radar systems

2.1.1 Basic principles of imaging radar systems

RADAR is an acronym for Radio Detection and Ranging. It is an active technique, which transmits a signal of electromagnetic energy in the form of microwave pulses at the rate of the pulse repetition frequency (PRF) and records the radar echoes of an illuminated target by an antenna (Bamler & Schättler 1993). By moving along its orbital path, a spaceborne SAR sensor focuses a single transmitted pulse perpendicular to the flight line to a restricted region on the ground, which is referred to as the antenna footprint (Fig. 3a). The entire image strip of succeeding footprints is called swath.

Since radar is basically a distance measuring method which uses the two-way travel time of the microwave pulses for a spatial separation of the received signals, the scanning process of the Earth's surface is accomplished in a side-looking fashion (Fig. 3a) perpendicular to the flight direction. This prohibits non-separability of the received signals, which would result from equal travel times of backscattered pulses from adjacent ground targets located near the nadir. In contrast to radar altimeters and scatterometers, imaging radar systems provide a two-dimensional representation of the Earth's surface after digital processing (Bamler & Schättler 1993).

Imaging radar systems are operated in so called radar bands, which cover wavelengths in the range of about 0.75 cm to 1 m. The X-, C-, and L-bands are the spectral ranges of the microwave region typically used on spaceborne radar systems (Fig. 2). Due to the fact that the atmosphere is effectively transparent for the emitted signal up to the low microwave region (10 GHz) (Elachi 1987), C- and L-band radar systems are, in contrast to passive optical sensors, characterized by an all-weather, day and night imaging capability, which makes radar systems suitable for continuous earth observation purposes. This property also applies for X-band SAR systems, except in the occurrence of hail and heavy rain cells (Danklmayer et al. 2009).

2.1.2 Resolution in range

A SAR system is characterized by its resolution in range (across-track) and azimuth (along-track) direction. The former can either be represented by the slant range or the ground range resolution. The slant range resolution r_{sl} is independent from the orbit height h and is half the transmitted pulse length τ :

$$r_{sl} = \frac{c\tau}{2} \quad (1)$$

where c is the speed of light. In contrast, the ground range resolution R_{gr} , which is the projection of R_{sl} on the ground, varies inversely with the sinus of the incidence angle θ_i and therefore enhances with increasing slant range distance (Raney 1998):

$$r_{gr} = \frac{c\tau}{2 \sin \theta_i}. \quad (2)$$

To achieve higher resolution in range, pulse duration should be as short as possible, since closely spaced objects can only be distinguished if the travel time of their backscattered signals to the antenna is different by at least $\tau/2$. However, this is difficult to realize, since the amplitude of each shortened pulse must be increased to transmit the same energy per time interval in order to maintain a sufficient signal to noise ratio (SNR). Technically this is achieved by replacing short bursts with a constant frequency by a long frequency modulated or chirped pulse (Leberl 1990). After reception, the long chirped pulse must be compressed into an equivalent short pulse using a matched filter approach.

2.1.3 Resolution in azimuth

The resolution in azimuth r_a describes the ability of an imaging radar system to separate two adjacent targets in the along-track direction of the sensor. It is defined by different factors than the resolution in range. For real aperture radar (RAR), r_a depends on the beam width φ of the antenna footprint, which can be approximated by the ratio between the wavelength λ of the transmitted pulses and the physical antenna length L :

$$\varphi = \frac{\lambda}{L}. \quad (3)$$

Since the antenna beam fans out with increasing distance R between the sensor and the target on the ground (Fig. 3b), the resolution in azimuth is defined by

$$r_{a,RAR} = R\varphi \approx \frac{R\lambda}{L}. \quad (4)$$

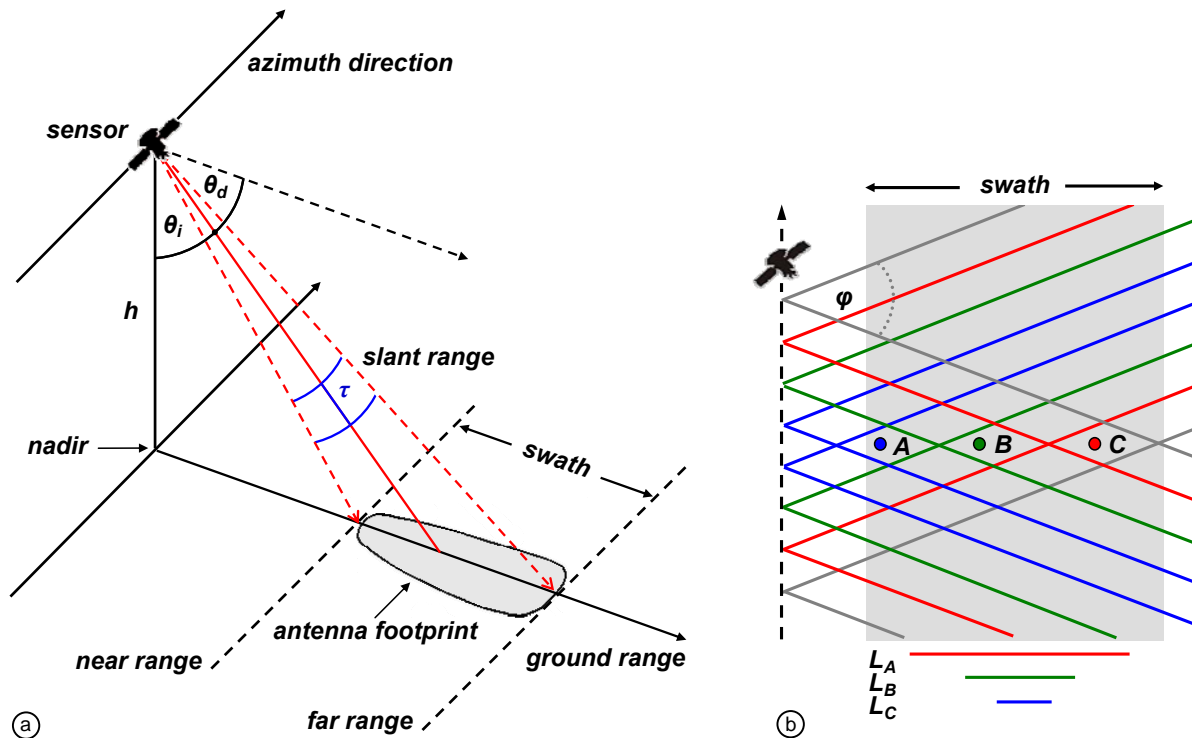


Fig. 3: a) Imaging geometry of a spaceborne SAR sensor; b) Principle of SAR systems. Targets on the ground are less frequently viewed at near range than in far range. Therefore, point A has a proportional shorter effective antenna length L_A than B (L_B) and C (L_C).

As the distance R to a target only varies slightly for spaceborne radar sensors due to the fixed orbit height, an enhanced spatial resolution can only be achieved by using an enormously large antenna. However, assuming for example a distance of 600 km between a X-band SAR sensor ($\lambda = 3.1$ cm) and a target, an antenna length of 6.2 km would be required to obtain a resolution of 3 m in azimuth direction. Obviously, this limits the usability of conventional radar for the application on satellites and is overcome by synthesizing a long physical antenna. SAR systems are thus equipped with a short physical antenna. During the motion of the sensor, the signal echoes of a scatterer are recorded coherently from subsequent antenna positions (Fig. 3b) over a long section of the sensor path (Elachi 1988) and combined in a processor using the Doppler principle, to synthesize the effect of a very long antenna. For SAR the maximal resolution in azimuth r_a is defined by

$$r_{a,SAR} = \frac{L}{2}. \quad (5)$$

Accordingly, the resolution in azimuth only depends on the antenna length L and is independent from the orbit height of the sensor platform. As targets on the ground are more frequently viewed at far range than in near range, the effective antenna length increases with slant range distance. Therefore, point A in Fig. 3b has a proportional shorter effective antenna length L_A than B (L_B) and C (L_C). In contrast to RAR systems, this results in a constant azimuth resolution irrespective of range (Lillesand et al. 2004).

2.2 SAR Signal

2.2.1 Radar equation

A radar image is a two-dimensional representation of the power P_r backscattered to a receiving antenna from an illuminated area on the ground presented as a pixel. After digital processing, this returned power is quantized and transformed into digital numbers (DNs). P_r is given by the so-called radar equation (Ulaby et al. 1982, Klausing & Holpp 2000):

$$P_r = \frac{P_t G^2 \lambda^2 \sigma n}{(4\pi)^3 R^4} \quad (6)$$

where P_t is the transmitted power and G is the antenna gain. The radar cross section σ [m^2] describes the reflection properties of a target with respect to a volume unit; i.e. the capacity to reflect the incident electromagnetic waves back to the sensor. Considering area-extensive distributed targets, σ is related to a resolution cell of size $r_a \times r_{gr}$:

$$\sigma = \sigma_0 r_a r_{gr} \quad (7)$$

where the normalized backscattering coefficient σ_0 is usually expressed logarithmically in decibel [dB]. The factor n in equation (6) considers the number of pulses, which illuminate a target during the acquisition by a SAR system. It depends on the time t during which an object is situated in the radar beam and the PRF. Using equation (5) and considering the velocity of the sensor v_{SAR} in the orbit, n can be formulated as:

$$n = t \cdot PRF = \frac{t \cdot PRF}{v_{SAR}} = \frac{R \cdot \lambda \cdot PRF}{v_{SAR} \cdot L}. \quad (8)$$

From equation (6) it can be inferred that the radar backscatter depends on system and object specific properties.

2.2.2 System specific properties

The system specific parameters encompass the wavelength [cm]/frequency [Hz] and polarization of the transmitted signal as well as the viewing geometry of the sensor.

The primary factor influencing the backscattering characteristics of the signals is the **wavelength** used in pulse transmission (Lillesand et al. 2004). Generally, radar signals of lower frequencies are characterised by a higher capacity to penetrate into media on the ground. Thus, C- and X-band SAR is preferred for the analysis of surface structures, whereas, for detecting structures below the surface, L-band SAR is favored. Additionally, the frequency of the signal determines the detectable roughness and therefore the backscattering of a surface (see chapter 2.2.3).

Electromagnetic radiation can be considered as transversal waves consisting of an electric and magnetic field vector, which both oscillate perpendicular to the propagation direction (Raney 1998). Irrespective of frequency, radar pulses can be transmitted and received in different **polarizations**; i.e. the signal is filtered in such a way that the electric field of the electromagnetic wave is restricted to a single plane perpendicular to the direction of propagation (Lillesand et al. 2004). Polarimetric SAR systems transmit either in a horizontal (H) or vertical (V) plane, which also can also be received horizontally or vertically. Thus, there can be two possibilities of like-polarization (HH, VV) and cross-polarization (HV, VH). As the dielectric and geometric characteristics of an object have a varying influence on the polarization properties of the incident electromagnetic energy, additional information about an object can be derived from the mode of signal polarization; e.g. depolarization leads to a significantly attenuated signal at like-polarization. However, a registration of the depolarized parts of the signal can be achieved by cross-polarization.

Another important factor is the **incidence angle** θ_i , which is the angle between the nadir and the incident radar beam. It sums up to 90° with the depression angle θ_d (Fig. 3a). The term local incidence angle θ_{loc} is used for the angle between the radar beam and the normal to the surface at the point of incidence. Incidence and local incidence angle are only equal for flat terrain and differ significantly from each other in hilly or mountainous regions. Since the

local incidence angle depends on the incidence angle as well as on the orientation and slope of the illuminated area, it is both a system and an object specific parameter. The incidence angle strongly determines the geometric properties of radar data and the influence of the object specific parameter roughness.

2.2.3 Object specific properties

Besides the system specific properties, the radar backscatter depends on the object specific properties. The influence of object properties on the signal return is expressed by the backscattering coefficient. For a given wavelength it is dependent on the surface roughness and the dielectric properties of the target.

Surface roughness is considered the main factor affecting radar backscattering. It determines the angular distribution of surface scattering. Smooth surface boundaries separating two semi-infinite media (Ulaby et al. 1982) act as specular reflectors and scatter the energy away from a monostatic sensor (Fig. 4a). In this case the emergent angle θ_e is equal to the incidence angle and the coherent component of the signal is very high. This results in a very low signal return, which causes relatively dark pixels in radar data. With an increase in roughness, the fraction of diffuse scattering is larger, and thus the coherent component is decreased (Ulaby et al. 1982). Such surfaces scatter incident energy in all directions and return a significant portion of the transmitted energy back to the sensor (Fig. 4b). In the extreme case where the surface is very rough (Lambertian surface), the energy is scattered equally in all directions (Fig. 4c) (Ulaby et al. 1982, Elachi 1988).

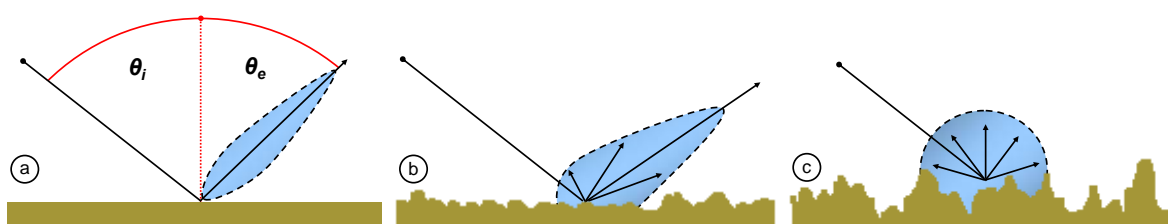


Fig. 4: Radar reflection of a) smooth, b) moderately roughened and c) strongly roughened surfaces (Lillesand et al. 2004, modified).

The roughness of a surface is not only defined by its geometric properties, but also depends on the wavelength and the local incidence angle of the signal. The relationship between these parameters is given by the Rayleigh criterion, which states that a surface is rough and acts as diffuse reflector corresponding to the expression:

$$\sigma_{rms} > \frac{\lambda}{8 \cos \theta_{loc}} \quad (9)$$

where σ_{rms} is the root mean square height of the surface variations. A more stringent condition for roughness is determined by the Fraunhofer criterion (Ulaby et al. 1982):

$$\sigma_{rms} > \frac{\lambda}{32 \cos \theta_{loc}}. \quad (10)$$

The Rayleigh and the Fraunhofer criteria state that if the phase difference $\Delta\Phi$ between two reflected waves is greater than $\pi/2$ radians and $\pi/8$ radians, respectively, the surface is considered as rough (Ulaby et al. 1982). Accordingly, more surfaces will appear smooth when the wavelength λ increases, and thus more energy will be specularly scattered (Lewis et al. 1998). Further, with increasing local incidence angle θ_{loc} , a surface must have higher elevation differences to be considered as rough.

Beside the surface roughness of objects, their shape and orientation further influence the radar signal, e.g. smooth perpendicular surfaces can act like dihedral corner reflectors generating a double bounce reflection. Since corner reflectors usually cover only small areas of the SAR data, these areas typically appear as bright spots in the image (Raney 1998).

The **dielectric properties** of an illuminated target significantly control the penetration depth and therefore the intensity of the signal. The average relative dielectric constant ϵ is the principal description of the material response to the electric field of the signal (Ulaby et al. 1986, Raney 1998). It is complex-valued and consists of a real ϵ' and an imaginary part ϵ'' , which are both highly dependent on the moisture content of the target and the signal's frequency. The real part is referred to as the permittivity of the material (Ulaby et al. 1986) and is called the dielectric constant ϵ' , while the imaginary part ϵ'' indicates losses of the dielectric constant (Ulaby et al. 1986, Raney 1998). In the microwave domain, most natural dry materials have a low value of ϵ' between 3 and 8 (Lillesand et al. 2004), whereas metals and materials with increased water content have a much higher dielectric constant, e.g. water has a value of approximately 80. Increasing moisture content leads to a stronger reflectivity and an enhanced surface scattering (Ulaby et al. 1982). In contrast, higher permittivity increases diffuse volume scattering, which appears within dielectrically discontinuous media such as vegetation. The volume scattering strength is proportional to the dielectric discontinuities inside the medium and the density of the embedded inhomogeneities. The

angular scattering distribution depends on the average dielectric constant of the medium, the roughness of the boundary surface, and the size of the distributed scatterers relative to the incident wavelength (Ulaby et al. 1982).

2.2.4 Speckle effect

SAR images are negatively affected by the occurrence of the speckle-effect, which takes the form of random variability of image tone among pixels corresponding to different resolution cells of uniform targets (Raney 1998). This effect gives SAR data a distinctive graining appearance, also referred to as a salt-and-pepper effect, which not only reduces the interpreter's ability to resolve fine details, but which also hampers the automatic processing of SAR images. This noise-like phenomenon can be understood as an interference effect, which results from the coherent imaging process. The total signal backscattered from a distributed target is the coherent sum of the signals returned from all randomly distributed discrete scatterers contained in this area. Depending on the structure of the target and location of the antenna, a signal is received that is modified by destructive and constructive interference of the scattered electromagnetic radiation. The speckle generally increases with signal intensity (Oliver & Quegan 1998). In a strict physical sense speckle cannot be considered as noise, since the identical imaging configuration results in the same speckle pattern (Bamler & Schättler 1993). The speckle-effect reduces the radiometric resolution of the images. Different methods are commonly applied to attenuate this effect at the cost of spatial resolution such as multi-look processing or filtering in the spatial, frequency, and time domain.

2.3 Geometric effects

The side-looking geometry of imaging radar systems leads to some important distortional effects, especially in mountainous regions, known as layover, foreshortening, and shadowing (Fig. 5). These effects mainly depend on the relation between terrain slope and the incident angle. Since the radar signal is transmitted radially, equal travel times to targets on the ground are placed on a circle centred at the SAR sensor. Even if features have different distances on the ground, they may have the same slant range to the antenna. **Layover** effects can be observed if the incidence angle is smaller than the slope of the object focusing the sensor. In this case, the radar pulse reaches the top of a vertical feature before the base, e.g. target *A* and *B* in Fig. 5. This results in a reversion of the terrain geometry because the top of a feature lies over its base. This effect is most severe at near range where the incidence angle is steeper. Such distortions cannot be corrected because radar echoes from several targets reach

the sensor simultaneously. Therefore, a unique spatial assignment of each signal is not possible.

When the slope facing the sensor is less steep than the incidence angle, the side of the sloped surface is compressed in the SAR image, as the time difference between the signals backscattered from the top and the base of the object is lower than their real horizontal distance (target *D* in Fig. 5). Areas affected by this **foreshortening** effect appear as bright fringes on the sensor-side of objects (Schreier 1993). The ambiguities of this range compression of the signal backscattered from foreslope areas can be corrected by means of rectification procedures which use topographic information. The **shadowing** effect occurs in radar images on slopes of objects, which are bending away from the look direction (Schreier 1993). If the slope is steeper than the incidence angle of the radar beam, no information can be derived from this terrain (target *C* and *D* in Fig. 5). Accordingly, these areas appear dark in the image. This phenomenon increases with increasing incidence angle and therefore also in range direction.

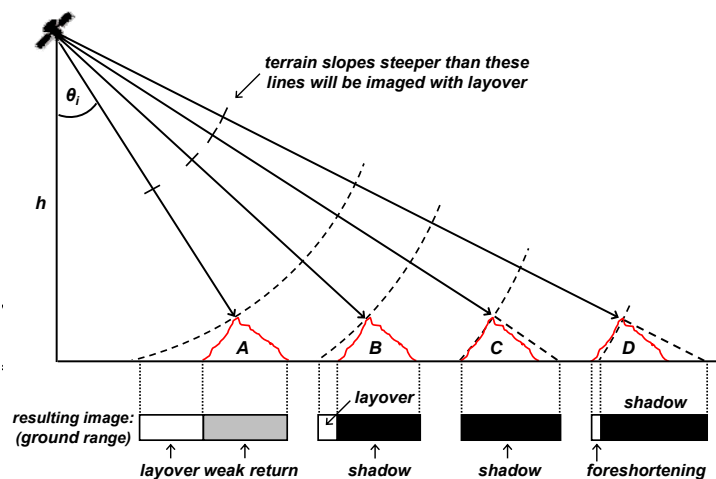


Fig. 5: Effects of terrain relief on SAR images (Lillesand et al. 2004, modified).

2.4 TerraSAR-X

In this thesis, predominantly spaceborne SAR data of the German TerraSAR-X sensor are used. The satellite was launched on June 15, 2007 into a 514 km height, sun-synchronous and near-polar dusk-dawn orbit. While the nominal repetition rate of the satellite is 11 days, each target of the Earth's surface can be observed within two to four days depending on its latitude using a large variety of different look angles (Fritz & Eineder 2009). The possibility to rotate the satellite system for an experimental left-looking mode can further accelerate acquisition times, which is particularly of importance in the context of disaster monitoring. The active X-band (3.1 cm) antenna allows the following imaging modes to be used: In the

High-Resolution Spotlight (HS) and SpotLight (SL) modes (Tab. 2), a pixel spacing between 1 to 2 m can be achieved. Depending on the mode selection (HS or SL), the size of the ground track is either 5 km x 10 km or 10 km x 10 km, respectively. In the StripMap (SM) mode (Tab. 3), TerraSAR-X acquires a strip of 30 km width with a maximum length of 1,650 km. Depending on incidence angle and processing options, the pixel spacing can be up to 3 m. The ScanSAR (SC) mode (Tab. 3) combines four adjacent StripMap beams to a total swath width of 100 km and a maximum length of about 1,650 km at a pixel spacing of 8.25 m. For each mode, a variety of acquisition and processing options can be defined (incidence angle, polarization, orbit accuracy, spatial resolution, and geocoding). On June 21, 2010, a second nearly identically constructed satellite called TanDEM-X has been successfully launched.

Tab. 2: Parameters of SpotLight (SL) and High-resolution SpotLight (HS) modes.

Parameter	HS	SL
Scene extent (azimuth x ground range)	5 km x 10 km	10 km x 10 km
Incidence angle range (full performance)	20° - 55°	20° - 55°
Azimuth resolution	1 m (single pol.) 2 m (dual pol.)	2 m (single pol.) 4 m (dual pol.)
Ground range resolution (55° - 20° incidence angle)	1.34 m - 3.21 m	1.34 m - 3.21 m
Polarization	HH or VV (single) HH/VV (dual)	HH or VV (single) HH/VV (dual)

Tab. 3: Parameters of StripMap (SM) and ScanSAR (SC) modes.

Parameter	SM	SC
Swath width (ground range)	30 km (single pol.) 15 km (dual pol.)	100 km
Incidence angle range (full performance)	20° - 45°	15° - 60°
Azimuth resolution	3 m	16 m
Ground range resolution (45° - 20° incidence angle)	1.55 m - 3.21 m	1.55 m - 3.21 m
Polarization	HH or VV (single) HH/VV, HH/HV, VV/VH (dual)	HH or VV (single)

3 Interaction between SAR signal and water bodies

In this section, the interaction between the transmitted SAR signal and a water surface under different conditions is described with regard to system and object specific parameters. In this context also the suitability of X-band SAR data for flood detection is discussed. The detectability of water in SAR data depends on the contrast between the water areas and the surrounding land, which is highly influenced by roughness characteristics of the water surface, and the system specific parameters wavelength, incidence angle and polarization. The following reflection and scatterings types can be observed: Specular reflection, corner reflection, diffuse surface scattering, diffuse volume scattering and Bragg scattering (see Fig. 6). Those effects occur when the radar signal interacts with smooth and rough open water surfaces, flooded vegetation or flooded urban areas.

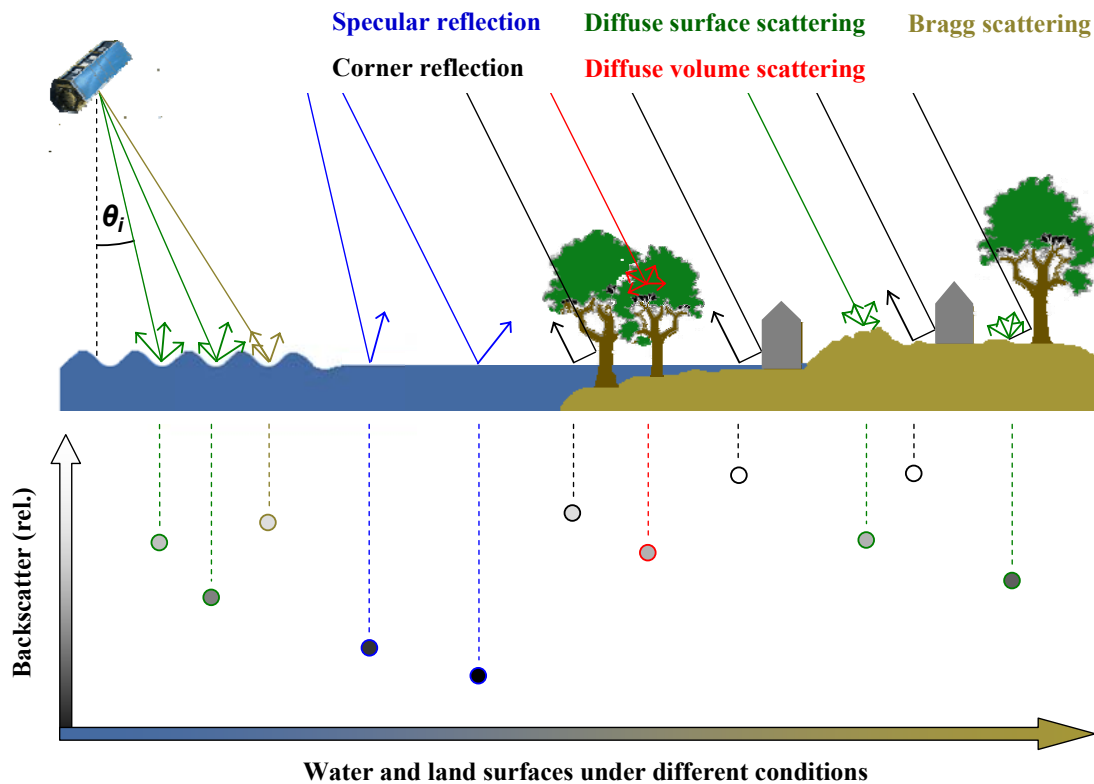


Fig. 6: Scattering mechanisms of water and land surfaces under different conditions as well as specular and diffuse components of surface scattered radiation as a function of incidence angle and surface roughness.

3.1 Smooth open water

Due to the low penetration depth of microwaves into water, surface scattering is the major scattering mechanism. The ideal case in detecting the extent of a water body is that the water surface is smoother than the surrounding land with respect to wavelength and incident

angle of the transmitted pulse. An open water body may be simplistically modeled as a perfectly smooth surface with a high dielectric constant, which acts as a specular reflector (Fig. 6) directing the incident microwave radiation away from a side-looking SAR sensor (e.g. Smith et al. 1997, Sarti 2001, Horritt et al. 2003, Mason et al. 2007). Due to a very low signal return, open smooth water surfaces appear dark in the data. These areas contrast with the brighter intensities of the rougher surrounding terrain, which is characterized by increased diffuse surface scattering. According to the Rayleigh criterion, land/water tonal contrast rises with increasing incidence angle (e.g. Drake & Patton 1980, Foster & Hall 1981, Moughinis-Mark 1984, Malnes et al. 2002, Solbø et al. 2004). Even if a decreasing system wavelength increases the backscatter of a smooth water surface due to its enhanced sensitivity to diffuse scattering, a higher contrast ratio between water and the land areas occurs, as the number of possible features on the land that might appear smooth and similar in tone to water is less than with longer wavelength (Drake & Shuchman 1974). Consequently, X-band appears to be more suitable for water detection purposes than C- and L-band.

However, imaging at smooth incidence angles also means an increase in the occurrence of radar shadowing (Fig. 5) (Lewis 1998). Radar shadows are exacerbated in mountainous terrain and in high resolution imagery also behind single vertical objects such as trees or buildings. These areas of low signal return are easily mixed up with smooth open water areas and lead to errors of commission. These errors also occur at look-alike areas of reduced surface roughness such as bare ground, sand dunes, airport runways, streets as well as in X-band imagery at cloud-shadows, which are generated by an attenuation of traversing signals due to hydrometeors in clouds (Danklmayer et al. 2010). In contrast, imaging with steep incidence angles increases the probability of radar layover. This source of information loss is particularly obstructive in identifying narrow water bodies bounded by high trees or banks (Henderson 1987).

Also the choice of polarization plays a role in detecting open water areas. Generally, HH polarization provides the most obvious discrimination between water and other types of land cover classes as it offers the best radiometric dynamic range (e.g. Sarti 2001, Malnes et al. 2002, Ahtonen et al. 2004, Henry et al. 2006, Schumann et al. 2007). This is caused by a low scattering of the horizontal component of the signal from the open water surface. Even if HH and VV polarizations leads to nearly identical separability of class distributions over a smooth water surface in TerraSAR-X data (Fig. 7a), an increase in surface roughness reduces the ability to discriminate between water and land in VV more than in HH polarization (Fig. 7b). Over smooth water surfaces, like-polarization offers improved class separability in

comparison to cross-polarization (Fig. 7c, Fig. 7d). Several studies showed the superiority of cross-polarization HV (Horritt et al. 2003, Henry et al. 2006) and VH (Solbø & Solheim 2004, Schumann et al. 2007) over like-polarization VV in terms of a roughened water surface, given the fact that a VV polarized signal is more sensitive to ripples and waves. Flood mapping accuracy may benefit from combining backscatter variations in different polarizations (Henry et al. 2006, Ngiem et al. 2000). However, the use of a multi-polarization mode results in a reduced resolution and coverage, which needs to be traded off against the increased information content.

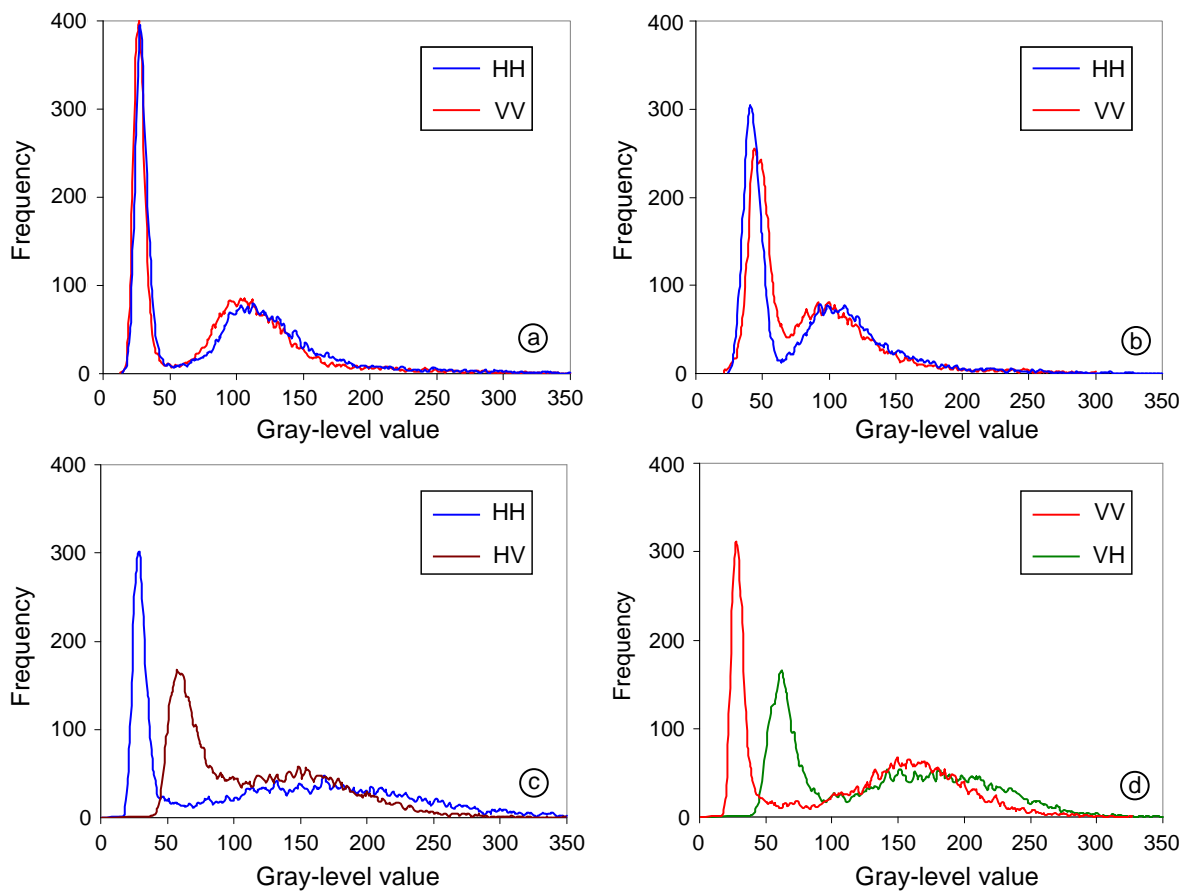


Fig. 7: Separability of classes water (left populations) and land (right populations) in histograms of TerraSAR-X StripMap data in dependence of polarization: HH vs. VV polarization on a) smooth and b) slightly roughened water surface, c) HH vs. HV and d) VV vs. VH polarization on a smooth water surface.

3.2 Rough open water

The influence of wind and rain as well as turbulence effects leads to the emergence of small perturbations (ripples) (Lewis 1998) in the scale of millimetres to centimetres and longer waves with wavelength in the order of metres and kilometres on the water surface. An increasing degree of roughness causes a higher backscattering signal and therefore an

enhanced brightness in the SAR data, which effects backscatter intensities equal or higher than the surrounding land areas (Fig. 6).

A special case of scattering occurs for lightly rough water surfaces with tiny capillary waves and short gravity waves at incidence angles beyond 30° (Ulaby et al. 1982). If the scatterer positions are oriented in such a way that they have geometric structures aligned with the phase fronts of the illumination and if they are spaced periodically in range, then the backscattering strongly increases through constructive inference at certain incidence angles. The Bragg equation describes the relationship between the wavelength of the periodically spaced surface patterns λ_R , the wavelength λ and the incidence angle θ_i of the SAR signal (Fig. 8):

$$\lambda_R = \frac{k\lambda}{2\sin\theta_i} \quad (11)$$

where k is the order of the resonance. In microwave applications, normally the lowest order number $k = 1$ applies (Raney 1998). According to the Bragg model (Fig. 8), a random surface is subdivided into its Fourier spectral components. Bragg scattering occurs from the component corresponding to the Bragg resonance condition; i.e. if the slant range distance between two successive wave crests oriented perpendicularly to the range direction is $\lambda/2$.

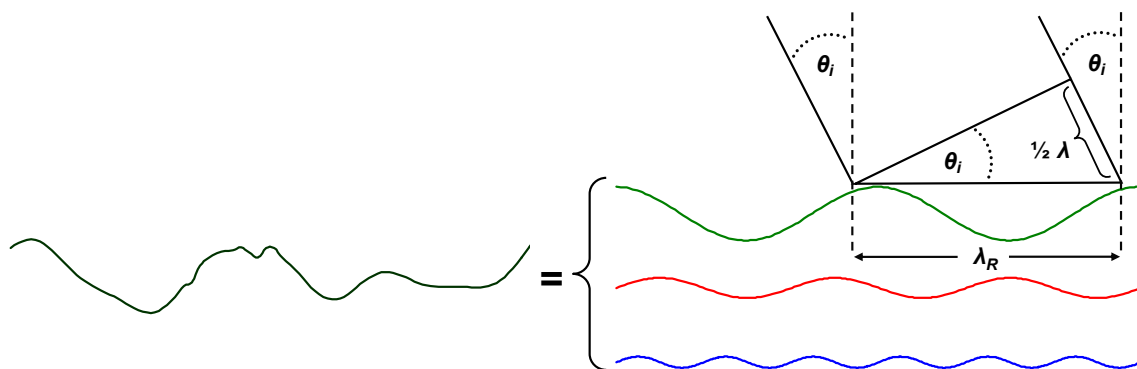


Fig. 8: Fourier spectral components of a rough water surface and resonant Bragg scattering (Elachi 1988, modified).

The larger a water body, the more susceptible it becomes for the formation of waves. Narrow rivers seldom show wind pattern, whereas on ocean surfaces roughness structures occur more often. In general the visible roughness structure of roughened water bodies does not show regular wave patterns. Regular patterns can mainly be observed on ocean surfaces,

whereas irregular patterns occur more frequently on the surface of large inland water bodies such as lakes.

3.3 Flooded vegetation

The backscatter increase over a water surface may not only be induced by waves but also by interspersed vegetation. SAR, with its unique ability to penetrate canopy even during leaf-on periods, offers the unique opportunity to map inundations beneath vegetation. This is enabled by multiple-bounce effects: The penetrated radar pulse is backscattered from the horizontal water surface and lower sections of the vegetation (trunks and branches) resulting in strong signal return (e.g. Richards et al. 1987, Townsend 2001, Hong et al. 2010), which is higher than in non-flooded conditions (Fig. 6). Diffuse scattering from the ground during dry conditions reduces this corner reflection effect, yielding darker image tones (Hess et al. 1990).

However the signal return from flooded vegetation is very complex and strongly depends on the system's wavelength, the canopy type, structure and closure as well as on other factors such as incidence angle and polarization. The interaction of these parameters can be described by theoretical scattering models (e.g. Ormsby et al. 1985, Richards et al. 1987, Wang et al. 1995, Kasischke & Bourgeau-Chavez 1997). According to Kasischke & Bourgeau-Chavez (1997) and Townsend (2002), the backscatter coefficient ($\sigma_{0,h}$) of wetlands dominated by herbaceous vegetation can be described by

$$\sigma_{0,h} = \sigma_{0,c} + \tau_c^2 (\sigma_{0,s} + \sigma_{0,m}) \quad (12)$$

where $\sigma_{0,c}$ is the backscatter coefficient of the vegetation canopy, τ_c is the transmission coefficient of the vegetation canopy, $\sigma_{0,s}$ is the backscatter from the ground surface, and $\sigma_{0,m}$ stands for the backscatter from multi-path scattering between the ground surface and the canopy. For the computation of the backscattering coefficient of wetlands containing woody vegetation ($\sigma_{0,w}$) such as shrubs and trees, the direct backscatter from the tree trunks $\sigma_{0,t}$, the attenuation of the radar signal by the tree trunks τ_t and the double-bounce scattering $\sigma_{0,d}$ between the trunks and the water surface have additionally to be considered (Fig. 9):

$$\sigma_{0,w} = \sigma_{0,c} + \tau_c^2 \tau_t^2 (\sigma_{0,s} + \sigma_{0,t} + \sigma_{0,d} + \sigma_{0,m}). \quad (13)$$

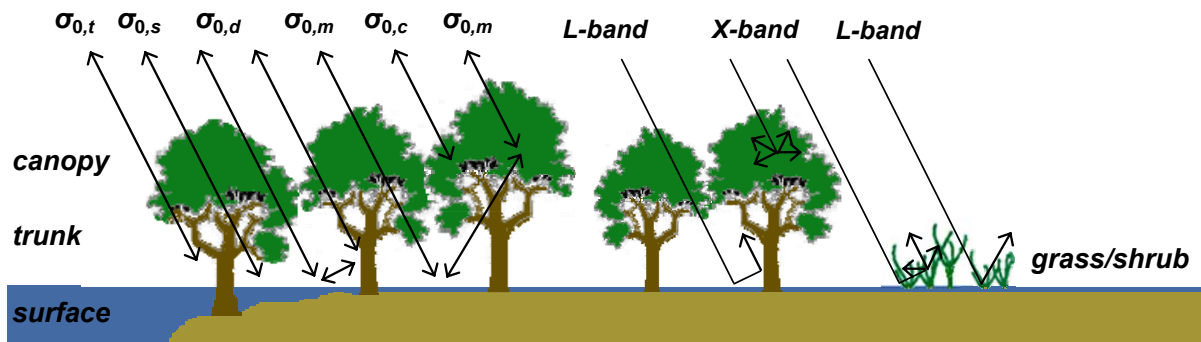


Fig. 9: Conceptual illustration of the major sources of backscatter from vegetation (Kasischke et al. 1997 and Lang et al. 2008, modified) and effect of flooded vegetation on X- and L-band SAR (Ormsby et al. 1985, modified).

Generally, the longer the system's wavelength, the higher is the capability of the signal to penetrate the vegetation canopy (Fig. 9). This is particularly the case when wavelength is substantially longer than the leaf size (Pope et al. 1994, Wang et al. 1995). Therefore, L-band SAR sensors have proven to be effective to map flooding in forest environments (e.g. Ormsby et al. 1985, Richards et al. 1987, Hess et al. 1990, Hess & Melack 1994, Hess et al. 1995, Townsend & Walsh 1998, Melack & Wang 1998, Saatchi et al. 2000, Hess et al. 2003), as in these wavelengths, the double-bounced trunk-ground signal interactions generate a bright signature in SAR data (Richards et al. 1987). In contrast, in C-band, and especially X-band, canopy attenuation, volume and surface scattering from the top layer of the forest canopy will be higher (Richards et al. 1987). In these wavelengths, the effect of enhanced backscattering is reduced, which causes a strongly decreased ratio between forests in dry and flooded conditions.

However, some studies conclude that C-band data can still be a valuable tool to map flooding beneath some types of floodplain forest canopies (Townsend & Walsh 1998, Rao et al. 1999, Townsend 2001 and 2002, Costa 2004, Lang et al. 2008). Experiments show that RADARSAT-1 C-HH data can be used to map flooded forests in temperate regions regardless of season and water stage. An increase in canopy foliage leaf-area index (LAI) reduces the transmissivity of the crown layer (Townsend 2001 and 2002), and thus diminishes the amount of microwave energy reaching the forest floor (Lang et al. 2008). Therefore, higher classification accuracies can generally be derived during leaf-off conditions (Townsend 2001 and 2002). Further, a backscatter increase over floating aquatic macrophytes and emergent shrubs in floodplain lakes is reported by Alsdorf et al. (2000) in C-band data.

High X-band double-bounce returns from flooded forests only occur at the edges where the penetration of the vegetation canopy is not an issue (Henderson 1995, Solomon 1993).

At shorter or sparser vegetation with thin branches and small diameter trunks brighter backscattering effects may occur with decreasing wavelength. For example Horritt et al. (2003) observe enhanced backscatter over a marshland environment in C-band rather than in L-band. The reason for this effect lies in the ability of the C-band signal to penetrate the sparse canopy and to interact with the water surface and the lower parts of the vegetation. This causes an enhanced signal return. In contrast, the canopy may be too transparent to interact with the vegetation at L-band (Fig. 9 and Fig. 10). Also results given in Ormsby et al. (1985) and Ramsey (1995) indicate enhanced backscattering in marshland areas in C-Band and even in X-Band, respectively. From interferometric coherence investigations over South Florida's Everglades with TerraSAR-X data, Hong et al. (2010) suggest that multiple bouncing between the water surface and lower parts of the vegetation is the dominant scattering effect in wetlands. Therefore, also in X-band there is a certain potential to derive flooding beneath vegetation.

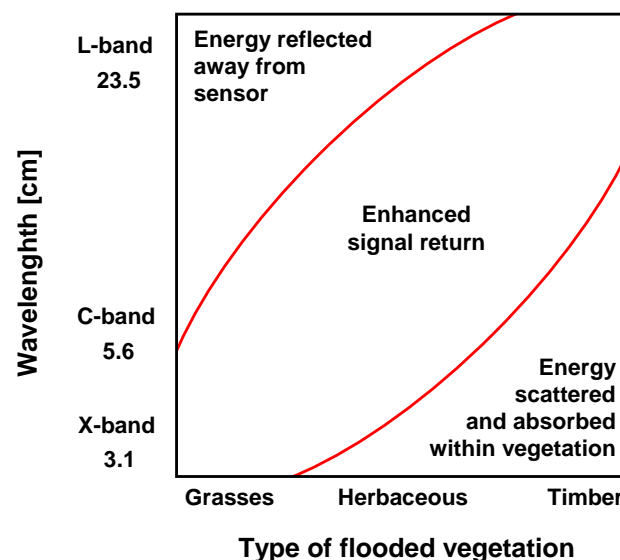


Fig. 10: Relative radar return responses for different wavelengths and flooded vegetation types (Ormsby et al. 1985, modified).

The incidence angle has a major impact on the detectability of inundation beneath vegetation. Several studies indicate that steeper incidence angles are preferable for distinguishing flooded from non-flooded forests (e.g. Richards et al. 1987, Hess et al. 1990, Wang & Imhoff 1993, Wang et al. 1995, Bourgeau-Chavez et al. 2001, Lang et al 2008). This generalization can be attributed to a shorter path length through the canopy, increasing transmissivity in the crown layer and leaving more microwave energy for the ground-trunk interactions. In contrast, shallower incidence angle signals interact more with the intervening canopy, resulting in increased volume scattering (Hess et al. 1990, Lang et al. 2008).

This angular dependence is not completely confirmed in literature and strongly depends on forest type and structure (Hess et al. 1990, Lang et al. 2008). Some earlier works (Ormsby et al. 1985, Imhoff et al. 1986) state that variations in the incidence angle do not affect the detection of the flood areas. Using C-HH RADARSAT-1 data from forested wetlands in north-eastern North Carolina, Lang et al. (2008) report that the potential to map flooding beneath forest canopies was less than expected at steeper and greater than expected at shallower incidence angles. The capability to detect flooding under leaf-on conditions varies much more according to incidence angle while forest type has a greater effect during the leaf-off season. Although a subtle decline in total backscatter return with shallower incidence angle is stated for all flooded forest types in this study, the smallest incidence angle of 23.5° considered in this study exhibits the smallest average difference in backscatter coefficient between flooded and non-flooded areas during both leaf-on and leaf-off periods. According to Lang et al. 2008, this presumably depends on the orientation of canopy leaves during the leaf-on season and on soil moisture conditions in the absence of flooding. The best discrimination between flooded and non-flooded forests is feasible using data collected at moderate incidence angles of 27.5° and 33.5° (Lang et al. 2008).

Radar systems with multiple polarizations provide much more information on inundated vegetation areas than single-polarization radars (Hess & Melack 2003, Horritt et al. 2003). Various studies employing multi-polarized data indicate a preference towards like-polarization (HH or VV) for separating flooded and non-flooded forests (e.g. Wu 1984, Evans et al. 1986, Wu & Sader 1987). Backscattering is generally very weak for cross-polarization (HV or VH) as depolarization does not occur for ideal corner reflectors (Leckie 1998). According to Wang et al. (1995) and Townsend (2002), the ratio of backscatter from flooded forest to that from non-flooded forest is higher at HH polarization than at VV polarization.

Comprehensive reviews of the interaction of various radar systems with a wide range of vegetation types are provided by e.g. Hess et al. (1990), Melack et al. (1994), Townsend (2002), Hess et al. (2003), Lang et al. (2008).

3.4 Floods in urban areas

The detection of flooding in urban areas with SAR is complicated by a number of factors. Fig. 11 schematically shows two buildings separated by a flooded street. Dihedral and trihedral reflection from buildings as well as the presence of metal surfaces leads to enhanced backscatter and strong contributions from side-lobes, which are nearly equal for non-flooded

and flooded situations. The double bounce effect between roads and walls is visualized by C_1C_2 and C_3C_4 for flooded and non-flooded conditions, respectively. Also SAR specific illumination phenomena adversely affect the appearance and ability to detect flooding. Due to the side-looking nature of SAR, areas might not be visible due to shadowing (SB) and layover (AL) caused by buildings. The only possibility to observe flooding is between L and S , as in this gap the incident signal is characterized by a single specular reflection (e.g., at R). Therefore, the larger the distance between L and S and the higher the resolution of the SAR sensor, the greater the likelihood to monitor inundations in urban areas. However, non-flooded roads and other smooth man-made surfaces generally also appear dark due to specular reflection. Therefore, they can hardly be separated by calm flooded urban areas (Giacomelli et al. 1995, Oberstadler et al. 1997, Solbø & Solheim 2004, Mason et al. 2010).

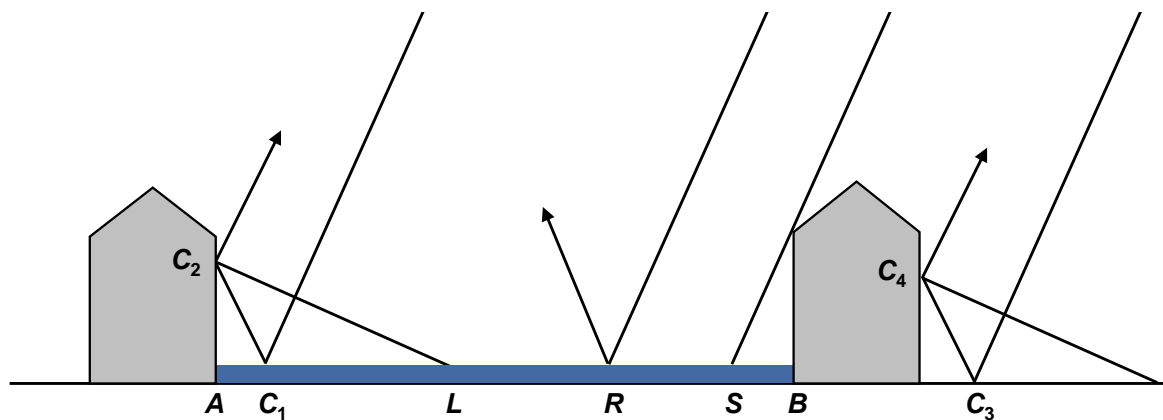


Fig. 11: Layover (AL) and shadow (SB) areas in a flooded street (AB) between adjacent buildings as well specular reflection from water surfaces (R) and double bounce effects between roads and buildings in flooded (C_1C_2) and non-flooded (C_3C_4) conditions (Mason et al. 2010, modified).

4 State of the art in SAR-based water detection

SAR remote sensing techniques have become promising tools for determining the extent and duration of flooding in different geographical areas. This section provides an overview of the state of the art regarding water detection techniques. The goal is not to present a comprehensive review of the large amount of published work, but to give an idea of principal research approaches and applications. A number of methods for the delineation of flood and water extent in SAR imagery of both fluvial and tidal environments have been developed. Using single-temporal data, these algorithms are only able to extract water bodies. The integration of additional information from pre-flood normal water level conditions enables the identification of inundation areas. Analysis of SAR satellite data for flood inundation mapping is generally carried out either by visual interpretation or by digital image processing techniques.

Visual interpretation gives a reasonably accurate assessment of the water extent (Sanyal & Lu 2003), but as this is carried out manually by digitalization of the land/water boundary, it is very time-consuming, especially when the area to be mapped is large (Matgen et al. 2007). Additionally, the quality of results strongly depends on background knowledge and therefore on the subjective impression of the image interpreter, which makes it difficult to reproduce the results.

In digital image analysis, the applied technique classifies each image element into water and non-water categories using their individual backscattering value and potentially also contextual and auxiliary information.

Thresholding is an important step in many pattern recognition systems (Li & Lee 1993) to binarize images by separating the object and the background class according to a suitably selected threshold value. This method is one of the most popular image processing techniques to distinguish between water and non-water areas in SAR imagery. Commonly, all image elements of the SAR amplitude or intensity data with a gray value lower than a given threshold are assigned to the water class. Due to its simplicity, this method is computationally very fast and therefore suitable for rapid mapping purposes. In moderate roughness conditions of the water surface, usually most of the water body extent can be derived by this technique, as the contrast between the water and non-water class is significant. In case double-bouncing inundated vegetation areas are prevalent, a threshold position has to be found above which all image elements are assigned to an additional class “flooded vegetation”. This is of particular importance for flood mapping in tropical and subtropical climatic zones, since in these

regions large forest areas, mangroves or marshlands are regularly affected by inundation beneath vegetation canopies. An adequate threshold position can be determined in a supervised manner using visual inspection of the image histogram or manual trial-and-error procedures (e.g. Townsend & Walsh 1998, Chen et al. 1999, Townsend 2001, Brivio et al. 2002, Henry et al. 2006, Matgen et al. 2007, Lang et al. 2008). In this case, the quality of the results highly depends on the visual interpretation and hence subjective impression of the operator. Therefore, such interactive threshold determination lacks objectivity and traceability. Automatic thresholding procedures can overcome these problems. In this context, e.g. Sahoo et al. (1988), Pal & Pal (1993), and Bazi et al. (2007) provide extensive methodological reviews. Surprisingly, only few studies use automatic thresholding for flood detection (e.g. Ahtonen et al. 2004, Solbø & Solheim 2004, Schumann et al. 2007). In chapter 5.1 and 5.2, more detailed information about automatic thresholding techniques is given.

In most cases, multi-temporal image analysis has proven superior to mono-temporal approaches. Change detection can be used as an effective tool to delineate inundation in multi-temporal SAR imagery. Numerous techniques have been developed for detecting changes in registered remote sensing data. Extensive methodological overviews can be found in Singh (1989), Mas (1999), and Lu et al. (2004). During flood mapping, change detection is usually performed by comparing pre- or post-disaster reference data with in-flood imagery using Post-Classification comparison (e.g. Herrera-Cruz & Koudogbo 2009) as well as by analyzing feature maps such as difference (e.g. Peng et al. 2004, McMillan et al. 2006), normalized difference (Nico et al. 2000), ratio (e.g. Rémi & Hervé 2007), and log ratio data (e.g. Bazi et al. 2005). Amplitude as well as coherence change detection are applied in the SAR domain. In the amplitude approach, areas are determined as flooded where the backscatter considerably decreases in case of calm open water areas or increases in case of double-bouncing vegetation areas from pre-/post-disaster imagery to in-flood data. Phase information derived from SAR interferometry also has the potential to be used for flood mapping. Several studies (e.g. Wegmüller et al. 1995, Marinelli et al. 1997, Dellepiane et al. 2000) state that water can be identified as regions of low interferometric phase correlation between two SAR scenes, which can be separated from land areas of higher coherence. To increase the efficacy of identifying flooded areas, Nico et al. (2000) and Buck & Monni (2000) perform combined amplitude and interferometric processing on multi-band ERS-1/2 images. Most studies in the coherence domain are accomplished with data pairs of the former ERS tandem mission (1995-1996), which offer high coherence over most non-flooded areas due to the short time interval of up to one day between data acquisitions of the ERS-1 and

ERS-2 satellites. At present, repeat-pass SAR interferometry, especially in X-band, is not very suitable for flood mapping due to the strong temporal signal de-correlation over non-water areas during the repetition period (e.g. 11-day repeat interval for TerraSAR-X), in which precise phase matching between the two SAR signals is degraded. In the near future this method will become more interesting due to the upcoming single-pass interferometric acquisitions of DLR's TanDEM-X mission, which will provide short temporal baselines of few milliseconds to seconds.

Several supervised approaches exist, which identify the floodplain using statistical properties of manually selected training data. For example De Roo et al. (1999) perform Maximum Likelihood (ML) classification on ERS-1/2 data assuming approximately normal distributions of the classes "flooded" and "non-flooded". Townsend (2001 and 2002) uses a binary decision classifier (Clark & Pregibon 1993) on RADARSAT-1 and ERS-1 imagery for differentiating between flooded and non-flooded forests. The same classifier is used by Wang (2004) for the classification of water, marsh, field, and flooded and non-flooded forest using two sets of JERS-1 data.

Most of the above mentioned studies consider pixels as smallest geometrical components of raster data. The classification of each image element is accomplished independently on the basis of its observed intensity vector without incorporating any contextual information. The accuracy of such methods is strongly affected by a salt-and-pepper appearance leading to a potential misclassification of such pixels. Context is a rich information source for the analysis of remote sensing imagery. Especially in data from the new generation of high resolution SAR sensors, objects on the ground are usually larger than the pixel size. Thus, there is a strong likelihood that adjacent pixels, although characterized by different spectral properties, belong to the same land-use/land-cover unit (LULC), unless these elements are located in boundary areas. If such contextual information can be well modeled, the classification accuracy may be improved significantly (Tso & Olsen, 2005). Different approaches consider spatial-contextual information from a local neighborhood within the flood-detection workflow: In Ahtonen et al. (2004), an automatic surface water detector is proposed, which integrates information in form of local texture features into the labeling scheme. This method uses a ML classifier trained by unsupervised thresholding of log-mean data. Classification is performed on a three dimensional feature space composed of logarithmically transformed occurrence measures (Anys et al. 1994) mean, variance, and difference between minimal and maximal intensity within 5 x 5 pixel-sized sliding windows around a center pixel.

Kussul et al. (2008) present a supervised flood mapping procedure for medium-resolution SAR using Kohonen's self-organizing maps (SOMs) (Kohonen 1995, Haykin 1999) based artificial neural networks (ANN). For considering spatial connections between neighboring pixels, the network is trained in an unsupervised manner using backscatter values from sliding windows.

Some studies integrate digital topographic information to improve the classification result by detecting flooding beneath vegetation or by removing look-alike areas according to simple hydrological assumptions (e.g. Wang et al. 2002, Horritt et al. 2003, Mason et al. 2007, Mason et al. 2010). Within this scope, Pierdicca et al. (2008) present a flood mapping procedure based on fuzzy sets considering local context in form of intensity, topographical, and land cover information.

In the past, several methodologies based on region growing have been used in waterline detection. Commonly, seeded regions expand according to their statistical properties until stopping conditions are reached. Within this context, Malnes et al. (2002) propose a simple method using RADARSAT-1 data. Supervised initialized water areas are grown by clustering adjacent pixels that are within three standard deviations from the mean intensity value of the respective region. Mason et al. (2010) present a supervised seeded region growing method for urban areas, which involves clustering using iterated region dilatation and labeling, followed by erosion. Areas in which water would not be detectable due to layover and shadowing effects are identified by DLR's SAR end-to-end simulator (SETES) from digital surface models (DSMs) of LiDAR (Light Detection and Ranging) data and are excluded from processing.

In recent years, more sophisticated region growing procedures of statistical active contour models (ACMs), so called snake algorithms, gained in popularity for delineating land/water boundaries in single-polarized SAR data. These algorithms make use of dynamic curvilinear contour to iteratively search through the 2-D image space until it settle upon object boundaries, driven by an energy function that is attracted to edge points. ACMs have proven useful for converting unconnected or noisy image edges into smooth continuous vector boundaries. Therefore, these algorithms are suitable for segmenting speckle-affected SAR data. The first snake model was introduced by Kass et al. (1987), and developed further in e.g. Williams & Shah (1992) and Ivins & Porrill (1994). Mason & Davenport (1996) use a modified version of the ACM presented by Williams & Shah (1992) to connect shoreline edges in ERS-1 data, derived by a contrast ratio edge detector (Touzi et al. 1998). A similar approach is developed in Niedermeier et al. (2005): First, a wavelet edge detection method is

applied, followed by thresholding and blocktracing, to distinguish between edge-free sea surfaces and land areas of higher edge density. Finally, a snake algorithm is applied to a restricted region on either side of the land/water boundary to link unconnected edge fragments into a continuous waterline. Based on the study of Irvin & Porrill (1994), a semi-automatic ACM (Psnake NT) is developed by Horritt (1999), who identifies flooding as regions of homogeneous speckle statistics. The energy function used is formulated to account for the gamma-distribution intensity of SAR images. This algorithm was widely used in the last decade for river flood delineation in rural areas using medium-resolution SAR data (e.g. De Roo et al. 1999, Horritt et al. 2001, Ahtonen et al. 2004, Matgen et al. 2007, Schumann et al. 2009) and was further successfully applied for computing polygonal approximations of rough sea water surfaces (Horritt 2001). Mason et al. (2007) modify Psnake NT in the way that the snake is not only conditioned on SAR data, but also by using LiDAR digital elevation models (DEMs). Using 3-D rather than 2-D curvature, the resulting waterline becomes smoothly varying in ground height. One disadvantage of Psnake NT is that this algorithm is related to significant user input. Several initializations of the contour line by manually set seed vectors are necessary to obtain satisfying results. Further, as Psnake NT belongs to the group of parametric ACMs, which have a rigid topography, additional snake seeds are necessary to delineate isolated flood regions (Mason et al. 2010). This, however, is critical in high resolution SAR data, where, in contrast to medium- and coarse-resolution data, the inundation area is commonly separated in multiple isolated flood regions by e.g. vegetation areas or man-made objects, which prohibit the expansion of the snake. In this case, geometric snake models (e.g. Malladi et al. 1995), which permit topology changes due to flexible level sets to simultaneously detect several water objects seem to be more suitable. Within this context, a semi-automatic flood detection algorithm based on region-based level sets is proposed by Silveira & Heleno (2009).

A Bayesian segmentation technique to separate land and sea regions in TerraSAR-X data is used by Ferreira and Bioucas-Dias (2008). The class conditional densities are estimated by a finite mixture of Gamma distributions whose parameters are approximated from manually selected land and sea training samples. The *a priori* probability of the labels is modeled by a Markov random field (MRF), which promotes local continuity of the classification result given a spatial neighborhood system. The maximum *a posteriori* estimation is performed by using graph cuts (Kolmogorov & Zabih 2004).

Object-based image analysis has constantly gained importance in earth observation applications during the last few years (Baatz & Schäpe 1999, Blaschke & Strobl 2001, Meinel

et al. 2001, Benz et al. 2004). It is based on the concept that important information necessary for image analysis is not always represented in single pixels but in homogeneous image segments and their mutual relations (Benz et al. 2004). Based on similarity criteria of gray values or textural properties, this procedure first extracts disjoint uniform image objects without any semantic meaning, which are classified subsequently. This offers the advantage that in addition to spectral-related characteristics of the segments parameters such as contextual information, texture and object geometry can be used for improving classification accuracy. The image partitioning can be accomplished by one of the standard techniques proposed in the literature (Haralick & Sharipo 1985, Zhang 1996, Carleer et al. 2005). A comparison of recent object-oriented image analysis algorithms applied in remote sensing is given in Meinel & Neubert (2004), Neubert et al. (2006), and Neubert & Herold (2008). One of the most effective image segmentation techniques is the Fractal Net Evolution approach (FNEA) (Batz & Schäpe 1999), which enables a multi-scale representation of the data using a bottom-up region merging method. Just a limited number of studies present object-based classifications for flood mapping purposes (e.g. Heremans et al. 2003, Hess et al. 2003, Herrera-Cruz & Koudogbo 2009). Further, these methods make only limited use of contextual information by classification of image elements generated by a segmentation step. Inter-spatial relationships between adjacent objects are not fully exploited and intra-spatial dependancies between multi-scale representations of the SAR data are ignored.

In summary, it can be stated that most of the water detection methods proposed in the literature require a considerable amount of user intervention. Further, they are not adapted to the new generation of SAR data, which are characterized by increased intra-class and decreased inter-class variability of the data in comparison to data acquired from medium-resolution SAR sensors. Finally, previous studies only integrate contextual information to a minor degree into the classification scheme without exploiting the hierarchical nature of remote sensing data.

Within the next section, automatic flood detection methods are presented, which incorporate multi-contextual information into operational flood detection workflows. In this scope, MRFs (Geman & Geman 1984, Li 2009) represent an effective and theoretically well established probabilistic model for integrating different types of contextual information such as spatial (e.g. Besag 1986), hierarchical (e.g. Laferté et al. 2000) and temporal context (e.g. Melgani & Serpico 2003) into the labeling process. Generally, MRFs are used in a probabilistic generative framework modeling the joint probability of data and its corresponding labels using Bayes rule. These models have proven to be effective tools for

image segmentation and image restoration purposes (e.g. Geman & Geman 1984, Besag 1986, Dubes & Jain 1989). In chapter 5.2 and 5.3, the basics and state of the art concerning causal and noncausal MRFs are given to provide the fundamentals required for the development of a hybrid Markov approach, which models the hierarchical, spatial, and optional temporal relationships between segmented image object of automatically generated irregular hierarchical graphs.

5 Publications

5.1 Paper 1

Martinis, S., Twele, A. & Voigt, S., 2009: Towards operational near real-time flood detection using a split-based automatic thresholding procedure on high resolution TerraSAR-X data. – Natural Hazards and Earth System Sciences, 9: 303–314, DOI 10.5194/nhess-9-303-2009.

Towards operational near real-time flood detection using a split-based automatic thresholding procedure on high resolution TerraSAR-X data

S. Martinis, A. Twele, and S. Voigt

German Aerospace Center (DLR), Oberpfaffenhofen, Germany

Received: 4 December 2008 – Revised: 19 February 2009 – Accepted: 26 February 2009 – Published: 11 March 2009

Abstract. In this paper, an automatic near-real time (NRT) flood detection approach is presented, which combines histogram thresholding and segmentation based classification, specifically oriented to the analysis of single-polarized very high resolution Synthetic Aperture Radar (SAR) satellite data. The challenge of SAR-based flood detection is addressed in a completely unsupervised way, which assumes no training data and therefore no prior information about the class statistics to be available concerning the area of investigation. This is usually the case in NRT-disaster management, where the collection of ground truth information is not feasible due to time-constraints. A simple thresholding algorithm can be used in the most of the cases to distinguish between “flood” and “non-flood” pixels in a high resolution SAR image to detect the largest part of an inundation area. Due to the fact that local gray-level changes may not be distinguished by global thresholding techniques in large satellite scenes the thresholding algorithm is integrated into a split-based approach for the derivation of a global threshold by the analysis and combination of the split inherent information. The derived global threshold is then integrated into a multi-scale segmentation step combining the advantages of small-, medium- and large-scale per parcel segmentation. Experimental investigations performed on a TerraSAR-X Stripmap scene from southwest England during large scale flooding in the summer 2007 show high classification accuracies of the proposed split-based approach in combination with image segmentation and optional integration of digital elevation models.

1 Introduction

The demand for near real-time (NRT) information on natural disasters has increased considerably during recent years worldwide. Flooding is considered as the world’s most costly type of natural disaster in terms of both property damage and human casualties. Because of their nearly all-weather day-night capabilities, ensuring data-gathering on every overpass, satellite Synthetic Aperture Radar (SAR) sensors are optimally suited for providing reliable information on extensive floods, which usually occur during long lasting precipitation and cloud cover periods. Flood information is needed as quickly and detailed as possible to provide an overview of the situation to improve crisis management and response activities. For that purpose an unsupervised flood detection approach particularly oriented to the analysis of single-polarized very high resolution SAR satellite data is presented.

Among supervised classification (e.g. Townsend et al., 2002), various change detection methods (e.g. Bazi et al., 2005; Brivio et al., 2002; Nico et al., 2000) and the application of active contour models (e.g. Mason et al., 2007), thresholding is one of the most popular image processing techniques to separate flooded from non-flooded areas in SAR imagery (e.g. Chen et al., 1999; Brivio et al., 2002; Matgen et al., 2007). Commonly, this classification is performed by assigning all elements of a SAR intensity image with a scattering cross-section lower than a given threshold to the class “flood”. One of the main advantages of this approach is that it is computationally relatively inexpensive and therefore suitable for rapid mapping purposes. Its results are usually reliable and commonly, most of the extent of an inundation area can be derived. The applicability of thresholding procedures for floodplain detection using SAR sensors depends on the contrast between the flood and non-flood areas. Its



Correspondence to: S. Martinis
(sandro.martinis@dlr.de)

results are satisfactory for calm water surfaces, which can be regarded as specular reflectors with low backscatter values. In contrast, the surrounding terrain usually exhibits higher signal return due to increased surface roughness. Elevated surface roughness of water bodies due to the influence of waves, precipitation as well as diffuse and double bounce reflection at vegetation reduces the class-separability and also complicates the determination of an appropriate threshold.

Since a flood separating threshold value depends on many factors such as environmental and, satellite system parameters, it can be highly variable and has to be determined individually for each satellite scene. In most cases thresholding based derivation of inundation areas from remote sensing data is generated by visual inspection of the image histogram and subsequent fine tuning of the threshold. However, such manual trial-and-error operations typically turn out to be relatively time consuming; additionally, the quality of their results highly depends on the visual interpretation and hence subjective impression of the operator. Therefore, such interactive threshold determination lacks objectivity and traceability. Automatic thresholding procedures can overcome these problems. In the context of automatic image thresholding, e.g. Sahoo et al. (1988), Pal and Pal (1993) and Bazi et al. (2007) provide extensive methodological reviews. Thresholding algorithms are either based on global information (e.g. gray-level histogram of the whole data set) or on local information (e.g. co-occurrence matrix) of an image. Independently of the used algorithm, the use of a single threshold for every image element in an entire data set is called global thresholding (Pal and Pal, 1993). On the other hand the partitioning of a data set into subregions and the derivation of a threshold value for each of these subimages is termed local thresholding (Sahoo et al., 1988).

Most parametric thresholding algorithms determine automatically the desired gray value which best separates two semantic classes under the assumption that the a priori probabilities of the class-conditional densities in a histogram are sufficient to properly model the class-distributions. The spatial flood extent, in combination with the spatial resolution and the coverage of the used satellite sensor determine the percentage of the inundated area within a satellite scene. Therefore the classes “flood” and “non-flood” may show quite different a priori probabilities when looking at the entire dataset compared to looking at a subset of it. This may reduce the capability of any global thresholding algorithm to detect an adequate threshold in the histogram, built from the large SAR scenes, because local gray-level changes may not be distinguished.

Due to these limitations a split-based approach (SBA) for unsupervised flood detection in SAR data is applied which originally has been proposed by Bovolo and Bruzzone (2007) for the identification of tsunami induced changes in multitemporal imagery. This approach comprises a tiling of the satellite imagery into smaller subscenes of user-defined size and a successive local thresholding analysis of a lim-

ited amount of splits with a high probability to contain large quantities of image elements of the classes “flood” and “non-flood”. Three thresholding approaches, all based on the KI minimum error thresholding algorithm (Kittler and Illingworth, 1986) are tested. Different combination techniques are applied to extract one global threshold from the analysis of the selected image splits. The global threshold is then integrated into a multi-scale segmentation process, which connects the advantages of small-, medium- and large-scale per parcel segmentation and hence should lead to a more accurate classification of the SAR data. Additionally, a high resolution digital elevation model (DEM) is used to improve the classification accuracy.

The effectiveness of the SBA in combination with subsequent classification refinement steps by multi-scale segmentation and DEM integration is analyzed using a large TerraSAR-X Stripmap scene from southwest England during a flood situation in July 2007.

The outline of the paper is as follows: in Sect. 2 the general SBA adapted to flood detection in SAR data is described. The application of the SBA to a TerraSAR-X scene of the River Severn (UK) and the subsequent classification refinement process is presented in Sect. 3. In Sect. 4, the results of the SBA by the use of three different automatic thresholding approaches as well as quality assessments of different refinement steps are reported. Finally, conclusions are drawn in Sect. 5.

2 A split-based automatic thresholding approach for unsupervised NRT-flood detection

2.1 Image tiling and split selection

The image-tiling technique divides a SAR scene X with dimensions R, C into N quadratic non-overlapping subimages X_n of user-defined size $s*s$. The selection of s and therefore N depends on the extent of the two classes “flood” and “non-flood” within X , and on the spatial resolution of the SAR scene. Due to the fact that the thresholding algorithms only extract proper thresholds values if the histogram is not unimodal, the selection process has to ascertain that the subscenes contain a distinct number of pixels from both classes. A minimum amount of 10% of each class seems to be sufficient for accurate threshold detection up to reasonable overlapped class mixtures according to empirical assumptions of Bazi et al. (2007) in automatic change detection. Appropriate splits are selected, combining the statistical properties of X and its subscenes. The coefficient of variation CV_{X_n} (ratio between the mean μ_{X_n} and standard deviation σ_{X_n} of the gray values of X_n) is used as an appropriate statistical measure to select splits with a wide data range. It serves as a measure of the degree of variation within the data and can therefore be used as an indicator of the probability that the splits contain more than one semantic class.

Erroneous selections may occur if a subset comprises both agricultural crop land and high reflecting urban areas. Thus, similar values of CV_{X_n} like for subsets containing the classes “flood” and “non-flood” are reached. A second measure R_{X_n} is added which selects the image splits in dependence of the ratio between the μ_{X_n} to the global intensity mean μ_X of X . This step prohibits the mis-selection of subsets comprising both agricultural crop land and urban areas characterized by similar values of CV_{X_n} as splits covering large parts of the classes “flood” and “non-flood”. Finally, the following data ranges have been derived by the investigation of several SAR data sets exhibiting flood situations for optimal split selection:

$$X_{n'} = \{X_n \mid CV_{X_n} \geq 0.7 \wedge R_{X_n} 0.4 \leq \dots \leq 0.9, n=1, \dots, N\}. \quad (1)$$

Optionally, ancillary data like vector layers containing the position of the land-water boundary at normal hydrological conditions may optionally be integrated into the split-selection process. This information is in most cases already readily available (e.g. SRTM water mask) or can be generated from pre-flood satellite archive scenes. The split-selection process may be restricted to these subimages intersecting the vector file. This reduces the probability of selecting split-elements not containing any water surfaces.

Out of the total set N' of subimages $X_{n'}$ which fulfils Eq. (1) a limited number N'' of subimages $X_{n''}$ is finally selected for the threshold computation. The value of N'' can be manually set by the user before starting the algorithm. This selection is made to constrain and equalize processing times independently from N' . This final selection is carried out by the computation of the Euclidean distance $\Delta CVR_{X_{n'}}$ within a 2-D feature space determined by $CV_{X_{n'}}$ and $R_{X_{n'}}$ between the points of the respective subset and the mean $\mu CVR_{X_{n'}}$ of the cluster of $X_{n'}$. The N'' elements with the lowest Euclidean distance are selected:

$$X_{n''} = \{X_1, X_2, \dots, X_{n'} \mid \Delta CVR_{X_1} \leq \Delta CVR_{X_2} \leq \dots \leq \Delta CVR_{X_{n'}}, n \leq N''\}. \quad (2)$$

If the case occurs that no splits are selected according to the predefined criterion, simultaneously the range of CV_{X_n} is decreased and R_{X_n} is increased stepwise by 0.05 until a minimum set of N'' splits is reached.

2.2 Automatic threshold selection procedure

The principal concept of using global thresholding algorithms for delineating flood zones in SAR intensity data is to assign all elements with a scattering cross-section lower or greater than a threshold τ to the class “flood” or “non-flood”, respectively. This means that a $R \cdot C$ dimensioned gray-scale image $X = \{x_{rc} : r=0, 1, \dots, R-1, c=0, 1, \dots, C-1\}$ with G possible gray-levels ($x_{rc}=g, g \in \{0, 1, \dots, G-1\}$) will be transformed according to $\tau \in \{0, 1, \dots, G-1\}$ into a binary

form $Y = \{y_{rc} : r=0, 1, \dots, R-1, c=0, 1, \dots, C-1\}$ with following values:

$$y_{rc} = \begin{cases} 1 & x_{rc} \leq \tau \\ 0 & x_{rc} > \tau \end{cases}, \quad (3)$$

where 1=flood, 0=non-flood.

Difficulties may arise within the global thresholding procedure if the illumination varies across the image due to incidence angle linked backscatter variances or atmospheric conditions. However, within TerraSAR-X data, especially Spotlight and Stripmap products, the system induced effect is marginally existent due to only small variations of the incidence angle from near- to far-range (3.562° maximum at a ground swath width of 31.638 km). Therefore these system-related backscatter variations can be neglected. Despite the fact that the all-weather imaging capabilities of SAR sensors are often emphasized in the literature, heavy precipitation in combination with the relatively short wavelength of the actively emitted X-band microwaves may cause artefacts which appear as dark patches due to the attenuation of the transmitted signal as well as bright objects due to partial backscattering at rain-cells. However, these effects are very rare and appear just locally. Likewise, these exceptions can be disregarded.

In this study three bi-level thresholding techniques are tested for the distinction between floodwater surfaces and non-flood areas. The first is the original KI algorithm itself. The second one computes the most prominent (global) minimum (GM) of the image histogram starting at the derived minimum error cutting point. The third approach uses an index function, combining the separability of the two distributions and the most dramatic change in the KI's criterion function, to obtain the optimal threshold by the use of a quality index (QI).

2.2.1 Kittler and Illingworth's algorithm

In this work the KI thresholding algorithm (Kittler and Illingworth, 1986) has been adopted, which has been used in remote sensing image analysis predominantly in modified versions for automatic change detection in difference or (log) ratio data (Bazi et al., 2005; Melgani et al., 2002; Bovolo and Bruzzone, 2007; Moser et al., 2006). This is a global parametric thresholding technique which uses a minimum error approach to group the sets of pixels of gray-scale images into object and background classes and assumes that the image histogram $h(g)$ which gives the frequency of occurrence of the various levels of g to be the only available information about the image. The histogram is viewed as an estimate of the class-conditional probability density functions of a mixture of two clusters. We assume that the histograms of the selected subimages $X_{n'}$ can be modelled statistically by two 1-D normal distributions of the semantic classes “flood” and “non-flood” $p(g|i), i=\{1: \text{flood}, 2: \text{non-flood}\}$, with param-

eters mean μ_i , standard deviation σ_i and a priori probability P_i , so that

$$p(g) = \sum_{i=1}^2 P_i p(g | i) \quad (4)$$

where

$$p(g | i) = \frac{1}{2\pi\sigma_i} e^{-(g-\mu_i)^2/2\sigma_i^2}. \quad (5)$$

Due to the fact that these parameters are usually not known in advance they have to be estimated at some arbitrary threshold level T which separates the two pixel populations with the following properties (Kittler and Illingworth, 1986):

$$P_i(T) = \sum_{g=a}^b h(g) \quad (6)$$

$$\mu_i(T) = \frac{\sum_{g=a}^b g * h(g)}{P_i(T)} \quad (7)$$

$$\sigma_i(T) = \frac{\sum_{g=a}^b (g - \mu_i(T))^2 * h(g)}{P_i(T)} \quad (8)$$

where $a=1$ if $i=flood$, $a=T+1$ if $i=non-flood$, $b=T$ if $i=flood$ and $b=G$ if $i=non-flood$.

The selection of an appropriate threshold τ is based on the optimization of a given predefined criterion function $J(T)$ that averages the cost function $c(g, T)$ over the histogram:

$$J(T) = \sum_{g=0}^{G-1} h(g)c(g, T) \quad (9)$$

The cost function measures the cost of classifying pixels by comparing their gray-levels with the threshold T . According to the number of brightness levels of an image up to G different threshold values can be tested in succession. For each brightness value, the fitting criterion $J(T)$ is calculated, which is defined by

$$J(T) = 1 + 2 [P_1(T) \log \sigma_1(T) + P_2(T) \log \sigma_2(T)] - 2 [P_1(T) \log P_1(T) + P_2(T) \log P_2(T)]. \quad (10)$$

As long as threshold T is varied, the models of the Gaussian distributions change. The better the model fits the data, the lower is the criterion of this cost function. Therefore, the brightness value T , which reduces the criterion function, is considered to be the optimal threshold τ_{KI} since at this position, the classification error is minimized according to the Bayes classification rule, i.e., the number of mis-segmented pixels is smallest:

$$\tau_{KI} = \arg \min_T J(T) \quad (11)$$

One has to note that τ_{KI} corresponds to the intersection point of the two Gaussian populations. If an overlap between the classes exists, as it is usually occurs in remote sensing data, the tails of these underlying distributions are truncated by the thresholding procedure and therefore the models $h(g | i)$ will be biased estimates of the true mixture components.

2.2.2 Global minimum thresholding

The second strategy used for automatic object-background separation is a bottom of the valley approach which locates, if existent, the most pronounced global minimum (GM) in a subhistogram. This belongs to the position between adjacent peaks of a bimodal histogram which often is chosen as a starting threshold in manual trial-and-error approaches by visual inspection of the image histogram. Based on the position of the threshold value τ_{KI} which is located between the two global maxima of a bimodal histogram the most pronounced valley between the two distributions “flood” and “non-flood” can be derived, primarily computing the direction in which the subhistogram declines in the surrounding of the start value τ_{KI} and moving step wise to this location τ_{GM} where the global minimum occurs.

2.2.3 Quality-index thresholding

The third method proposed for automatic partitioning of bimodal histograms derives the threshold according to a quality measure. For that purpose we use an index function $I[h(g)]$, introduced by Miasnikov et al. (2004) as a measure for the usefulness of bi-partitioning a 1-D projection of a dataset at the position of a computed threshold. $I[h(g)]$ is a composite measure containing a term *sep* describing the separability between the peaks of two distributions in relation to their means μ_i and variances σ_i^2 as well the term *depth* which accounts for the largest variation in KI's criterion function $J(T)$:

$$I[h(g)] = \text{sep} * \text{depth} \quad (12)$$

where

$$\text{sep} = \frac{(\mu_1 - \mu_2)^2}{\sigma_1^2 + \sigma_2^2}. \quad (13)$$

The depth of $J(T)$ is originally given by the difference between the value of $J(T)$ calculated at the minimum error threshold τ_{KI} and the closest local maximum $J(T_{\max})$ of the KI function. In this study $I[h(g)]$ is used for the search of the threshold τ_{QI} which best separates the class distributions “flood” and “non-flood”. This is identical to the position where $I[h(g)]$ is maximized:

$$\tau_{QI} = \arg \max I[h(g), T] \quad (14)$$

The calculation of the closest local maximum is accomplished for each of the two class peaks of $J(T)$ separated by the calculated global minimum at τ_{GM} .

2.2.4 Split combination techniques

To derive a spatially coherent binary flood mask without any discontinuance at the borders of adaptively thresholded splits one global reliable threshold is used for classification.

For its calculation two approaches can be applied using the split inherent information (Bovolo and Bruzzone, 2007):

mathematical combination techniques of (sub)histogram derived thresholds and a (sub)histogram-merging strategy with subsequent thresholding.

The principal concept of the first method is to compute for every (sub)histogram of the selected splits $X_{n''}$ a local threshold τ_{loc} by any of the proposed KI, GM or QI thresholding algorithms. To obtain a global threshold τ_{glob} which is used for the classification of X simple mathematical operations can be applied; e.g. the computation of the median or the arithmetic mean. Due to the fact that all values of the variables are integrated with the same weight within the computations, the arithmetic mean contains more information than the median. However, it is more sensitive to outliers appearing just at one side of the range of values, especially in the presence of just a few samples. This may produce improper final threshold values due to the limited number N'' of selected splits $X_{n''}$, even if a robust split-selection procedure is applied.

The second method avoids the use of mathematical combination techniques by computing τ_{glob} directly from a merged histogram which is a combination of the distributions of the individual splits $X_{n''}$. However, the accuracy of the threshold selection may be reduced by differences in the statistical properties of the class-distributions in the respective splits.

3 Application for high resolution TerraSAR-X data at the River Severn, UK

In this section the unsupervised flood detection approach is applied exemplarily to a TerraSAR-X data set acquired during heavy floods in southwest England at the River Severn in 2007. The proposed workflow (Fig. 1) contains the SBA for automatic threshold computation of the pre-processed SAR scene as well as a classification refinement process including a multi-scale segmentation and an optional DEM integration step.

3.1 Data set

A period of heavy precipitations over the Gloucestershire Region in Southwest England during the summer season 2007 caused severe flooding at the River Severn. The record flood level at Tewkesbury was measured at 5.43 m on 22 July 2007 which was 0.13 m above the previously highest record from the year 1947. The proposed SBA is applied on a TerraSAR-X Stripmap scene (Fig. 2a) with 3.25 m pixel spacing in range and azimuth direction showing the flood situation along a section of about 69 km length of the River Severn on 25 July 2007 (06:34:08 UTC) including the confluence of River Avon coming from northeast. The data are HH polarized, which is the favoured polarization in flood mapping, because it provides the most obvious discrimination between open water and non-flood areas since it is less sensitive to small scale roughness of waves on the water surface than VV like-polarisation or cross-polarisations (Henry et al., 2006).

At the time of the satellite overpass there was no precipitation and low wind speed (16.5 km/h). Additionally, two ancillary data sets are available for this study: orthorectified aerial photographs with a spatial resolution of 0.2 m recorded about half a day prior to the TerraSAR-X overpass (24 July 2007 between 13:10:00 and 15:40:00 UTC) by a Rollei Modular AIC as well as a LiDAR-DEM with a horizontal resolution of 2 m and a vertical accuracy of 0.1 m.

3.2 Pre-processing

A preliminary despeckling was performed by adaptive filtering to reduce salt-and-pepper structures within the data. The speckle appearing on SAR imagery is a natural phenomenon generated by the coherent processing of radar echoes (Lee, 1986). Its presence not only reduces the interpreter's ability to resolve fine details, but also makes automatic segmentation of such noisy images difficult. For this purpose the Gamma-MAP filter (Lopes et al., 1990) was chosen because it comprises a good trade-off between the quality of the filtering result and the computation time. The filtering was accomplished by a mask-size of 3×3 pixels, which seems to be a sufficient size for this data set.

For validation purposes of the results of the proposed SBA and refinement process a reference map was created for a small subset (approx. 5.4×10^6 pixels) of the TerraSAR-X scene by visual interpretation and manual digitisation of the orthophotos, which is covered by 23.8% of the class "flood" and 76.2% of the class "non-flood". The subset of the reference scene (see Figs. 2a and 5a) was chosen based on the overlap between the SAR data, the aerial images and the DEM. It comprises the heavily flooded Tewkesbury region.

3.3 Split-based approach

The SBA is applied to a TerraSAR-X scene X with dimensions of $R=14\,461$, $C=20\,153$ pixels. According to a split size of $s=500$, X is tiled into 1187 subimages, whereof a quantity N of 637 subimages contains no pixels with no-data values. An amount of $N'=7$ splits (Fig. 2a and b) were selected out of N according to the criterion defined in Eq. (1). These remaining subscenes are considered as suitable for effective threshold detection. This assumption can be confirmed by the fact that selected subimages intersect the visually detectable land-water boundary (see Fig. 2a). Out of N' a fixed number of $N''=5$ splits are sorted out according to Eq. (2) to perform the final threshold selection (Fig. 2a and b). The three proposed thresholding algorithms (KI, GM and QI) are applied to the five splits and different combination techniques for the derivation of one global threshold are executed. The performing of the thresholding algorithms as well as the results is presented in Fig. 3 exemplarily by split X'_4 . For this split the KI algorithm computes a threshold value $\tau_{KI}=26$ where $J(T)$ reaches its minimum. Based on τ_{KI} the global minimum $\tau_{GM}=29$ of the histogram is localised. The

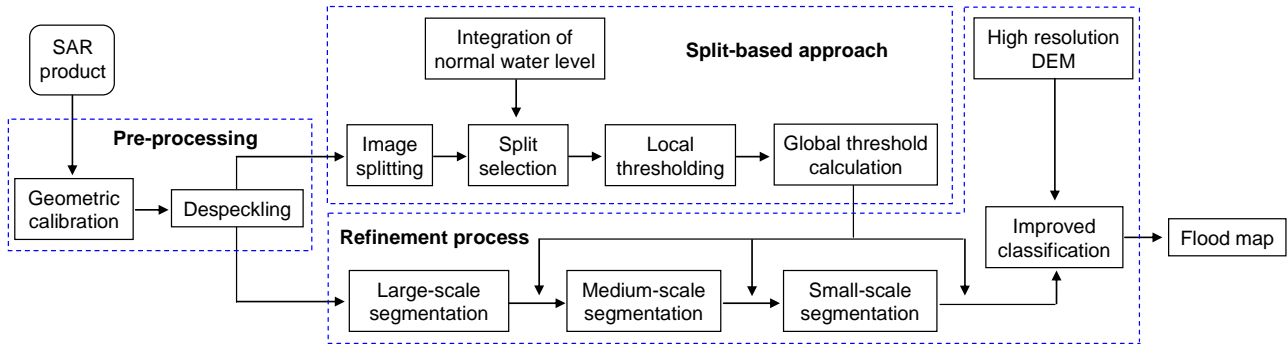


Fig. 1. Block scheme of the proposed workflow for automatic flood detecting within large SAR satellite data.

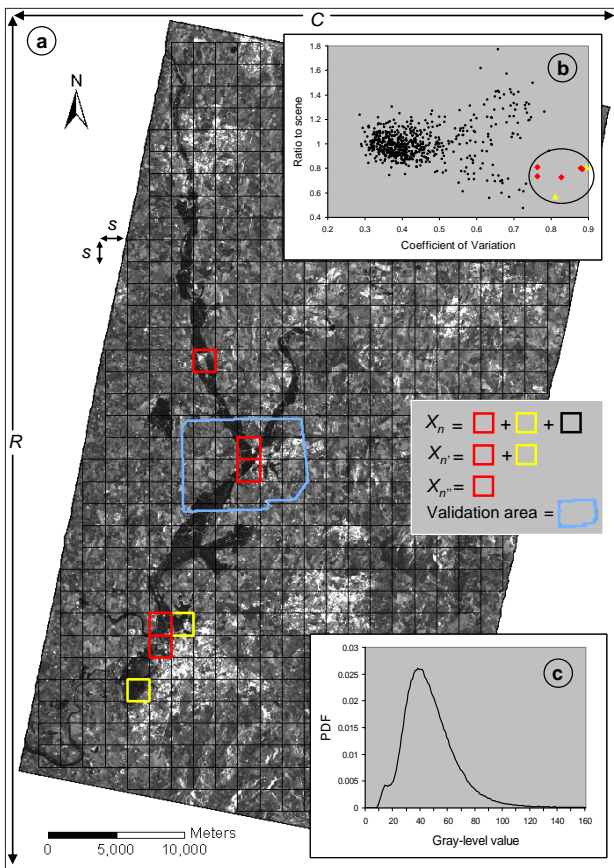


Fig. 2. (a) TerraSAR-X data of the River Severn (25 July 2007) with splits X_n , $X_{n'}$ and outline of the validation area, (b) Location of X_n , $X_{n'}$ and $X_{n''}$ within the feature space (CV_{X_n}/R_{X_n}), (c) PDF of X .

criterion function derived by the KI algorithm as well as τ_{GM} are used to calculate the threshold position $\tau_{QI}=28$ where the index function reaches its maximum.

3.4 Classification refinement process for unsupervised flood detection

The classification refinement process has the purpose to improve the accuracy of the classification result derived by global thresholding. It consists of two main parts: a multi-scale segmentation and an optional DEM integration step.

3.4.1 Multi-scale segmentation

Pixel-based and segmentation-based classification techniques can be considered as main concepts for the identification of flooded areas in radar imagery. Conventional classification approaches use pixels as smallest geometrical components of raster data. However, the parameters which can be employed for the classification are limited. Additionally, pixel-based classifiers do not make use of spatial information of the image and are thus not suited in cases where land cover units are composed of spectrally heterogeneous elements. By the use of segmentation techniques, some disadvantages of pixel-based image thresholding can be solved. Image segmentation partitions an image into uniform regions based on similarity criteria of gray values or textural properties (Meinel and Neubert, 2004). The created homogeneous, non-overlapping segments have a strong correlation with real objects or areas of the earth's surface. Due to the increasing spatial resolution of earth observation imagery per-parcel approaches gain in importance in the field of remote sensing image analysis. Especially for data of the new generation of SAR sensors with up to one meter pixel spacing (TerraSAR-X, COSMO-SkyMed) the use of segmentation-based methods appears promising. These images can exhibit very high spectral variances within a given thematic class due to both the reduced mixed pixel phenomenon and the SAR intrinsic speckle effect. In addition to spectral related characteristics of the image objects further parameters such as contextual information, texture and object geometry can be used for improving classification accuracy.

However, the quality of the classification result depends on the properties of the calculated image segments. Gener-

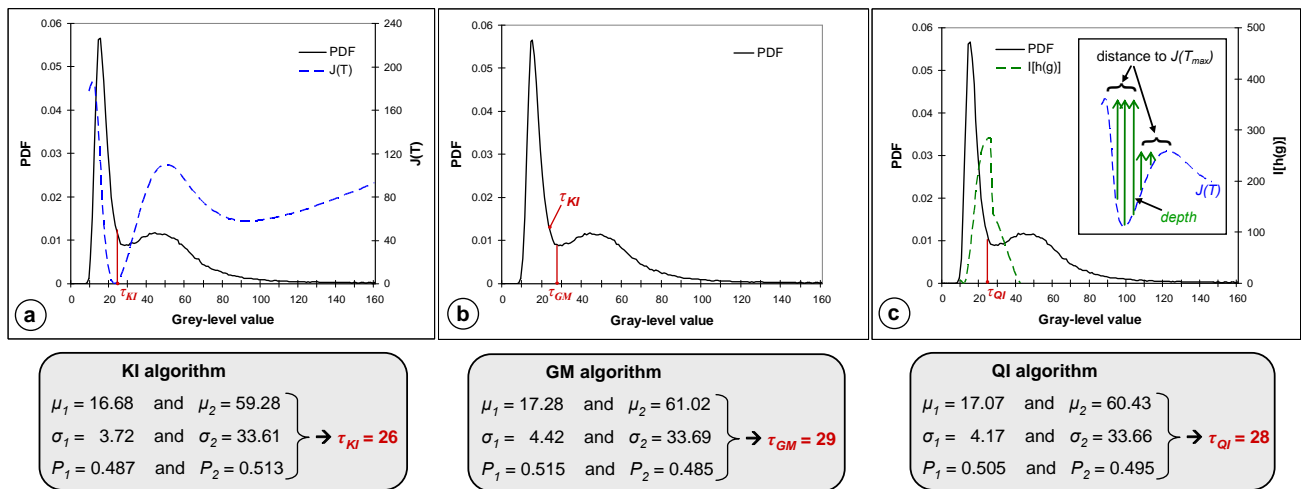


Fig. 3. Histogram of split X_i and derived threshold values by the use of the (a) criterion function of the KI algorithm, (b) GM algorithm, (c) Index function of the QI algorithm.

ally, high homogeneity segmentation parameters cause small segments, which, similar to pixel-based classifiers, produce noisy classification results but are able to detect small objects, whereas low values of the homogeneity criterion generate large segments at the expense of fine detail. Therefore, segmentation algorithms connecting the advantages of multi-scale segmentation and per-parcel classification by automatic thresholding seem promising for improved flood mapping.

Image objects were created using the Fractal Net Evolution concept of the Definiens Developer software (Batz and Schäpe, 1999; Definiens AG, 2008). An iterative bottom-up segmentation algorithm based on a pair wise region merging technique is employed to segment the image according to the maximum allowable heterogeneity of the image objects, defined by an initially set scale parameter. This scale parameter is a homogeneity criterion h combining spectral h_c and shape homogeneity h_s , with h_s being composed of the smoothness $h_{compact}$ and compactness h_{smooth} . The fusion of the objects within the segmentation process follows the local mutual best fitting algorithm. This leads to the lowest increase of object heterogeneity by merging two adjacent objects which exhibit the lowest distance in a feature space determined by mean spectral values or texture features. For classification refinement we developed an approach containing a threefold processing step which alternates multi-scale segmentation and classification by the SBA-derived global threshold τ_{glob} :

1. Large-scale segmentation step and thresholding by τ_{glob} .
2. Medium-scale segmentation of objects of class “non-flood” and thresholding by τ_{glob} .
3. Small-scale segmentation of objects of class “non-flood” and thresholding by τ_{glob} .

Step 1 partitions the input data X into an initial set of large image objects containing some variations in the spectral properties of the merged pixels. Subsequently, the created objects are thresholded by τ_{glob} . Most of the inundation area is classified by this step, however fine tuning is reached by the following two steps, progressively enforcing the spectral homogeneity constraints of non-flood objects in a defined neighbourhood around flood objects and thresholding by τ_{glob} . A scale parameter of $h=75$ (unitless) was selected for the initial segmentation of X in step 1 based on visual interpretation of the image segmentation results with different scale parameters. This value was considered appropriate as reaching the best compromise between maximal possible heterogeneity and minimal homogeneity within the resultant object primitives, leading to an average object size of 2995 pixels. Steps 2 and 3 were performed by a reduced scale parameter of $h=40$ (average object size: 908 pixels) and $h=5$ (average object size: 16 pixels) respectively to detect fine detailed flood objects. The composition of homogeneity was controlled by both spectral and shape properties. Spectral homogeneity was set to an overall spectral factor of $h_c=80\%$. Shape-homogeneity criteria included an overall shape factor of $h_s=20\%$, which was subdivided into smoothness ($h_{smooth}=10\%$) and compactness ($h_{compact}=10\%$). Medium- and small-scale segmentation was accomplished within a distance of max. 5 objects and 1 object respectively to the class “flood”. This restriction prohibits the flood mapping of medium- and small-scale image elements with too large distance from the flood objects and additionally reduces the computational requirements of the segmentation. The settings for the scale parameter h , h_c / h_s and $h_{smooth} / h_{compact}$ are defined as constants so that they need not be set by the user.

3.4.2 DEM integration

We observe that thresholding is capable of detecting the majority of flooded surfaces in X , but there are multiple areas of relatively high backscatter surrounded by flood objects, which are flooded with high probability but interpreted as non-flooded. These areas correspond predominantly to flooded surfaces which are broken by emergent vegetation. With X-band SAR flooded and non-flooded vegetation with a closed canopy can hardly be differentiated, due to very similar radar cross-sections. Additionally, some wrongly labelled flood regions exist with a small surface roughness and therefore low backscatter characteristics similar to calm water like streets, smooth agricultural crop land or radar shadow. For a hydrological plausible improvement of the classification result the topographic information of a high resolution DEM is added into the classification process as it can be used to extract flooding under dense vegetation and forest cover (e.g. Wang et al., 2002; Mason et al., 2007) and within residential areas. The proposed approach is appropriate for floods primarily caused by over-bank flow; predominantly affecting areas connected to the main river channel and also can be applied if no river gauge readings are available for hydraulic floodplain modelling. A prerequisite for this method is that major parts of the flood surface are already detected by the automatic thresholding step, thus a spatially coherent flood surface can be derived. The classification procedure using the DEM can be separated into two parts: an inclusion and an exclusion step. During the inclusion step, topography information can be used in combination with contextual information to classify potentially flooded objects with backscatter intensities higher than the originally defined threshold, e.g. protruding vegetation or urban areas into the flood class. First, all classified flood objects without any conjunction to the core flood area and exceeding a predefined elevation H are temporarily excluded from the classification result:

$$H = \left(\sum_{s_f=1}^{S_f} S_h / S_f \right) + 1.5 * \sigma_{S_h} \quad (15)$$

where S_f is the number of flood objects, S_h the elevation of each single flood object and σ_{S_h} the standard deviation of S_h .

After that, an iterative classification process is performed considering local neighbourhood relations: If an object of the main flood area is found next to a non-flood object the height distance between the non-flood objects and the surrounding flood objects is calculated. In the case that the mean altitude of the non-flood object is lower or equal than the elevation of the contiguous flood objects, the non-flood object is recoded as flooded area. This processing step is repeated until no further non-flood object fits to this criterion. In case microtopographic features exist (e.g. embankments, walls) that may prevent flooding of areas at lower elevations, the integration of objects stops if these obstructions with higher elevations are detected as non-flood objects. If the segmentation fails

to delineate such objects or the resolution of the DEM is too coarse classification errors may occur in this processing step.

At the exclusion step, wrongly masked objects in regions with higher elevation than the main flood area can be eliminated. However, due to the fact that most parts of the floodplain are connected to the main river channel which is a body of flowing water, the altitude of the land-water boundary decreases downstream. Therefore using a global threshold for the exclusion step is not effective and a value which is representative for each position along the river is required instead. Accordingly, the altitude of every single flood object without connection to the main expanse of the flood area is compared to the altitude of the nearest object of the core flood area and removed from the mapping result if it exceeds a height difference of 1.0 m. This value was chosen to account for slightly higher objects which should be retained due to local variations in water height caused by the dynamic nature of floods.

4 Results

In this section, the performance of the proposed automatic approach of unsupervised threshold selection as well as the subsequent classification refinement process containing threefold image segmentation and an optional DEM integration are assessed.

The results of the threshold computations by the use of the KI, GM and QI algorithm are presented in Table 1. It was possible to model the histogram of each selected split by a mixture of two Gaussian distributions. Thus, by any of the applied algorithms a threshold value could be derived. In comparison, no decision threshold could automatically be identified from the histogram of X (Fig. 2c) because of the small a priori ratio at the visual detectable global minimum between the class “flood” ($P_1=0.023$) and “non-flood” ($P_2=0.977$), and the nearly unimodal distribution of the data set.

The local threshold positions of the selected subscenes computed by the KI, QI and GM algorithms exhibit slightly different values. This results from the varying class-statistical properties in the respective splits. The results derived by the QI algorithm are characterized by the lowest range of threshold values (26.0 to 29.0) which indicates less sensitivity to class statistics. A total amount of nine global threshold values (Table 1) have been derived by combining the three thresholding algorithms (KI, GM, QI) with three different split combination techniques (cf. Sect. 2.2.4), leading to seven different values of τ_{glob} in the range of 22.6 to 29.0. According to this a subset of X (see Fig. 2a), for which the real flood extent is known, has been classified by these seven thresholds with different segmentation adjustments:

- P: chessboard segmentation with an object size of 1 pixel ($\hat{=}$ pixel based application);

Table 1. Local thresholds computed by the KI, GM and QI algorithm for splits $X_{n''}$ and global thresholds derived by the use of different split combination techniques.

Thresholding approach	Subscene $X_{n''}$					(sub)histogram threshold combining		(sub)histogram-merging
	$X_{1''}$	$X_{2''}$	$X_{3''}$	$X_{4''}$	$X_{5''}$	Mean	Median	
KI	25	21	17	26	24	22.6	24.0	23.0
GM	29	26	23	29	29	27.2	29.0	29.0
QI	26	27	29	28	26	27.2	27.0	25.0

- L, M, S: uni-scale segmentation at large-, medium- or small-scale;
- L-M: bi-scale segmentation at large- and medium-scale;
- L-M-S: tri-scale segmentation at large-, medium- and small-scale;
- L-M-S-DEM: tri-scale segmentation with subsequent DEM integration.

In Fig. 4 the accuracy assessment of the SBA and the classification refinement steps for each threshold value is illustrated by the missed alarm rate (MDR; i.e. the percentage of flood reference pixels erroneously detected as non-flooded), false alarm rate (FAR; i.e. the percentage of non-flood reference pixels erroneously detected as flood) and overall error rate (OER; i.e. the percentage of erroneously labelled reference pixels). Generally, a trend can be stated that a rise of the threshold value simultaneously is related to an increase of the FAR and a decrease of the MDR. Thus, reduction of false and missed alarms become two partially conflicting objectives. Regarding the classification accuracy of every single threshold derived by the SBA, pixel-based thresholding in all cases produces higher OERs than segmentation-based classification. This observation can be explained by the huge amount of false alarms which cannot be compensated by a low quantity of missed alarms in relation to uni-scale and bi-scale segmentation for $\tau_{\text{glob}}=22.6$ to 27.2 . Large-scale segmentation (L) yields much better results than small- (S) and medium-scale (M) image decomposition due to the highly reduced number of false alarms which exceed the rise in missed alarms. These missed alarms of L further are strongly reduced by L-M and more considerably by L-M-S, due to the fact that finer details on medium- and small-scale level are identified as flooding in a defined neighbourhood of large-scale flood objects.

L-M-S leads to lowest OERs by classification without ancillary data due to the fact that it combines the advantages of small-scale (low number of missed alarms) and large-scale (low number of false alarms) segmentation.

The integration of topographic information within the classification process of the tri-scale segmentation additionally reduces the percentage of the MDR. This results in the

best classification accuracy of L-M-S-DEM out of all segmentation adjustments for all determined threshold values.

When comparing the scale-dependent classification results of the individual threshold values, the minimum pixel-based OER (8.68%) appears at $\tau_{\text{glob}}=23.0$, which corresponds to the threshold position derived by the KI algorithm applied to the mixed pixel population of the merged (sub)histograms of $X_{n''}$. In contrast values of $\tau_{\text{glob}} <$ and > 23.0 ($\tau_{\text{glob}}=22.6$) show higher pixel-based OERs.

The difference in OER between P and L-M-S increases with rising threshold values. Additionally, by the use of segmentation, the range of OER between the different threshold values can be reduced. For example the range between the highest and lowest OER at pixel-based classification reaches 3.83% whereas the overall error of L, L-M, L-M-S and L-M-S-DEM just varies between 0.30% and 0.17%. This means that independent of the applied thresholding algorithm and split-combination technique, the variation of the classification accuracy can be reduced by appropriate segmentation. Thus, the method chosen for automatic thresholding is less critical when applied to segmented data. Lowest classification errors for M, L, L-M, L-M-S and L-M-S-DEM are reached when $\tau_{\text{glob}}=25.0$, which also produces the best total classification result (OER: 4.55%) at L-M-S-DEM. The threshold value of 25.0 is reached by the QI algorithm applied to the histogram of the merged distributions of $X_{n''}$. The highest of the derived threshold values ($\tau_{\text{glob}}=29.0$) also results in the highest OERs for every classification result without DEM integration due to a high FAR. This threshold has been computed by the GM algorithm in combination with (sub)histogram merging. The threshold value is overestimated due to the loss of a clear global minimum in the data set by the combination of the different class populations of $X_{n''}$. However, using $\tau_{\text{glob}}=29.0$, the OER comes close to the best classification result at L-M-S-DEM. This is due to the following facts: the relatively high OER of 7.52% at L-M-S is fairly reduced by the exclusion step of the DEM integration process and the largest amount of correctly classified pixels at L-M-S (MDR: 3.46%) generates a more compact core flood area, which helps to identify more easily flooded vegetation and anthropogenic objects during the DEM integration step.

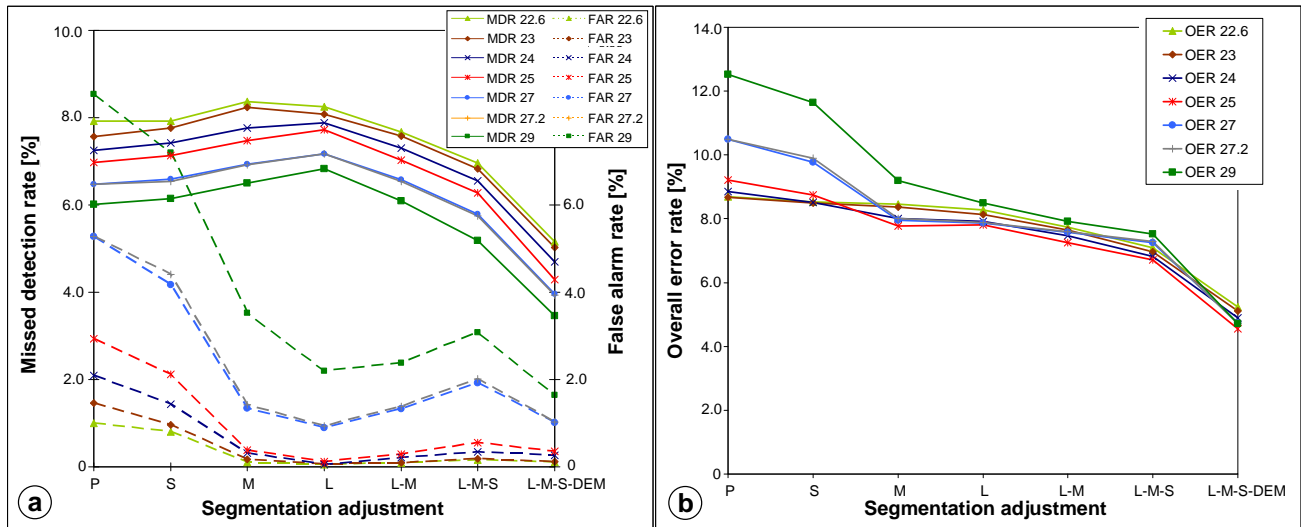


Fig. 4. (a) MDR and FAR for class flood and (b) OER calculated for the resultant global threshold values by the use of different segmentation scales.

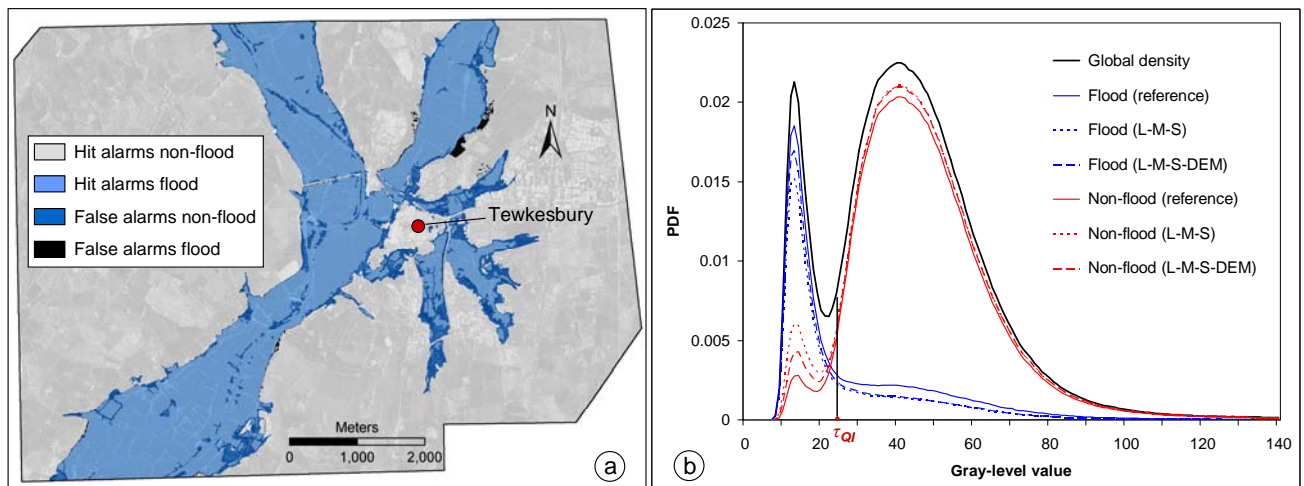


Fig. 5. (a) Classification result by thresholding with $\tau_{glob}=25$ derived from the merged histogram of X_n with L-M-S-DEM by the QI algorithm (b) global density function of the reference subset as well as class-conditional density functions of “flood” and “non-flood” of the reference data and of thresholding results P (global density function separated by the vertical black curve), L-M-S and L-M-S-DEM.

The final flood map for the subset of X obtained by L-M-S-DEM with a threshold of $\tau_{glob}=25.0$ is shown in Fig. 5a. The producer’s accuracy reaches 82.01%, the user’s accuracy 98.65% and the overall accuracy is 95.44%. This is a good result with overall accuracies considerably higher than commonly reported on the literature, which rarely reaches 90%. The result shows a coherent flood surface without salt-and-pepper-effects and a good representation of the land-water boundary due to multi-level segmentation. Additionally, compared to pure per-pixel classification, less image el-

ements are classified outside the floodplain. The remaining errors in waterline position found at the riverbanks are either due to emergent vegetation or caused by a slight decrease of the flood extent between the acquisition of the orthophotos (water level at Mythe gauge: 12.49 ± 0.05 m a.s.l.) and the SAR data (water level at Mythe gauge: 12.22 ± 0.05 m a.s.l.), whereas emergent hedges between adjacent flooded fields are predominantly labelled as “flood”. Some objects within the floodplain are not detected by the classification with DEM integration due to some remaining artifacts in the LiDAR to

pography information such as short vegetation, which cause overestimations of the real ground surface elevation. False alarms just appear at the boarder of the extracted flood extent. These are related to crop fields with short vegetation which show a similar spectral characteristic as water areas. Due to the fact that the DEM exclusion step only removes objects at higher elevations without connection to the main flood area, these regions initially labelled as main flood could not be deleted.

Generally, the algorithm performs very well in rural areas. In the partly flooded Tewkesbury town, however, only some larger regions could be detected as flooded. These are areas which are not brightened by double bounce effects as well as contributions from side-lobes of strong reflectors and therefore can be detected due to their intensity value below the derived threshold. Supervised methods with a considerable amount of user interaction are necessary to perform a more accurate classification in urban areas using SAR data (Mason et al., 2008).

It is assumed that the obtained classification accuracy could be slightly increased if the flood extent extracted from the SAR data and from the aerial photos would be fit to one another. An estimation of the flood extent at the satellite overpass time was done by Mason et al. (2008) for the same SAR scene by linearly interpolating between the aerial photo flood extent on 24 July and the flood extent of 27 July derived from aerial photos acquired on a second flight campaign. Due to the fact that the aerial photos of the 27th were not at our disposal during our investigations, no such correction could be accomplished.

The advantage of segmentation-based thresholding is also apparent if the class distributions derived from pixel- and object-based flood detection are compared (Fig. 5b): the class distributions derived by pixel-based thresholding according to $\tau_{\text{glob}}=25.0$ show a rigorous truncation of the right tail of the class flood and of the left tail of the class “non-flood” whereas the populations derived by thresholding of the segmented image with L-M-S and especially L-M-S-DEM come closer to the shape of the reference classes’ distributions. This is due to the fact that the segmentation process also integrates image elements above the selected threshold into a homogeneous image object in dependence of the chosen homogeneity criterion. Thus, besides pure spectral information derived by histogram thresholding, also topological information is made available for classification.

5 Conclusions

A split based automatic thresholding and classification refinement process has been applied as a test case to a TerraSAR-X Stripmap scene of the River Severn, UK, for unsupervised flood detection in large high resolution single-polarized SAR data sets. This approach already has successfully been applied in operational rapid mapping activities.

The proposed method tiles a SAR image into a set of segments and automatically selects a fixed number of splits according to their probability to comprise adequate portions of both classes “flood” and “non-flood”. To derive one global threshold by the analysis of the split inherent information mathematical combination techniques of (sub)histogram derived thresholds as well as (sub)histogram-merging strategies with subsequent thresholding have been analyzed. All three thresholding strategies (KI, GM, and QI) were able to determine a threshold value by the analysis of the histogram of every single selected split and of the merged class-populations of the individual splits, respectively.

The following results could be derived by thresholding a reference subscene decomposed by different segmentation adjustments: object-based context-sensitive thresholding has proven superior to pixel-based context-insensitive procedures due to the addition of spatial information to the pure spectral information derived from histogram thresholding. Lowest OERs could be obtained by a threefold segmentation step which consists of an alternating multi-scale image decomposition and thresholding approach that combines the advantages of small-, medium- and large-scale object generation. By the use of image segmentation, the variation in OER for the classification results derived by different threshold values can be fairly reduced in comparison to pixel-based thresholding approaches. Thus, the classification results of decomposed images are less sensitive to the used threshold algorithm as well as the applied split combination technique. Lowest OERs could be achieved by combining the KI algorithm with the (sub)histogram merging strategy whereas for the image segmentation adjustments M, L, L-M, L-M-S, L-M-S-DEM greatest classification accuracies could be achieved by a higher threshold value derived by the QI algorithm in combination with the (sub)histogram merging strategy.

High resolution topographic information has been successfully combined with multi-scale segmentation to enhance the mapping performance in areas that partly consist of flooded vegetation and anthropogenic objects as well as to remove non-water look-alike areas.

Experimental results of the SBA have shown that it is computationally more efficient than global threshold derivation by the use of the whole SAR scene. This is due to the fact that the most time-consuming step of global threshold detection is the computation of the image histogram which depends on the number of pixels of the analyzed data. In contrast the KI thresholding procedure is very fast, as no iterations are needed, but only the calculations of the criterion function for a defined gray-level range. The processing times of the GM and QI algorithm are nearly identical to the computational speed of the KI algorithm because only some additional calculations are needed to determine τ_{GM} and τ_{QI} , respectively. The computation can be accelerated if the position of the threshold can be restricted a priori. Due to the fact that the criterion function may have local minima at the

boundaries of the histogram meaningless thresholds can be avoided by a constraint of the loop. The computational effort of the SBA (less than 10 s for the entire scene on an Intel Xeon 5160 CPU with 3.0 GHz and 3 GB of RAM) is much lower than the refinement process by image segmentation, whose processing time rises according to the number of used segmentation-scales (160 s at L-M-S-DEM for the selected validation area). Therefore, the interpreter has to find a compromise between computational effort and classification quality.

The presented thresholding algorithm works successful in most of the cases, due to the fact that there is usually a sufficient contrast between the land and water surface. Future work will be related to extract the flood extent from roughened water surfaces.

Acknowledgements. Most part of this work is funded by the German Ministry of Education, Science, Research and Technology (BMBF) in the context of the Research Programme “Risk Management of Extreme Flood Events” (RIMAX), project SAR-HQ (grant reference number: 0330719). The authors thank the Environment Agency of England and Wales for providing the LiDAR DEM and aerial photography of the Tewkesbury region. They are also grateful to Guy Schumann and an anonymous reviewer for their helpful comments.

Edited by: B. Merz

Reviewed by: G. Schumann and another anonymous referee

References

- Baatz, M. and Schäpe, A.: Object-oriented and multi-scale image analysis in semantic networks, in: Proceedings of the 2nd International Symposium on Operationalization of Remote Sensing, Enschede, Netherlands, 16–20 August 1999.
- Bazi, Y., Bruzzone, L., and Melgani, F.: An unsupervised approach based on the generalized Gaussian model to automatic change detection in multitemporal SAR images, *IEEE T. Geosci. Remote*, 43, 874–887, 2005.
- Bazi, Y., Bruzzone, L., and Melgani, F.: Image thresholding based on the EM algorithm and the generalized Gaussian distribution, *Pattern Recogn.*, 40, 619–634, 2007.
- Bovolo, F. and Bruzzone, L.: A split-based approach to unsupervised change detection in large-size multitemporal images: Application to tsunami-damage assessment, *IEEE T. Geosci. Remote*, 45, 1658–1669, 2007.
- Brivio, P. A., Colombo, R., Maggi, M., and Tomasoni, R.: Integration of remote sensing data and GIS for accurate mapping of flooded areas, *Int. J. Remote Sens.*, 23, 429–441, 2002.
- Chen, P., Liew, S. C., and Lim, H.: Flood detection using multitemporal Radarsat and ERS SAR data, in: Proceedings of the 20th Asian Conference of Remote Sensing, Hong Kong, China, 1185–1189, 22–25 November 1999.
- Definiens AG: Definiens Developer 7 User Guide, Document Version 7.0.5.968, Munich, Germany, 2008.
- Henry, J. B., Chastanet, P., Fella, K., and Desnos, Y. L.: ENVISAT multi-polarised ASAR data for flood mapping, *Int. J. Remote Sens.*, 27, 1921–1929, 2006.
- Kittler, J. and Illingworth, J.: Minimum error thresholding, *Pattern Recogn.*, 19, 41–47, 1986.
- Lee, J. S.: Speckle suppression and analysis for SAR images, *Opt. Eng.*, 25, 636–643, 1986.
- Lopes, A., Nezry, E., Touzi, R., and Laur, H.: Maximum A Posteriori speckle filtering and first order texture models in SAR images, International Geoscience and Remote Sensing Symposium (IGARSS), Maryland, USA, 2409–2412, 24–28 May 1990.
- Mason, M. S., Horritt, J. T., Dall’Amico, Scott, T. R., and Bates, P. D.: Improving river flood extent delineation from synthetic aperture radar using airborne laser altimetry, *IEEE T. Geosci. Remote*, 45, 3932–3943, 2007.
- Mason, M. S., Speck, R., Schumann, G., Neal, J., and Bates, P. D.: Using TerraSAR-X data for improved urban flood model validation, in: Proceedings of the 3rd TerraSAR-X Science Team Meeting, DLR Oberpfaffenhofen, Germany, 25–26 November 2008.
- Matgen, P., Schumann, G., Henry, J. B., Hoffmann, L., and Pfister, L.: Integration of SAR derived river inundation areas, high-precision topographic data and a river flow model toward near real-time flood management, *Int. J. Appl. Earth Obs.*, 9(3), 247–263, 2007.
- Meinel, G. and Neubert, M.: A comparison of segmentation programs for high resolution remote sensing data, in: Proceedings of the ISRPS Annual Conference, Istanbul, Turkey, 19–23 July 2004.
- Miasnikov, A. D., Rome, V., and Haralick, R. M.: A hierarchical projection pursuit clustering algorithm, in: Proceedings of the 17th International Conference on Pattern Recognition, Cambridge, England, 268–271, 23–26 August 2004.
- Melgani, F., Moser, G., and Serpico, S. B.: Unsupervised change-detection methods for remote-sensing images, *Opt. Eng.*, 41, 3288–3297, 2002.
- Moser, G. and Serpico, S. B.: Generalized minimum-error thresholding for unsupervised change detection from SAR amplitude imagery, *IEEE T. Geosci. Remote*, 44, 2972–2982, 2006.
- Nico, G., Pappalepore, M., Pasquariello, G., Refice, S., and Samarelli, S.: Comparison of SAR amplitude vs. coherence flood detection methods – a GIS application, *Int. J. Remote Sens.*, 21, 1619–1631, 2000.
- Pal, N. R. and Pal, S. K.: A review on image segmentation techniques, *Pattern Recogn.*, 26, 1277–1294, 1993.
- Sahoo, P. K., Soltani, S., Wong, A. K. C., and Chen, Y. C.: A survey of thresholding techniques, *Comput. Vision Graph.*, 41, 233–260, 1988.
- Townsend, P. A.: Estimating forest structure in wetlands using multitemporal SAR, *Remote Sens. Environ.*, 79, 288–304, 2002.
- Wang, Y., Colby, J. D., and Mulcahy, K. A.: An efficient method for mapping flood extent in a coastal floodplain using Landsat TM and DEM data, *Int. J. Remote Sens.*, 23, 3681–3696, 2002.

5.2 Paper 2

Martinis, S., Twele, A. & Voigt, S., 2011: Unsupervised extraction of flood-induced backscatter changes in SAR data using Markov image modeling on irregular graphs. – IEEE Transactions on Geoscience and Remote Sensing, DOI 10.1109/TGRS.2010.2052816, (in print).

© 2010 IEEE. Reprinted, with permission, from IEEE Transactions on Geoscience and Remote Sensing.

This material is posted here with permission of the IEEE. Such permission of the IEEE does not in any way imply IEEE endorsement of any of the Ludwig-Maximilians-University of Munich's products or services. Internal or personal use of this material is permitted. However, permission to reprint/republish this material for advertising or promotional purposes or for creating new collective works for resale or redistribution must be obtained from the IEEE by writing to pubs-permissions@ieee.org. By choosing to view this material, you agree to all provisions of the copyright laws protecting it.

Unsupervised Extraction of Flood-Induced Backscatter Changes in SAR Data Using Markov Image Modeling on Irregular Graphs

Sandro Martinis, André Twele, and Stefan Voigt

Abstract—The near real-time provision of precise information about flood dynamics from synthetic aperture radar (SAR) data is an essential task in disaster management. A novel tile-based parametric thresholding approach under the generalized Gaussian assumption is applied on normalized change index data to automatically solve the three-class change detection problem in large-size images with small class *a priori* probabilities. The thresholding result is used for the initialization of a hybrid Markov model which integrates scale-dependent and spatiocontextual information into the labeling process by combining hierarchical with noncausal Markov image modeling. Hierarchical maximum *a posteriori* (HMAP) estimation using the Markov chains in scale, originally developed on quadrees, is adapted to hierarchical irregular graphs. To reduce the computational effort of the iterative optimization process that is related to noncausal Markov models, a Markov random field (MRF) approach is defined, which is applied on a restricted region of the lowest level of the graph, selected according to the HMAP labeling result. The experiments that were performed on a bitemporal TerraSAR-X StripMap data set from South West England during and after a large-scale flooding in 2007 confirm the effectiveness of the proposed change detection method and show an increased classification accuracy of the hybrid MRF model in comparison to the sole application of the HMAP estimation. Additionally, the impact of the graph structure and the chosen model parameters on the labeling result as well as on the performance is discussed.

Index Terms—Automatic thresholding, change detection, flood mapping, generalized Gaussian distribution, hierarchical maximum *a posteriori* (HMAP) marginal estimation, irregular graph, Markov random field (MRF).

I. INTRODUCTION

THE WORLDWIDE increase of flood risk [1] and the timely monitoring capability of the recently launched high-resolution space-based synthetic aperture radar (SAR) sensors (TerraSAR-X, COSMO-SkyMed, Radarsat-2, and ALOS-PALSAR) require accurate and automatic change detection methods for the derivation of flood dynamics. This is particularly the case for rapid mapping purposes [2] where accurate information about the extent of a disaster and its spatiotemporal evolution are necessary on a near real-time basis to support decision makers and humanitarian relief organizations.

Manuscript received January 13, 2010; revised May 13, 2010.

The authors are with the German Remote Sensing Data Center (DFD), German Aerospace Center (DLR), 82234 Wessling, Germany (e-mail: Sandro.Martinis@dlr.de; andre.twele@dlr.de; stefan.voigt@dlr.de).

Color versions of one or more of the figures in this paper are available online at <http://ieeexplore.ieee.org>.

Digital Object Identifier 10.1109/TGRS.2010.2052816

In comparison to optical remote sensing, the SAR data show the clear advantage of imaging capability even in the case of adverse meteorological and nighttime conditions.

Numerous techniques have been developed for the derivation of changes in remote sensing imagery. The most common change detection techniques are postclassification comparison [3] and classification of some feature maps, such as difference images [4], ratio images [5], and results derived from selective principal component analysis [6].

Several unsupervised change detection methods have been established in the last few years, which derive change maps through the application of automatic thresholding algorithms on feature maps by using minimum-error procedures [5], [7] or expectation-maximization algorithms [8], [9] for the estimation of the data mixture models. These methods are proven to be effective in solving the single-threshold approach between classes “change” and “no change” in small subsets of remote sensing data pairs. However, in large data sets, where local gray-level changes may not be distinguished in the image histogram due to small *a priori* probabilities of some classes, these methods may fail. Furthermore, the change detection problem in feature maps extends to a three-class segmentation problem if different types of changes are to be extracted.

An important feature which improves the quality of classification results is the integration of contextual information into the labeling process. Markov image modeling is proven to be a useful tool in considering the contextual information in remote sensing data. Noncausal lattice-based Markov random fields (MRFs) have been extensively used to model stochastic interactions among classes in remote sensing imagery [4], [10]–[12], and they allow a global Bayesian optimization of the classification result [12]. However, the computational effort is considerable since the classification process must be accomplished iteratively for each image element. This is particularly time consuming in pixel-based applications.

A computationally faster alternative to MRFs are hidden Markov chain (HMC) models [12]–[15], which are applied for spatial image regularization problems to 1-D representations of images, like the Hilbert-Peano Scans, in a noniterative manner. The computational improvement of these methods, however, may come at the expense of lower classification accuracy [12].

In contrast to noncausal MRF and HMC models, the hierarchical Markov models [16]–[18] have the capacity to capture the intrinsic hierarchical nature of remote sensing data. The

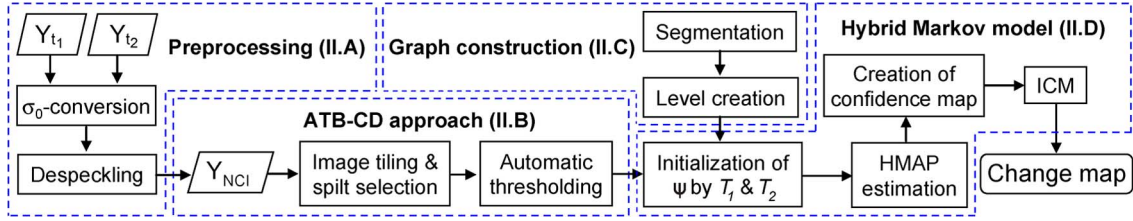


Fig. 1. Block scheme of the proposed method.

image is represented by a hierarchical graph which allows the integration of multiscale information into Markov image models. These models can be solved by fast noniterative inference, e.g., by Markov chains in scale [16], [18].

In most of the cases, hierarchical Markov modeling is conducted on the simple regular graph structure of quadrees [18]–[21], which is represented by four branches at each node. Due to the fact that image segmentation is accomplished without consideration of the image content, block artifacts may occur in the final estimates. Several methods have been proposed to reduce these undesired effects, e.g., *a posteriori* smoothing [22], the integration of tree structures with overlapping data leaves [23], and the introduction of interlevel edges [16].

On a quadtree, the class label of a node solely depends on the labels of its ancestor and its four descendants. In order to improve the classification, the study in [17] and [19] considered a more complex graph, which additionally integrates a regular spatial neighborhood at each level in the modeling process. However, since the modeling incorporates all elements of each level in an iterative way, the computational demand strongly increases.

This paper presents an automatic method for the near real-time extraction of flood-induced change areas in multitemporal TerraSAR-X data using a hybrid context-based model, combining causal with noncausal Markov image modeling on irregular hierarchical graphs (Fig. 1). The specific objectives are the following: 1) to implement a tile-based automatic change detection approach for the initialization of the Markov image model. Therefore, a parametric thresholding algorithm under the generalized Gaussian (GG) assumption is applied to image tiles to solve the three-class change detection problem in large-size SAR data; 2) to establish an automatic method for the creation of an irregular hierarchical graph structure of the SAR data according to user-defined specifications of average object sizes at each level; and 3) to integrate scale-dependent contextual information by hierarchical maximum *a posteriori* (HMAP) estimation using Markov chains in scale as well as spatiocontextual information by a noncausal MRF model in a partial region of the finest level of the tree, defined by the frequency of occurrence of class labeling in the multiscale representation of the image.

II. METHODOLOGY

A. Data Set

Data Set Description: This study was conducted over the Gloucestershire region in South West England, which was affected by severe flooding at the River Severn in summer 2007.

In the city of Tewkesbury, a record flood level of 5.23 m was reached on July 22, 2007. In order to carry out an experimental analysis that is aimed at assessing the performance of the proposed change detection approach for a real test case, a bitemporal data set that consists of two TerraSAR-X StripMap scenes with 3.0-m pixel spacing in the range and azimuth directions is used. The first image was acquired in HH polarization on July 25, 2007, with an incidence angle of $\sim 22.4^\circ$ along a section of about 69 km long of the River Severn. The second image was recorded roughly one year after (July 22, 2008). It exhibits nearly the same geographic coverage, with a river network at normal water level conditions. Due to the fact that the second image has identical acquisition parameters, shadowing and layover conditions in the data are similar.

For validation purposes of the water level in each scene, two aerial orthophotos are used: The first one shows the flood situation at about half a day prior to the TerraSAR-X scene on July 25, 2007, at a spatial resolution of 0.2 m. For the validation of the water level of the postevent data, no contemporary aerial photographs are available. However, due to the fact that, on July 22, 2008, the SAR scene was recorded at normal water level conditions, the aerial photographs on April 30, 2007, could be used as reference due to a very similar extent of the rivers.

Preprocessing: Initially, the SAR amplitude data are radiometrically calibrated to backscattering coefficients σ_0 to minimize the impact of the topography on the radar signal. To simplify data handling in the following processing steps, all σ_0 values are converted to positive values by adding a constant to the σ_0 value of each date. For a reduction of the SAR data inherent speckle effect, a Gamma-MAP filter [24] of matrix size 3×3 is used. Additionally, the filtering step minimizes the statistical overlap between class distributions and, therefore, leads to a better class separability.

A reference map is created for a subarea ($\sim 6.43 \times 10^6$ pixels) of the overlap between the SAR scenes comprising the heavily flooded Tewkesbury region by visual interpretation and manual digitalization of the water areas in both orthophotos. The final flood change mask is created by the intersection of these two water layers.

B. ATB-CD Approach

Problem Formulation: Let us consider two coregistered SAR intensity images Y_{t_1} and Y_{t_2} acquired over the same geographical areas at two times t_1 and t_2 ($t_1 < t_2$), respectively. To derive the flood-induced changes over the time interval $[t_1, t_2]$, the information content of Y_{t_1} and Y_{t_2} is combined into one

image Y with D elements by the calculation of a normalized change index (NCI) for each pixel at position d ($\sigma_0 > 0$)

$$NCI = ((\sigma_0^{t_2} - \sigma_0^{t_1}) / (\sigma_0^{t_2} + \sigma_0^{t_1})) + 1. \quad (1)$$

The generated image Y with $y_d = NCI$ has a float data range from $[0, \dots, 2]$, with values that are equal to one showing the unchanged areas. A high NCI is an indicator for pixels with an increase in backscattering at t_2 , which, in this case, is related to the changes caused by a decreasing flood level. For a more efficient data handling, the float values of Y are transformed to 8-bit integers with a possible gray-level range G of 256, i.e., $y_d = g, g \in \{0, 1, \dots, G - 1\}$.

Since the histogram of Y can be considered as a mixture of three distributions of classes i [“negative change” ($C-$), “unchanged” (U), and “positive change” ($C+$)], the classification task aims at identifying threshold τ_1 between $C-/U$ and τ_2 and between $U/C+$. This means that y_d could be labeled as $C-$ if $y_d \leq \tau_1$, as U if $\tau_1 < y_d < \tau_2$, and as $C+$ if $y_d \geq \tau_2$.

To automatically derive τ_1 as well as τ_2 and, therefore, to initialize the Markov model in an unsupervised way, an automatic tile-based change detection (ATB-CD) approach is used. This method extends the work of [25], which used an automatic thresholding approach for the extraction of flood areas in high-resolution mono-temporal SAR data in the context of operational rapid mapping activities. In this approach, the SAR data are split into a set of square subimages of a user-defined size, and a fixed number of tiles are automatically selected according to their probability to comprise adequate portions of the classes “flood” and “no flood.” In order to derive the best class separation in the (sub)histograms, the Kittler and Illingworth (KI) thresholding algorithm [26] has been used, which models the class-conditional probability density function (pdf) as a mixture of two clusters of two 1-D normal distributions of the semantic classes “flood” and “no flood” and which derives the threshold at the gray-level position where the minimum classification error occurs.

Since change detection is a three-class segmentation problem, if one wants to extract different types of changes, this binary classification method has to be extended to a double threshold selection task. In large NCI images, the *a priori* class probabilities are usually very different. Therefore, in particular, the change classes $C-$ and $C+$ might not be detectable in the histogram of the entire data set. This partly makes it impossible for any thresholding algorithm to compute adequate threshold values. The usage of the ATB-CD approach offers the advantage that the threshold positions are computed from several tiles of the whole NCI image where local gray-level changes, even of classes of low areal representation, may be distinguished in the image (sub)histograms.

NCI Splitting and Tile Selection: Initially, the NCI data Y are split into N square nonoverlapping subimages Y_n of size z^2 . In order to prevent unimodality of the selected (sub)histograms, it has to be ensured that a distinct number of elements of both classes $C-$ and U as well as U and $C+$, respectively, are represented within the tiles. Appropriate tiles for the derivation of τ_1 and τ_2 are selected, combining the global statistics of

Y and the local statistics of Y_n by applying the following formulations:

$$Y_{n'_{C-/U}} = \{Y_n | CV_{Y_n} \geq 0.3 \wedge R_{Y_n} \leq 0.9, \quad n = 1, \dots, N\} \quad (2)$$

$$Y_{n'_{U/C+}} = \{Y_n | CV_{Y_n} \geq 0.3 \wedge R_{Y_n} \geq 1.1, \quad n = 1, \dots, N\}. \quad (3)$$

CV_{Y_n} is the coefficient of variation (ratio of the square root of the local variance v_{Y_n} of the gray values of Y_n to the local mean μ_{Y_n}), and R_{Y_n} is the ratio between μ_{Y_n} to the global intensity mean μ_Y of Y . CV_{Y_n} represents the degree of gray-level variation within Y_n . Therefore, it is an appropriate feature to separate subimages with nearly unimodal histograms from tiles that are represented by more than one class. This means that tiles are selected, which contain a significant amount of pixels of the classes $C-$ and U as well as U and $C+$, respectively. Using the additional feature R_{Y_n} , the selected subimages can be divided into tiles which seem to be adequate for the derivation of either τ_1 or τ_2 .

Out of the two sets $N'_{C-/U}$ and $N'_{U/C+}$ of subimages $Y_{n'(C-/U)}$ and $Y_{n'(U/C+)}$ which are located in the range given by (2) and (3), respectively, a limited number of tiles are finally used for threshold computation. This selection is accomplished by choosing the quantity $N''_{C-/U}$ and $N''_{U/C+}$ of tiles $Y_{n''(C-/U)}$ and $Y_{n''(U/C+)}$, with the lowest Euclidean distances to the cluster centers of the 2-D feature spaces determined by CV_{Y_n} and R_{Y_n} . The values of CV_{Y_n} and R_{Y_n} in (2) and (3) are determined empirically from the investigation of several NCI data sets. For visualization of the splitting and tile selection process, the reader is referred to [25].

If $N'_{C-/U}$ and/or $N'_{U/C+}$ is zero, the interval of the selection criterion is expanded by iteratively decreasing CV_{Y_n} by 0.01 to a minimum value of 0.25. However, in some cases, in every Y_n of size z^2 , the *a priori* probability of a class may be very small. Therefore, if still no tiles are selected according to the enlarged criterion, the initially chosen tile size z is halved, which increases the number of N by a factor of four. If after this step $N'_{C-/U}$ and/or $N'_{U/C+}$ remains zero, it is assumed that the corresponding class $C-$ and/or $C+$ is not represented in Y .

Automatic Threshold Selection Procedure: The KI thresholding algorithm automatically computes the threshold value between the object and background classes of a gray-scale image according to a parametric estimation of the statistical model of the two class pdfs under the Gaussian distribution assumption.

In order to improve the threshold selection process, the study in [7] reformulated this method based on the GG model. This model is well adapted to approximate a large range of symmetric, leptokurtic (ranging from impulsive to Gaussian density), and platykurtic distributions (ranging from Gaussian to uniform density). Their parameterization requires the estimation of only one additional parameter in comparison to the Gaussian model, which is the shape parameter $\beta_i > 0$, which determines the rate of the exponential decay of the pdfs ($\beta_i = 1$ for Laplacian,

$\beta_i = 2$ for Gaussian, and $\beta_i > 8$ for nearly uniform density functions).

In the following, it is assumed that the histograms $h(g)$ of $Y_{n''(C-/U)}$ and $Y_{n''(U/C+)}$ can be parameterized by a pdf $p(g)$, which is a mixture of two GG distributions $p(g|i)$ with parameter mean μ_i , standard deviation σ_i , *a priori* probability P_i , and shape parameter β_i , where

$$i = \begin{cases} (C-, U), & \text{if } Y_{n''} \in Y_{n''_{C-/U}} \\ (U, C+), & \text{if } Y_{n''} \in Y_{n''_{U/C+}} \end{cases}$$

$$\text{so that } p(g) = \sum_{i=1}^2 P_i p(g|i). \quad (4)$$

The expression of the GG distribution for modeling the two class-conditional pdfs of $Y_{n''(C-/U)}$ and $Y_{n''(U/C+)}$ is given by

$$p(g|i) = \frac{b_i \beta_i}{2\Gamma(\beta_i^{-1})} e^{-(b_i |g - \mu_i|)^{\beta_i}} \quad \text{with } b_i = \frac{1}{\sigma_i} \sqrt{\frac{\Gamma(3/\beta_i)}{\Gamma(1/\beta_i)}} \quad (5)$$

where $\Gamma(\cdot)$ is the gamma function. The required parameters have to be estimated at some arbitrary decision threshold T which separates the two clusters with the following properties:

$$\mu_i(T) = \frac{1}{P_i(T)} \sum_{g=a}^b gh(g) \quad \text{with } P_i(T) = \sum_{g=a}^b h(g) \quad (6)$$

$$\sigma_i(T) = \frac{1}{P_i(T)} \sum_{g=a}^b (g - \mu_i(T))^2 h(g) \quad (7)$$

$$\text{where } a = \begin{cases} 1, & \text{if } i = C- \wedge Y_{n''} \in Y_{n''_{C-/U}} \\ & \vee i = U \wedge Y_{n''} \in Y_{n''_{U/C+}} \\ T+1, & \text{if } i = U \wedge Y_{n''} \in Y_{n''_{C-/U}} \\ & \vee i = C+ \wedge Y_{n''} \in Y_{n''_{U/C+}} \end{cases} \quad (8)$$

$$b = \begin{cases} T, & \text{if } i = C- \wedge Y_{n''} \in Y_{n''_{C-/U}} \\ & \vee i = U \wedge Y_{n''} \in Y_{n''_{U/C+}} \\ G, & \text{if } i = U \wedge Y_{n''} \in Y_{n''_{C-/U}} \\ & \vee i = C+ \wedge Y_{n''} \in Y_{n''_{U/C+}}. \end{cases} \quad (9)$$

The shape parameter is derived by the estimation procedure described in [27]. This technique allows the identification of an estimated value of β_i which best parameterizes the so called GG ratio function $r(\beta_i)$, computed for 450 different values of β_i in the range of $[0.5, \dots, 5.0]$ with a step size of 0.01.

The computation of the final decision thresholds τ_1 and τ_2 is based on the optimization of a criterion function averaging a cost function $c(g, T)$ over $h(g)$

$$J(T) = \sum_{g=0}^{G-1} h(g)c(g, T). \quad (10)$$

According to the number of gray levels of a tile, the cost at G threshold positions can be evaluated successively to label the

pixels by utilizing the generated class statistics by computing the fitting criterion $J(T)$ under the GG assumption [7]

$$J(T) = \sum_{g=0}^T h(g) [b_{C-}(T) |g - \mu_{C-}(T)|]^{\beta_{C-}(T)} + \sum_{g=T+1}^{G-1} h(g) [b_U(T) |g - \mu_U(T)|]^{\beta_U(T)} - \sum_{g=0}^T h(g) \ln P_U(T) - \sum_{g=T+1}^{G-1} h(g) \ln P_{C-}(T) - \left[P_U(T) \ln \left(\frac{b_U \beta_U}{2\Gamma(1/\beta_U)} \right) (T) + P_{C-}(T) \ln \left(\frac{b_{C-} \beta_{C-}}{2\Gamma(1/\beta_{C-})} \right) (T) \right]. \quad (11)$$

Equation (11) has been adapted for tiles $Y_{n''(C-/U)}$. For tiles $Y_{n''(U/C+)}$, $C-$ has to be replaced with U , and U has to be replaced with $C+$. The gray-level position which minimizes $J(T)$ can be regarded as the optimal decision threshold due to the fact that the lowest classification error occurs according to the Bayes classification rule (i.e., the number of mis-segmented pixels is smallest)

$$\tau_{1/2} = \arg \min_T J(T). \quad (12)$$

For finally obtaining two global thresholds for the classification of Y , the locally derived threshold values of $Y_{n''(C-/U)}$ as well as $Y_{n''(U/C+)}$ are combined by their arithmetic mean. Another possibility of threshold computation is the analysis of one histogram that is combined with the local histograms of the tiles $Y_{n''(C-/U)}$ as well as $Y_{n''(U/C+)}$ [25].

C. Automatic Graph Construction

Image Segmentation: Segmentation is the basic step in low-level processing of images [28], in which an image is subdivided into disjoint regions, which are uniform with respect to some homogeneity attributes such as spectral or textural characteristics [29]. During the recent years, segmentation-based image analysis has constantly gained importance in Earth observation. This can particularly be attributed to the strongly increased spatial resolution of remote sensing data, which demand image analysis techniques that are specifically adapted to the increased intraclass and decreased interclass variability of images [30]. In particular, for the data of the recently launched high-resolution SAR sensors, the use of the per-parcel methods appears promising. These data are, in comparison to medium-resolution SAR data, characterized by higher variances in backscattering properties of different land-cover classes due to the reduced mixed pixel phenomenon and the salt-and-pepper structures that result from the speckle. This means that semantic image information is less represented in a single pixel but in homogeneous image objects and their mutual relations [31]. The decomposition of the images can be accomplished by several segmentation techniques described in literature [29].

In the presented approach, the decomposition of Y in object primitives is performed using the fractal net evolution concept of the eCognition Developer software [31], [32]. In an iterative way, a bottom-up region-merging technique starting from pixel elements is employed to create image objects of maximum allowable heterogeneity according to user-defined spectral and geometrical constraints. These homogeneity attributes are expressed by the so-called scale parameter H , which combines spectral ($h_{\text{color}} \in [0, \dots, 1]$) and shape homogeneity ($h_{\text{shape}} \in [0, \dots, 1]$), with $h_{\text{shape}} = 1 - h_{\text{color}}$ and h_{shape} , being composed of the smoothness h_{smooth} and compactness h_{compact} of the object boundaries ($h_{\text{smooth}} = 1 - h_{\text{compact}}$). The fusion of the adjacent objects follows the local mutual best fitting algorithm, leading to the lowest increase of object heterogeneity within the merging process. The greater the value of H is, the greater is the decrease of the sensitivity for the object fusion, i.e., the obtained object size increases.

The created segments exhibit a strong correlation with real-world objects of the Earth's surface. However, due to the fact that the semantic information is scale dependent, a hierarchical network of image objects is simultaneously constructed, which represents the image content at different spatial scales. By exploiting the relationship between the networked objects, the local contextual information can be integrated into the multi-scale image analysis.

Automatic Level Creation: In the proposed approach, the spatial context of each pixel in image Y is modeled according to a complete hierarchical multilevel representation of the scene, where objects at the same level S^l ($l = 1, \dots, L$) are related to each neighboring object and where every object at an arbitrary level is hierarchically linked to those represented at lower and/or higher levels. Tree-based hierarchic constraints are used, whereby each object at S^{l-1} ($l < L$) has only one parent node at level S^l , i.e., it cannot be included in more than one adaptive neighborhood at the coarser superlevel. The object size and, therefore, the number of objects O^l at each level are adjusted by the scale parameter H^l , which regulates the homogeneity property at each level. The greater the value of H^l is, the greater is the dimension of the objects obtained at S^l .

In the quadtree decomposition of an image [18], [20], O^l of each level and, therefore, the percentage difference E^l of O^l ($l > 1$) to O^1 are known before the image decomposition is accomplished. The total number of segments is approximately given by $4/3 * O^1$ [16]. However, in the context of irregular hierarchical image segmentation, these parameters are not known in advance, and they must primarily be adjusted in a trial-and-error fashion.

In this section, an approach is presented which automatically generates a multilevel segmentation with the following characteristics: 1) the finest level S^1 is decomposed by an initially intended mean relative object number \tilde{O}_p^1 , defined in objects per pixel, and 2) the coarser levels S^l ($l \neq 1$) offer an initially defined value of \tilde{E}^l . On the one hand, this is important in order to prevent over- and undersegmentation of S^1 . On the other hand, the transferability of algorithms is ensured by a fixed difference in the mean object size between levels. The choice of \tilde{O}_p^1 depends on the minimum mapping unit of the classification process and, therefore, on the information detail

that is to be detected from the classes $C-$, U , and $C+$. The lower \tilde{O}_p^1 is, the higher is the probability that the fine detail is lost. Therefore, \tilde{O}_p^1 should be approximately equal to the size of the smallest objects to be detected. An increasing value of \tilde{O}_p^1 causes a higher processing demand due to the increasing number of nodes of the graph. Additionally, more false alarms may occur due to the reduced smoothing effect that is related to the oversegmented data.

For the creation of level S^1 with a user-intended value of \tilde{O}_p^1 , we present an approach which uses a presegmentation of a limited area of Y . Therefore, Y is decomposed in N square tiles of size z^2 . Out of N , three tiles Y_n of size A_{init}^k are assigned to three classes w_k , which show the minimum ($k = \min$) and maximum ($k = \max$) coefficient of variation (CV) as well the lowest difference to the mean CV ($k = \text{mean}$) of all Y_n . The three tiles are segmented with an arbitrary scale parameter H_{init}^1 . Subsequently, the resulting number of objects O_k^1 of each class is used to estimate \hat{O}_p^1 , which would result from the segmentation of the entire image Y by H_{init}^1 . For this task, the value of O_k^1 is weighted in dependence of an extrapolated spatial representation A_{ext}^k of the classes w_k in relation to the size A_Y of Y . The tiles N are then labeled by the following formulations for $n = 1, \dots, N$:

$$w_{\min} = \{Y_n | CV_{Y_n} \leq CV_{\min} + \sigma_{CV}\} \quad (13)$$

$$w_{\text{mean}} = \{Y_n | CV_{\text{mean}} - 0.5\sigma_{CV} \geq CV_{Y_n} \leq CV_{\text{mean}} + 0.5\sigma_{CV}\} \quad (14)$$

$$w_{\max} = \{Y_n | CV_{Y_n} \geq CV_{\max} - \sigma_{CV}\}. \quad (15)$$

The value of \hat{O}_p^1 of the extrapolated class probabilities is calculated by

$$\hat{O}_p^1 = A_Y \left(\frac{\sum_{k=1}^3 \frac{O_i^1 A_{\text{ext}}^k}{A_{\text{init}}^k}}{\sum_{k=1}^3 A_{\text{ext}}^k} \right) D^{-1}. \quad (16)$$

In the case where \hat{O}_p^1 differs from \tilde{O}_p^1 , the relation between O_p^1 and H^1 is used to approximate the user-intended value of \tilde{O}_p^1 by adapting H^1 to the prevailing image content of Y . However, the image content is not known in advance, and a varying number of objects at a given value of H^1 are generated in dependence of the class mixtures.

To model the image content, the relation between O_p and H in the range of [1–115] is calculated (Fig. 2) for six tiles ($z = 500$) of Y containing the following class *a priori* probabilities: a) 25%; b) 50%; c) 75%; and d) > 90% of the change caused by flooding (the remaining percentage is the unchanged natural area); e) 100% unchanged natural area; and f) 100% unchanged urban area.

The lowest value of O_p in dependence of H [1–115] is created by the tile covering 100% of the natural areas e) due to the large size and spectral homogeneity of these regions. In contrast, small-scale features within urban areas f) induce the highest values of O_p in dependence of H . For clarity reasons, just the trends of e) and f) are shown in Fig. 2. Trend lines a)–d) are situated between e) and f). The trends are well modeled ($R^2 > 0.998$) by second-order polynomial equations of the

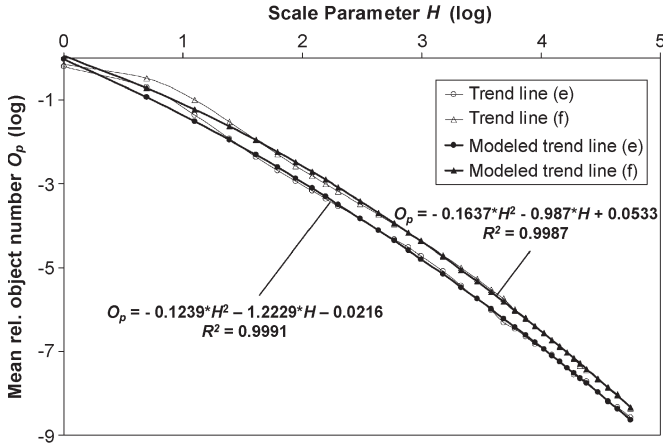


Fig. 2. Dependence of the mean relative object number O_p from the scale parameter H ($h_{\text{color}} = 0.9$ and $h_{\text{compact}} = 0.5$) for two subimages of Y consisting of natural and urban areas, respectively.

form $O_p = a * H^2 + b * H + c$. For each equation of the trend lines a)–f), the respective value of O_p is computed by H_{init}^1 , and the function which is most representative for the scene, which generates the lowest difference between O_p and \hat{O}_p^1 , is used for the subsequent approximation of \tilde{O}_p^1 . By integrating \tilde{O}_p^1 in the respective equation of the chosen function, \hat{H}^1 is calculated, which leads to the decomposition of the lowest level S^1 of Y with $\hat{O}_p(\hat{H})^1 \sim \tilde{O}_p^1$

$$\hat{H}^l = e^{\left(\frac{-b - \sqrt{b^2 - 4a(c - \ln(O_p^l))}}{2a} \right)} \quad (17)$$

Finally, levels S^l ($l > 1$) are decomposed by \hat{H}^l , approximating a user-defined percent difference \tilde{E}^l of O_p^l ($l \neq 1$) to $\hat{O}_p(\hat{H})^l$. This is accomplished by integrating \tilde{O}_p^l ($l > 1$) into (17).

D. Markov Image Modeling

Context is a rich source of information for the analysis of remote sensing images. In particular, for the new generation of high-resolution SAR data, objects on the ground are much greater than the pixel size. Thus, the likelihood is very high that the adjacent pixels, although characterized by different scattering properties, belong to the same land cover unit and form a homogeneous region. Markov image modeling is a commonly used approach for the integration of contextual information into the classification scheme of remotely sensed images.

In the following, two different Markov image models are described in the image object domain, i.e., a causal Markov model which uses HMAP estimation on a multiscale tree and a noncausal MRF model on an irregular planar graph associated to an image partition. We furthermore introduce a hybrid method that combines the computational speed of the HMAP modeling approach with the fine spatial modeling of noncausal MRFs on a restricted number of elements. This hybrid Markov model can be combined with every segmentation algorithm, which is able to perform a multilevel representation of an image.

Causal Markov Model: The multilevel decomposition of a SAR scene Y can be represented as a connected graph $\Psi_L = (S, W)$ with L levels that are composed of a set of nodes S and W edges, where each node s , apart from the root r , has a unique parent node s^- (Fig. 3). The superscript “ $-$ ” designates the decrease of the spatial resolution from a child node to its parent node. A descendant node originating from s is denoted as node t . The set of nodes can be partitioned into levels of different scales $S = S^1 \cup S^2 \cup \dots \cup S^L$ according to the path length from each node to the root. The level decomposed by the lowest scale parameter is S^1 , and the coarsest level consists of only one node $S^L = \{r, l = L\}$. In the following, hierarchical Markov image modeling is applied on an irregular hierarchical graph (Fig. 3), leading to a unique statistical inference problem instead of a sequence of multiscale problems that are only loosely related [18].

In this hierarchical classification problem, one attempts to estimate the hidden variable set x through a set of observed variables y . Variables x and y are occurrences of the random vectors X and Y , which are attached to the nodes s of Ψ_L .

In the following, a labeling process is considered, which assigns a label x_s to each node s of levels S^l of Ψ_L , where x_s takes its values in the discrete set x of classes i ($i \in x = \{C-, U, C+\}$):

$$x = \{x^l\}_{l=1}^L \quad \text{with } x^l = \{x_s, s \in S^l\}. \quad (18)$$

The classification is accomplished by HMAP estimation. The following Bayesian estimator is used:

$$\hat{x} = \arg \max_{x \in x^S} P(x|y) = \arg \max_{x \in x^S} P(x, y) \quad (19)$$

where x^S is the configuration set of the vectors x of all nodes S .

A number of statistical assumptions about the random vectors (X, Y) are defined in the following [18].

The labeling process X is supposed to be Markovian in scale (i.e., X is a first-order top-down Markov chain)

$$P(x^l | x^\lambda, \lambda > l) = P(x^l | x^{l+1}) \quad \forall l \in \{1, \dots, L\}. \quad (20)$$

To simplify the notation, the discrete probability $P(X = x)$ is denoted as $P(x)$ throughout this paper. The interscale transition probabilities can be factorized by the following criteria (21)–(23):

$$P(x^l | x^{l+1}) = \prod_{s \in S^l} P(x_s | x_{s^-}). \quad (21)$$

This means that, for each S^l , the conditioning in X^{l-1} reduces to a dependence from its parent node only.

Assuming conditional independence, the likelihood of the observations Y conditionally to X is defined by the following model:

$$P(y|x) = \prod_{s \in S^l} P(y_s | x_s). \quad (22)$$

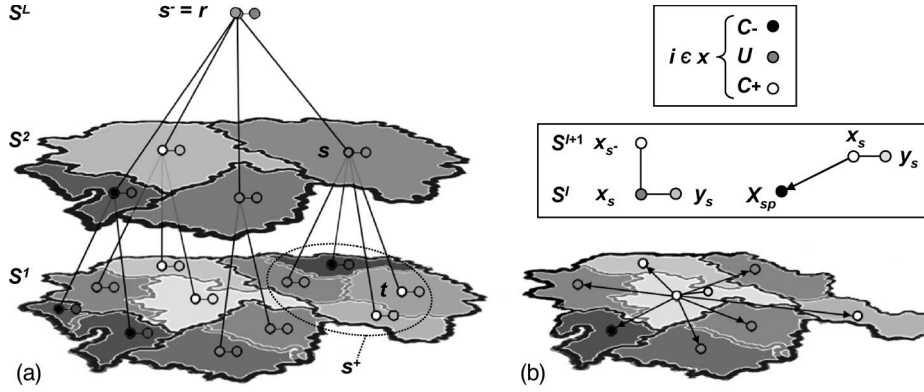


Fig. 3. (a) Three-level independence graph Ψ_3 corresponding to an irregular tree structure. (b) Irregular planar graph with a second-order clique set in neighborhood system V_{sp} . The left circles represent the labeling according to classes C^- , U , and C^+ . The right circles represent the observations at each node.

TABLE I
TWO-PASS MAP ESTIMATION ON IRREGULAR HIERARCHICAL GRAPHS

Bottom-up sweep: Functions $P_s(x_{s^-})$ (most probable label \hat{x}_{s^-} of a parent node s^-) and $x_s^*(x_{s^-})$ (MAP estimate of child node s according to MAP component \hat{x}_{s^-}) are computed and stored in look-up tables for all possible values of x_{s^-} .

Initialization ($s \in S^1$):

$$P_s(x_{s^-}) = \max_{x_s} P(y_s | x_s) P(x_s | x_{s^-}) \varphi$$

$$x_s^*(x_{s^-}) = \arg \max_{x_s} P(y_s | x_s) P(x_s | x_{s^-}) \varphi$$

Recursion ($s \in S^2 \dots S^L$):

$$P_s(x_{s^-}) = \max_{x_s} P(y_s | x_s) P(x_s | x_{s^-}) \prod_{t \in S^+} P_t(x_s) \varphi$$

$$x_s^*(x_{s^-}) = \arg \max_{x_s} P(y_s | x_s) P(x_s | x_{s^-}) \prod_{t \in S^+} P_t(x_s) \varphi$$

Top-down sweep: Components of the MAP estimate are recovered from the root to the leaves

Initialization (root r):

$$\hat{x}_r = \arg \max_{x_r} P(y_r | x_r) P(x_r) \prod_{t \in r^+} P_t(x_r)$$

Recursion ($s \in S^{L-1} \dots S^1$):

$$\hat{x}_s = x_s^*(x_{s^-})$$

According to these statistical assumptions, the joint distribution $P(x, y)$ can be expressed by

$$P(x, y) = P(x_r) \prod_{s \neq r} P(x_s | x_{s^-}) \prod_{s \in S} P(y_s | x_s) \quad (23)$$

where $P(x_r)$ is the root prior probability and $\{P(y_s | x_s)\}_{s \in S}$ is the data conditional likelihoods.

One of the advantages of these models lies in the possibility to compute the exact MAP estimate of X , given $Y = y$ at each node of the tree within two passes. This extension of the Viterbi algorithm [18], which is a standard technique for the computation of the MAP estimate of HMCs [33], is summarized in Table I.

To account for the problem of underflow in the Viterbi algorithm, the whole estimation procedure is implemented by computing the logarithm of the probabilities. In the bottom-up sweep, we integrated a weighting factor φ , which takes into account the proportion of the spatial extent A of child node

s to its ancestor s^- in dependence of the number of child nodes t

$$\varphi = (1 - (A_s/A_{s^-})) / (\text{card}(t) - 1). \quad (24)$$

Equation (24) has been adapted to weight negative values of the probabilities, which result from the logarithmic expression of the probabilities in the HMAP estimation. In contrast to the MAP estimation on the quadtree, where all child objects have the same size of $A_{s^-}/4$, φ has to be integrated in the computation of the inference on irregular graphs, where an ancestor is represented by a varying number of child objects at lower levels.

For the conditional likelihoods $P(y_s | x_s)$, a Gaussian model was chosen, defined by the parameter vector $\theta_i = (\mu_i, \sigma_i)$, where μ_i is the mean and σ_i is the standard deviation of class i . Vector θ_i may vary depending on the spatial resolution so that the classes are defined by θ_i^l . The conditional likelihoods are defined by

$$\forall s \in S^l, \quad P(Y_s = y_s | X_s = i) = \frac{1}{2\pi\sigma_i} e^{-(y_s - \mu_i)^2 / 2\pi(\sigma_i)^2}. \quad (25)$$

The scale-dependent parameters for each class are defined by the unsupervised change detection method described in Section II-B. For the definition of the prior probability, the Potts-like model is used [16], which favors identical labeling of s and s^-

$$\forall s \in S^l, \quad P(X_s = j | X_{s^-} = i) = \begin{cases} \phi, & \text{if } i = j \\ \frac{1-\phi}{M-1}, & \text{if } i \neq j \end{cases} \quad (26)$$

with the number of classes M , the root prior $P(r) = 1/M$, and the parent prior Φ [$1 \leq \Phi < 1/M$]. A higher value of Φ increases the smoothing effect of the classification result.

The labeling of S^1 is used as the final classification result of the HMAP approach, as during the two pass steps, most contextual information is integrated into the labeling of the lowest segmentation level. The HMAP approach is a fast and effective method for postclassification smoothing on irregular trees. To further improve the results, spatial context is integrated into the labeling process using noncausal MRFs.

Noncausal MRF Model: The principal idea of noncausal MRFs is the modeling of contextual correlations among image elements at the same level according to criteria such as MAP estimation (19). To make MRFs computationally tractable, the conditional prior probability of individual image elements has to be modeled, given their neighboring objects. According to the Hammersley–Clifford theorem [34], [35], the prior $P(x)$ can be expressed by a Gibbs distribution. Using this MRFs–Gibbs equivalence, the global contextual relationship of Y can be modeled by MRFs of local spatial neighborhoods

$$P(x_s|X_{sp}) = Z^{-1} \exp^{-U_{sp}(x_s, X_{sp})} \quad (27)$$

where x_s denotes the class of node s , X_{sp} is a subset of the labeling of the image in a predefined spatial neighborhood system V_{sp} , and Z is a normalizing constant. This simplification is a reasonable approach because the interactions between object labels decrease rapidly with an increasing object distance. Usually, in image analysis, MRFs are applied to regular lattices with first- or second-order neighborhood systems, where each pixel has four or eight neighbors. Since we are dealing with irregular planar graphs associated to an image partition, the number of image elements in V_{sp} varies. The spatial energy function U_{sp} is characterized as

$$U_{sp}(x_s, X_{sp}) = - \sum_{q \in V_{sp}} \gamma \delta(x_s, x_q). \quad (28)$$

Here, δ is the Kronecker delta function, which is, according to a second-order clique system ($s-q$), equal to one if $x_s = x_q$ and zero, otherwise. The parameter γ controls the influence of the spatiocontextual information of the change detection process, i.e., the greater this term is, the more likely that two adjacent image objects will have the same label. The class-conditional distribution under Gaussian assumptions leads to the following data attach term:

$$U_{\text{data}}(Y_s = y_s | X_s = i) = 0.5 \ln |2\pi\sigma_i^2| + 0.5(y_s - \mu_i)^2 (\sigma_i^2)^{-1}. \quad (29)$$

Together with the regularization term U_{sp} and the data term U_{data} , the MAP estimate can be transformed to the following energy minimization problem:

$$\hat{x}_s = \arg \min_{x_s} \{U_{\text{data}}(Y_s = y_s | X_s = i) + U_{sp}(x_s, X_{sp})\}. \quad (30)$$

This energy function can be solved by iterated conditional modes (ICM) [36], which represents a computationally feasible alternative to simulated annealing [37], converging to a local, but usually sufficient, minimum of the energy function. In this proposed method, the ICM algorithm can be computed as follows.

- 1) Estimate class parameter vectors θ_i^l of the initial tile-based thresholding result.
- 2) For all elements $s \in S^1$, update X by using the HMAP approach.

- 3) For all $s \in S^1$, perform the local minimization by using (30).
- 4) Repeat the preceding step until convergence is reached.

The application of the ICM algorithm to irregular planar graphs compared to pixel-based applications has the advantage that the model is applied to a strongly decreased number of image elements. This is related to a dramatic reduction of computational complexity. However, since the computing time of ICM may still be considerable, particularly if the segmentation of S^1 is accomplished by a small homogeneity parameter, we introduce a hybrid Markov model. According to this model, the ICM algorithm is applied only to a restricted number of image objects, defined by the hierarchical representation of the HMAP labeling result.

Hybrid Markov Model: In the following, a confidence map is created at S^1 by combining the HMAP labeling result from the different tree levels. The objects of S^1 are assigned to different categories according to their frequency $f(x_s)$ of class representation in the coarser super objects of S^l ($l \neq 1, L$):

$$f(x_s) = \sum_{s^- \in (S^2, \dots, S^{L-2})} \kappa, \quad \kappa = \begin{cases} 1, & \text{if } x_{s \in S^1} = x_{s^- \in (S^2, \dots, S^{L-2})} \\ 0, & \text{if } x_{s \in S^1} \neq x_{s^- \in (S^2, \dots, S^{L-2})}. \end{cases} \quad (31)$$

If $f(x_s) = L - 2$ (excluding S^1 and S^L), an object at S^1 is represented by the same class label at all super objects. Therefore, this object shows a high degree of confidence to be labeled to the correct class, and no optimization process by the ICM algorithm is necessary for this object. However, if $f(x_s) < L - 2$ at least at one level S^l ($l \neq 1, L$), the labeling of a super object differs from the labeling of an object at S^1 . Accordingly, the class assignment of all elements $s \in S^1$ with $f(x_s) < L - 2$, is checked by the ICM algorithm in the first iteration. This restricted number of elements $O_{\text{sub-1}}^1$ of the subarea $S_{\text{sub-1}}^1$ can be reduced to $O_{\text{sub-2}}^1$ after the first iteration by the restriction of the ICM algorithms to objects $s \in S^1$ with $f(x_s) < L - 2$, which have a common border to other elements of $s \in S^1$ with $f(x_s) < L - 2$.

For the ICM algorithm, $f(x_s)$ is used for the definition of an adaptive smoothness parameter γ_{adapt} for each object $s \in S_{\text{sub-1}}^1$, with values in a user-defined range $[\gamma_{\text{min}}, \gamma_{\text{max}}]$, according to the following criterion:

$$\gamma_{\text{adapt}} = \gamma_{\text{min}} + (\gamma_{\text{max}} - \gamma_{\text{min}}) / f(x_s). \quad (32)$$

Thus, an image element at S^1 , whose class label is less represented by the same labeling at its ancestors, is characterized by a higher probability that the classification result of the HMAP approach is incorrect. Therefore, a higher value of γ_{adapt} is assigned to this element, which causes an increased influence of the neighboring objects during the ICM approach.

III. EXPERIMENTAL RESULTS

In this section, the effectiveness of the proposed change detection approach is evaluated using an NCI image of the

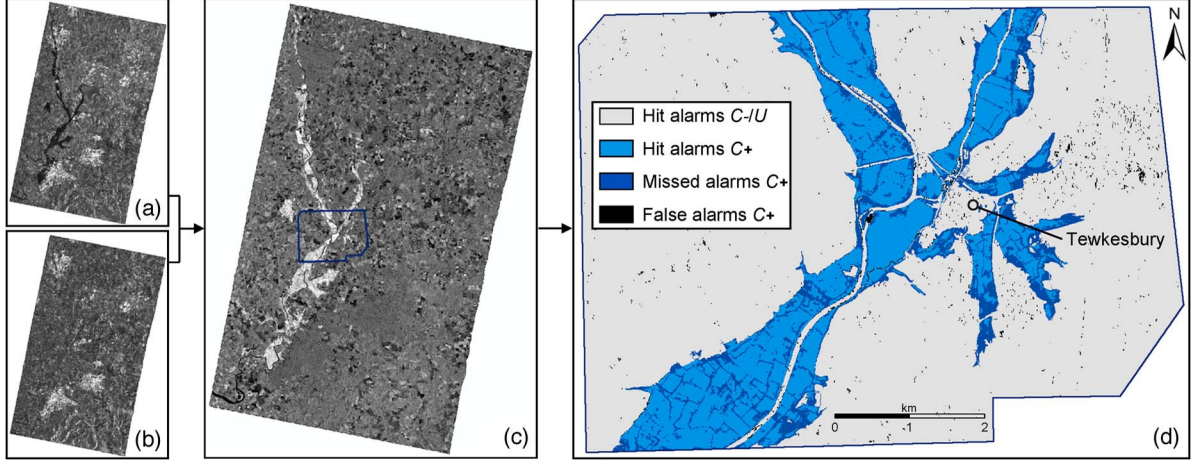


Fig. 4. TerraSAR-X data of the River Severn on (a) July 25, 2007, and (b) July 22, 2008. (c) NCI image. (d) Classification result of Y_{sub} derived by the hybrid Markov model for Ψ_8 , with γ_{1-5} and $H = 24$.

TABLE II
GLOBAL THRESHOLDS CALCULATED BY THE ARITHMETIC MEAN OF
LOCALLY DERIVED THRESHOLDS OF TILES $Y_{n''(C-/U)}$ AND $Y_{n''(U/C+)}$

Class-mixture	Local threshold					Global threshold Mean
	$Y_{1''}$	$Y_{2''}$	$Y_{3''}$	$Y_{4''}$	$Y_{5''}$	
$C-/U$	103	101	105	105	101	104.4
$U/C+$	163	164	171	172	168	167.0

Gloucestershire region (Fig. 4): First, the ATB-CD method is applied on Y for the unsupervised initialization of the Markov image models. In the next step, the structure of a hierarchical irregular graph is created automatically, and its properties of fitting to user-intended scaling parameters are evaluated. Finally, the efficiency of the hybrid Markov image model is assessed. Since the reference water mask only covers a small part of Y , a subarea Y_{sub} ($\sim 6.43 \times 10^6$ pixels) of the Tewkesbury region is chosen for the evaluation of the method.

A. Tile-Based Automatic Thresholding Approach

The ATB-CD approach is used to derive global thresholds for the initialization of the Markov image models. According to a tile size of $z = 500$, the entire image Y , with 3.5×10^8 elements, is decomposed into $N = 1140$ square tiles. Using the criterion defined in (2) and (3), $N'_{C-/U} = 37$ and $N'_{U/C+} = 32$ tiles are selected, which are suitable for the derivation of the thresholds τ_1 and τ_2 . To restrict the computational effort, $N''_{C-/U} = 5$ and $N''_{U/C+} = 5$ tiles are finally chosen for the computation of the local threshold values by applying the GG-KI algorithm. Reasonable global thresholds $\tau_{C-/U} = 104.4$ and $\tau_{U/C+} = 167.0$ are calculated by the arithmetic mean of the locally derived thresholds (Table II). Since these local thresholds are characterized by a low gray-level range of $\sigma_1 = 2.0$ and $\sigma_2 = 4.0$, the proposed method seems to be useful in separating the classes $C-/U$ and $U/C+$. This thresholding approach has the advantage that classes with a small *a priori* probability are also detected in the histogram of Y . Additionally, the computational speed of this methodology is very high since the GG-KI algorithm is only applied on a small number of tiles.

B. Automatic Creation of the Graph Structure

Before the HMAP approach is accomplished, the hierarchical irregular graph structure of the chosen subarea Y_{sub} is generated. In the following, the properties of a graph with $L = 8$ (Ψ_8), created according to user-intended parameters \hat{O}_p^1 and \hat{E}^l , are evaluated.

To approximate a decomposition of S^1 with a mean relative object number \hat{O}_p^1 of 0.015, the following steps are accomplished: First, three square tiles ($z = 500$) of Y_{sub} , labeled to different classes w_k according to (13)–(15), are decomposed by an arbitrary scale parameter $H_{\text{init}}^1 = 15$. The next step encompasses the estimation of \hat{O}_p^1 through the extrapolation of the resulting object number O_k^1 of each class by their spatial representation in Y_{sub} . According to (16), $\hat{O}_p^1 = 0.0129$. This is an underestimation of \hat{O}_p^1 . In order to approximate \hat{O}_p^1 , the scale parameter has to be adapted. According to that, for each of the equations of the trend lines a)–f), describing the contents of image Y in relation to the object size, O_p is calculated by H_{init}^1 . For further modeling, trend line b) is chosen since it offers the lowest difference between O_p and \hat{O}_p^1 at H_{init}^1 . A value of $\hat{H}^1 = 12.9$ is calculated by integrating \hat{O}_p^1 (0.015) in the equation associated to trend line b). The segmentation of Y by \hat{H}^1 results in a mean relative object number of $\hat{O}_p(\hat{H}^1)^1 = 0.0171$, which shows a slightly higher value of 0.0021 than \hat{O}_p^1 . These results are nearly independent of the initially selected value of H_{init}^1 .

The next step encompasses the automatic creation of the coarser superlevels according to user-defined values of the relative percentage \hat{E}^l of the mean relative object number of level l ($l \neq 1, R$) to $\hat{O}_p(\hat{H}^1)^1$. \hat{E}^l is set to 50% ($l = 2$), 25% ($l = 3$), 17.5% ($l = 4$), 10% ($l = 5$), 5% ($l = 6$), and 2.5% ($l = 7$). The integration of the related values of \hat{O}_p^l into the equation describing trend line 2) results in values of \hat{H}^l ranging from 18.7 ($l = 2$) to 67.0 ($l = 7$).

As shown in Fig. 5, the mean relative object number of the levels ($l = 1-7$), decomposed by \hat{H}^l , is nearly identical to the intended values. Therefore, the presented method seems to be able to automatically model the parameters for the creation of

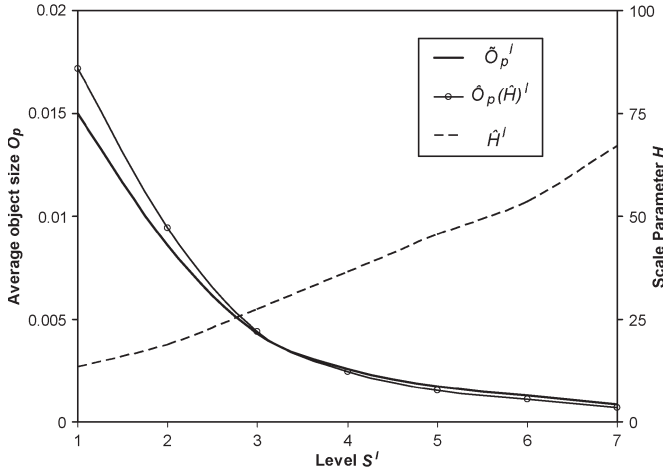


Fig. 5. Fit of the intended value of \hat{O}_p^l ($= 0.015$) to the average relative object number \hat{O}_p^l of the segmented levels, decomposed by the modeled scale parameter \hat{H}^l .

an irregular graph structure according to user requirements. This replaces the time-consuming trial-and-error procedures for the adaptation of H to the image content. Additionally, over- and undersegmentation of an image are automatically avoided. In particular, oversegmentation may lead to serious performance problems in the processing of large data sets due to memory constraints. In contrast, undersegmentation causes a loss of fine detail. The segmentation of the lowest level is the most important step in the generation of the graph structure since the properties of the coarser superlevels depend on the mean object size of S^1 .

C. Effectiveness of the Markov Image Models

In order to evaluate the quality of the proposed change detection approach and to derive transferable parameter settings, the HMAP estimation and the hybrid Markov image model are computed with different parameters on a diversified irregular graph structure to analyze the following: 1) the quality of the HMAP algorithm as well as the hybrid Markov image model in comparison to uniscale classification results. In particular, the influence of the hierarchical graph structure and smoothness parameter γ on the classification accuracy is investigated; and 2) the performance of the Markov image models in dependence of the graph structure and γ .

The hybrid Markov model is computed on a graph Ψ_L with a varying number of levels ($L = 4, 6, 8$) and different scale parameters H in the range of [12–32]. The parent prior was empirically set to 0.9. By the use of Ψ_6 , an additional level is integrated between levels S^1 and S^2 as well as S^2 and S^3 of Ψ_4 , respectively. H^3 and H^5 of Ψ_6 are, therefore, identical to H^2 and H^3 of Ψ_4 . In comparison, using Ψ_8 , two coarser levels are generated above S^5 of Ψ_6 .

The ICM algorithm is computed with $\gamma = 1.0, 3.0$, and 5.0 as well as γ_{adapt} in the range of $\gamma_{\text{min}} = 1.0$ and $\gamma_{\text{max}} = 5.0$ on a restricted region according to the class label representation $f(x_s)$ of a leaf object on its super objects after HMAP estimation. In Table III, the values of γ_{adapt} are shown in dependence of L . The ICM algorithm stops if the percentage of objects

TABLE III
VALUES OF THE ADAPTIVE SMOOTHNESS PARAMETER γ_{adapt}
IN DEPENDENCE OF $f(x_s)$ FOR Ψ_L ($L = 4, 6, 8$)

$f(x_s)$	Number of level		
	4	6	8
5	-	-	1.0
4	-	-	1.8
3	-	1.0	2.6
2	-	2.33	3.4
1	1.0	3.66	4.2
0	5.0	5.0	5.0

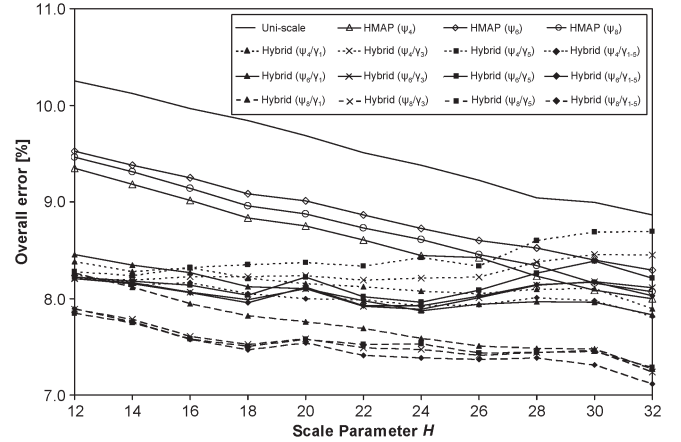


Fig. 6. OER of the uniscale classification, the HMAP estimation, and the hybrid Markov model in dependence of H ($= 12\text{--}32$), L ($= 4, 6, 8$), and different values of γ (1.0, 3.0, and 5.0; 1.0–5.0).

with different labels at iterations $1 + n$ and 1 is lower than a predefined threshold of 0.02%.

Accuracy: In Fig. 6, the accuracy assessment of the uniscale classification, the HMAP, and the hybrid Markov model is illustrated by plots of the overall error rates (OER, i.e., the percentage of the erroneously labeled reference pixels, including false positives and false negatives) of class $C+$ in dependence of the altered parameters.

The classification results confirm that the proposed HMAP estimation and the hybrid Markov model applied on irregular graphs always exhibit a much lower OER compared with that obtained using only one decomposition level.

Regarding the results of the uniscale segmentation as well as of the HMAP approach, a nearly linear decrease of the OER with increasing H can be observed in the range of [12–32]. The decrease of the OER resulting from the uniscale classification is about 0.69% per H , starting from 10.25% at $H = 12$ to 8.86% at $H = 32$. The trend lines of the HMAP approach have nearly the same decrease of about 0.62% per H . However, the HMAP trend lines start at about 0.72% (Ψ_6) to 0.90% (Ψ_4) below the OER of the uniscale classification approach at $H = 12$.

The HMAP results show very similar classification accuracies. Therefore, the number of levels does not seem to have a significant impact on the HMAP classification accuracy. Surprisingly, the lowest OERs are calculated on Ψ_4 . Slightly higher OERs are obtained on Ψ_6 . This is caused by an increased false alarm rate (i.e., the percentage of reference pixels that do not belong to $C+$ that are erroneously detected as $C+$). Therefore, using Ψ_6 , created by the integration of additional

layers between S^1 and S^2 as well as S^2 and S^3 of Ψ_4 , reduces the smoothing effect of the HMAP approach. The integration of two coarser levels for the creation of Ψ_8 improves the classification accuracy in comparison to the HMAP estimation on Ψ_6 by reducing the missed detection rate (i.e., the percentage of reference pixels of $C+$ that are erroneously detected as U or $C-$). However, the OER is slightly higher in comparison on the HMAP on Ψ_4 . In comparison to the number of levels of Ψ , H has a greater influence on the classification accuracy of the HMAP approach, which improves with an increasing H .

Looking at the results of the hybrid Markov image model, the following points can be stated: In comparison to the HMAP results, the hybrid Markov model generates a much lower OER for all parameter settings in the range of $H = [12-26]$. This increase of accuracy is related to the integration of spatial-contextual information into the labeling process using noncausal Markov modeling. However, there are significant differences in the OER caused by the parameter settings and the graph structure. At $H = 12$, the OERs are very similar, and they exhibit values in the interval of 7.89% (Ψ_8/γ_5) and 8.45% (Ψ_6/γ_1). At this position, the greatest increase in accuracy in relation to the HMAP approach can also be stated. With an increasing H , the difference between the maximum and minimum OER increases, and it reaches the highest difference (1.58%) at $H = 32$ between 8.70% (Ψ_4/γ_5) and 7.11% (Ψ_8/γ_{1-5}). Hence, for $H > 26$, the classification accuracy of the hybrid Markov model for Ψ_4 and Ψ_6 is nearly similar to the OERs of the HMAP approach. It is obvious that, with an increasing H , the number of levels of Ψ gains importance and leads to significant differences in classification accuracy. In contrast to HMAP estimation, the accuracy improves with an increasing number of levels.

The decrease of the OER with an increasing H , which has been stated for the HMAP estimation, can only be observed for the hybrid Markov model for Ψ_8 . However, the influence is not as pronounced as in the HMAP approach, and the accuracies are nearly identical in the range of $H = [18-28]$ for (Ψ_8/γ_3), (Ψ_8/γ_5), and (Ψ_8/γ_{1-5}), with an interval between 7.39% and 7.58%.

The highest classification accuracies over all trend lines are reached for Ψ_8 . Additionally, trend lines for (Ψ_8/γ_3), (Ψ_8/γ_5), and (Ψ_8/γ_{1-5}) offer nearly identical OERs, which are independent from the parameters chosen. This can also be stated for the trend lines for Ψ_6 in the range of $H = [12-26]$. In contrast, the results derived for Ψ_4 are more sensitive to the selection of γ .

The highest overall accuracies are reached between $H = [14-32]$ by (Ψ_8/γ_{1-5}), with OERs in the range of 7.75% ($H = 4$) and 7.11% ($H = 32$). These accuracies are up to 1.5% higher than the HMAP results. Also, for Ψ_4 , the lowest OERs can be observed using γ_{adapt} in the whole range of $H = [12-32]$, while at Ψ_6 , the generation of the lowest OER by (Ψ_6/γ_{1-5}) is replaced at $\geq H = 24$ by (Ψ_5/γ_1). In contrast, the lowest accuracies are reached using γ_5 , particularly for Ψ_4 and Ψ_6 .

It can be concluded that an increasing number of levels in the graph enhance the classification accuracy and decrease the influence of the remaining parameters on the results.

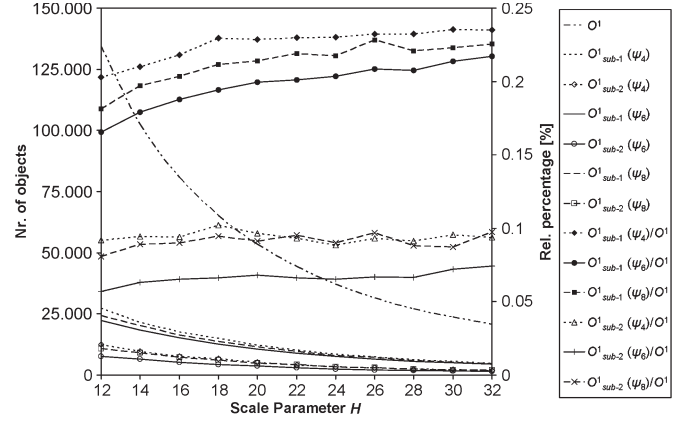


Fig. 7. Performance of the hybrid Markov model in dependence of H and L on all objects of S_1 as well as of $S_{\text{sub-1}}^1$ and $S_{\text{sub-2}}^1$.

The change map of Y_{sub} is shown in Fig. 4, derived for Ψ_8 , with $H = 24$ and γ_{1-5} . The map shows a coherent change area caused by the receding flooding. Since no quadtree structure, but an irregular graph, has been used in the processing, no block artifacts are visible in the map. Most errors occur at the border of the flood surface, and they are predominantly misclassified as class U . On the one hand, these are related to the flooded vegetation, which shows nearly similar radar cross sections between t_1 and t_2 , and, on the other hand, to a slight decrease of the flood extent between the acquisition of the orthophotos and the SAR data at t_1 . False alarms are very sparse, and they occur predominantly in urban areas. These errors could be further reduced by methods integrating elevation information into the labeling process [25], [38].

Performance: The HMAP estimation is a very fast technique due to its noniterative inference on irregular hierarchical graphs. The performance depends on the number of nodes S of Ψ and, therefore, on H^1 as well as on L . This results in a fixed computational complexity per site, i.e., the computational effort increases linearly with a decreasing S . Accordingly, the performance of the HMAP approach ($H^1 = 12$) on Ψ_4 ($S = 181\,250$) is $\sim 37\%$ faster than that on Ψ_8 ($S = 286\,900$) and $\sim 34.5\%$ faster than that on Ψ_6 ($S = 272\,200$). In contrast, the computational efficiency on Ψ_8 at $H = 12$ ($S = 286\,900$) is $\sim 86.2\%$ higher than that at $H = 32$ ($S = 39\,500$).

In comparison, the noncausal MRFs are characterized by an iterative minimization of an energy function. In a per-pixel application, the MAP estimation must be computed on Y_{sub} for all elements ($\sim 6.43 \times 10^6$ pixels) in each iteration. In that case, the ICM algorithm achieved convergence after 12 iterations ($V_{sp} = 8$ and $\gamma = 2.0$). Using the ICM algorithm on irregular planar graphs, the performance of this noncausal MRF approach is strongly increased due to the following facts.

The decomposition of an image by H leads to a strongly reduced number of elements integrated into the MAP estimation. When applied to the whole irregular planar graph with O^1 , this number decreases with an increasing H from 103 350 ($H = 12$) to 20 780 ($H = 32$) (Fig. 7).

A strong increase in performance is reached by restricting the ICM algorithm to $O^1_{\text{sub-1}}$, derived in Section II-D using the HMAP labeling approach. The value of $O^1_{\text{sub-1}}$ shows $\sim 16.5\%$ – 23.5% of O^1 . The difference between O^1 and $O^1_{\text{sub-1}}$

decreases with larger values of H (Fig. 7). Therefore, the performance increase is particularly significant on images decomposed by a small value of H . $O_{\text{sub-1}}^1$ decreases continually with an increasing H , which is nearly independent on Ψ_4 , Ψ_6 , and Ψ_8 . The highest values of $O_{\text{sub-1}}^1$ in the range of 27 250 ($H = 12$) and 4890 ($H = 32$) are achieved for Ψ_4 . In contrast, the lowest values of $O_{\text{sub-1}}^1$ are generated for Ψ_6 . This results from the integration of additional intermediate levels into the graph structure, which favors increased identity of the class labeling of a node at S^1 and its ancestors.

Additionally, after the first ICM iteration, $O_{\text{sub-1}}^1$ is further decreased to $O_{\text{sub-2}}^1$ for an increase of the processing time (Fig. 7). Objects with no common border to the other elements of $S_{\text{sub-1}}^1$ are removed from the MAP estimation since they can only change their labeling in the first iteration. This reduces the object number in the subsequent iterations to $\sim 5.5\%$ – 10.0% in comparison to O^1 .

In addition to the number of nodes O^1 , checked by the ICM algorithm for a possible label change, the performance of the hybrid Markov model further depends on the size of the neighborhood system V_{sp} and the speed of convergence. In pixel-based applications, usually, four- or eight-neighborhood systems are used. However, on irregular planar graphs, the average size of V_{sp} is nearly similar for all computations, with a range of 3.5–3.9 neighbors per MAP estimation. With an increasing H , the average size of V_{sp} slightly reduces.

The ICM converges independently of the chosen parameters in three to four iterations. This is a strong decrease in comparison to 12 iterations of a per-pixel application of the MAP estimation on Y_{sub} . The mean number of iterations of the ICM with γ (1.0, 3.0, and 5.0) and γ_{adapt} (1.0–5.0) processed on Ψ_4 , Ψ_6 , and Ψ_8 over $H = [12-32]$ shows that the fastest convergence is reached by using γ_{adapt} in 3.30 iterations. This value increases by the use of constant values of γ ($\gamma = 1.0 : 3.45$, $\gamma = 3.0 : 3.78$, and $\gamma = 5.0 : 3.93$). The use of γ_{adapt} shows that the adaptation of γ to confidence maps can be effectively applied to reduce the number of iterations and also to increase the classification accuracy.

When applied to Y_{sub} , the described hybrid Markov approach takes ~ 25 s of processing time on a hierarchical graph with eight levels and a total number of $9 * 10^4$ nodes (CPU details: Intel Xeon 5460 Core Duo @ 3.16-GHz processor with a 3-GB RAM). The HMAP estimator accounts for $\sim 70\%$, and the noncausal Markov model accounts for $\sim 30\%$ of this time. The generation of the graph takes more processing time (~ 60 s). In contrast, the automatic thresholding approach only requires ~ 30 s in deriving thresholds from the entire NCI data.

IV. CONCLUSION

In this paper, an unsupervised method for the extraction of flood-induced change areas in multitemporal SAR data has been presented. The experimental results obtained on a bitemporal TerraSAR-X data set of South West England, with an overall error (OER) of the class $C+$ of $\sim 7.5\%$, confirm the effectiveness of this approach.

A tile-based parametric thresholding approach under the GG assumption is successfully applied to an NCI image to

automatically solve the three-class change detection problem in large-size data with small *a priori* class probabilities within a short time. The thresholding result is used in initializing a hybrid context-based model, combining causal with noncausal Markov image modeling on automatically generated irregular hierarchical graphs.

The integration of the hierarchical context in the labeling process is accomplished by the adaptation of HMAP estimation using Markov chains in scale. The supplementary integration of spatial-contextual information in the classification using noncausal MRF modeling leads to an increase in accuracy of up to 1.5% in comparison to the HMAP estimation.

To decrease the computational demand of noncausal Markov models, the energy minimization process is defined as the MRF approach, which is applied on the finest tree level to a restricted region specified by the use of confidence maps.

Due to its high accuracy and fast performance, this unsupervised hybrid change detection approach is useful for operational rapid mapping activities. It is important to note that, although this method has been presented in the specific context of the analysis of flood-induced change areas, it could be used in any change-detection application. Additionally, it has been successfully used for flood detection in single-polarized single-temporal SAR data. For future work, it would be an interesting topic to investigate the integration of elevation information into the process of extracting flood-related changes in feature maps. Therefore, methods using digital elevation models for improved flood detection [25], [38] have to be modified and adapted to this application.

ACKNOWLEDGMENT

The authors would like to thank the Environment Agency of England and Wales for providing the orthophotos of the Tewkesbury region during the flooding and the three anonymous reviewers for their helpful comments.

REFERENCES

- [1] Z. W. Kundzewicz, U. Ulbrich, T. Bruecher, D. Graczyk, A. Krueger, G. Leckebusch, L. Menzel, I. Pińskwar, M. Radziejewski, and M. Szwed, "Summer floods in Central Europe—Climate change track?" *Natural Hazards*, vol. 36, no. 1/2, pp. 165–189, Sep. 2005.
- [2] S. Voigt, T. Kemper, T. Riedlinger, R. Kiefl, K. Scholte, and H. Mehl, "Satellite image analysis for disaster and crisis-management support," *IEEE Trans. Geosci. Remote Sens.*, vol. 45, no. 6, pp. 1520–1528, Jun. 2007.
- [3] P. Deer, "Digital change detection in remotely sensed imagery using fuzzy set theory," Ph.D. dissertation, Dept. Geograph. Comput. Sci., Univ. Adelaide, Adelaide, Australia, 1998.
- [4] L. Bruzzone and D. F. Prieto, "Automatic analysis of the difference image for unsupervised change detection," *IEEE Trans. Geosci. Remote Sens.*, vol. 38, no. 3, pp. 1171–1181, May 2000.
- [5] G. Moser and S. B. Serpico, "Generalized minimum-error thresholding for unsupervised change detection from SAR amplitude imagery," *IEEE Trans. Geosci. Remote Sens.*, vol. 44, no. 10, pp. 2972–2982, Oct. 2006.
- [6] J. F. Mas, "Monitoring land-cover changes: A comparison of change detection techniques," *Int. J. Remote Sens.*, vol. 20, no. 1, pp. 139–152, Jan. 1999.
- [7] Y. Bazi, L. Bruzzone, and F. Melgani, "An unsupervised approach based on the generalized Gaussian model to automatic change detection in multitemporal SAR images," *IEEE Trans. Geosci. Remote Sens.*, vol. 43, no. 4, pp. 874–887, Apr. 2005.

- [8] F. Melgani, G. Moser, and S. B. Serpico, "Unsupervised change detection methods for remote sensing images," *Opt. Eng.*, vol. 41, no. 12, pp. 3288–3297, Dec. 2002.
- [9] G. Moser and S. B. Serpico, "Unsupervised change detection from multichannel SAR data by Markovian data fusion," *IEEE Trans. Geosci. Remote Sens.*, vol. 47, no. 7, pp. 2114–2128, Jul. 2009.
- [10] Q. Jackson and D. Landgrebe, "Adaptive Bayesian contextual classification based on Markov random fields," *IEEE Trans. Geosci. Remote Sens.*, vol. 40, no. 11, pp. 2454–2463, Nov. 2002.
- [11] T. Kasetkasem and P. K. Varshney, "An image change detection algorithm based on Markov random field models," *IEEE Trans. Geosci. Remote Sens.*, vol. 40, no. 8, pp. 1815–1823, Aug. 2002.
- [12] R. Fjørtoft, Y. Delignon, W. Pieczynski, M. Sigelle, and F. Tupin, "Unsupervised classification of radar images using hidden Markov chains and hidden Markov random fields," *IEEE Trans. Geosci. Remote Sens.*, vol. 41, no. 3, pp. 675–686, Mar. 2003.
- [13] N. Giordana and W. Pieczynski, "Estimation of generalized multisensor hidden Markov chains and unsupervised image segmentation," *IEEE Trans. Pattern Anal. Mach. Intell.*, vol. 19, no. 5, pp. 465–475, May 1997.
- [14] S. Derrode, G. Mercier, and W. Pieczynski, "Unsupervised change detection in SAR images using a multicomponent HMC model," in *Proc. 2nd Int. Workshop Anal. Multi-Temp. Remote Sens. Images*, Ispra, Italy, 2003, vol. 3, pp. 195–203.
- [15] C. Carincotte, S. Derrode, and S. Bourennane, "Unsupervised change detection on SAR images using fuzzy hidden Markov chains," *IEEE Trans. Geosci. Remote Sens.*, vol. 44, no. 2, pp. 432–441, Feb. 2006.
- [16] C. Bouman and M. Shapiro, "A multiscale random field model for Bayesian image segmentation," *IEEE Trans. Image Process.*, vol. 3, no. 2, pp. 162–177, Mar. 1994.
- [17] Z. Kato, M. Berthod, and Z. Zerubia, "A hierarchical Markov random field model and multi-temperature annealing for parallel image classification," *Graph. Models Image Process.*, vol. 58, no. 1, pp. 18–37, Jan. 1996.
- [18] J. M. Laferté, P. Pérez, and F. Heitz, "Discrete Markov image modeling and inference on the quadtree," *IEEE Trans. Image Process.*, vol. 9, no. 3, pp. 390–404, Mar. 2000.
- [19] R. Wilson and C. Li, "A class of discrete multiresolution random fields and its application to image segmentation," *IEEE Trans. Pattern Anal. Mach. Intell.*, vol. 25, no. 1, pp. 42–56, Jan. 2003.
- [20] J.-N. Provost, C. Collet, P. Rostaing, P. Pérez, and P. Boutheymy, "Hierarchical Markovian segmentation of multispectral images for the reconstruction of water depth maps," *Comput. Vis. Image Understanding*, vol. 93, no. 2, pp. 155–174, Feb. 2004.
- [21] C. Collet and F. Murtagh, "Multiband segmentation based on a hierarchical Markov model," *Pattern Recog.*, vol. 37, no. 12, pp. 2337–2347, Dec. 2004.
- [22] M. Luetgten, W. Karl, and A. Willsky, "Efficient multiscale regularization with applications to the computation of optical flow," *IEEE Trans. Image Process.*, vol. 3, no. 1, pp. 41–64, Jan. 1994.
- [23] W. Irving, P. Fieguth, and A. Willsky, "An overlapping tree approach to multiscale stochastic modeling and estimation," *IEEE Trans. Image Process.*, vol. 6, no. 11, pp. 1517–1529, Nov. 1997.
- [24] A. Lopes, E. Nezry, R. Touzi, and H. Laur, "Maximum a posteriori speckle filtering and first order texture models in SAR images," in *Proc. IGARSS*, College Park, MD, 1990, vol. 3, pp. 2409–2412.
- [25] S. Martinis, A. Twele, and S. Voigt, "Towards operational near real-time flood detection using a split-based automatic thresholding procedure on high resolution TerraSAR-X data," *Natural Hazards Earth Syst. Sci.*, vol. 9, no. 2, pp. 303–314, 2009.
- [26] J. Kittler and J. Illingworth, "Minimum error thresholding," *Pattern Recog.*, vol. 19, no. 1, pp. 41–47, Jan./Feb. 1986.
- [27] K. Sharifi and A. Leon-Garcia, "Estimation of shape parameter for generalized Gaussian distributions in subband decompositions of video," *IEEE Trans. Circuits Syst. Video Technol.*, vol. 5, no. 1, pp. 52–56, Feb. 1995.
- [28] L. Lucchese and S. K. Mitra, "An algorithm for unsupervised color image segmentation," in *Proc. IEEE 2nd Workshop Multimedia Signal Process.*, Redondo Beach, CA, 1998, pp. 33–38.
- [29] R. M. Haralick and L. G. Sharipo, "Image segmentation techniques," *Comput. Vis., Graph., Image Process.*, vol. 29, no. 1, pp. 100–132, Jan. 1985.
- [30] L. Bruzzone and L. Carlin, "A multilevel context-based system for classification of very high spatial resolution images," *IEEE Trans. Geosci. Remote Sens.*, vol. 44, no. 9, pp. 2587–2600, Sep. 2006.
- [31] M. Baatz and A. Schäpe, "Object-oriented and multi-scale analysis in semantic networks," in *Proc. 2nd Int. Symp. Oper. Remote Sens.*, Enschede, The Netherlands, 1999.
- [32] *eCognition Developer 8 User Guide*, Definiens AG, Munich, Germany, 2009.
- [33] G. D. Forney, "The Viterbi algorithm," *Proc. IEEE*, vol. 61, no. 3, pp. 268–278, Mar. 1973.
- [34] J. Besag, "Spatial interaction and the statistical analysis of lattice systems," *J. R. Stat. Soc., B*, vol. 36, no. 2, pp. 192–236, 1974.
- [35] S. Z. Li, *Markov Random Field Modeling in Image Analysis*. London, U.K.: Springer-Verlag, 2009.
- [36] J. Besag, "On the statistical analysis of dirty pictures," *J. R. Stat. Soc., B*, vol. 48, no. 3, pp. 259–302, 1986.
- [37] S. Geman and D. Geman, "Stochastic relaxation, Gibbs distributions and the Bayesian restoration of images," *IEEE Trans. Pattern Anal. Mach. Intell.*, vol. 6, no. PAMI-6, pp. 721–741, Jun. 1984.
- [38] D. C. Mason, R. Speck, B. Devereux, G. J.-P. Schumann, J. C. Neal, and P. D. Bates, "Flood detection in urban areas using TerraSAR-X," *IEEE Trans. Geosci. Remote Sens.*, vol. 48, no. 2, pp. 882–894, Feb. 2010.



Sandro Martinis received the M.Sc. degree in physical geography, physics, and remote sensing from the Ludwig-Maximilians-University of Munich, Munich, Germany, in 2006. He is currently working toward the Ph.D. degree in the German Remote Sensing Data Center (DFD), German Aerospace Center (DLR), Wessling, Germany.

From 2006 to 2007, he was a Research Associate with the Institute of Geology, Munich, where he worked on the development of remote sensing methods for glacier monitoring. He is involved in development activities at DLR/DFD's Center for Satellite-Based Crisis Information (ZKI). His main research activities are in the areas of operational flood extraction and change detection from synthetic aperture radar data.



André Twele received the M.Sc. degree in geography and applied geoinformatics from Westfälische Wilhelms-Universität Münster, Münster, Germany, in 2003.

As part of his M.Sc. thesis research, he spent eight months with the Joint Research Centre (JRC), European Commission, working on remote-sensing-based methods for burned-area assessment and post-fire regeneration monitoring. From 2003 to 2006, he was a Research Associate with the Cartography, GIS and Remote Sensing Department, Göttingen University, Göttingen, Germany, working in an international research program on rainforest monitoring. In 2007, he joined the German Remote Sensing Data Center (DFD), German Aerospace Center (DLR), Wessling, Germany, where he is currently coordinating a research project focused on operational methods for flood detection based on synthetic aperture radar remote sensing data. Furthermore, he is involved in method development activities at DLR/DFD's Center for Satellite-Based Crisis Information (ZKI), which is contributing to several national and international activities and projects in the field of disaster mitigation, humanitarian relief, and civil security.

Mr. Twele is a member of the Remote Sensing and Photogrammetry Society of Nottingham (RSPSoc).



Stefan Voigt received the M.Sc. degree in physical geography, physics, and remote sensing from the Ludwig-Maximilians-University of Munich, Munich, Germany, in 1997 and the Ph.D. degree from Berne University, Bern, Switzerland, in 2000, working on remote sensing for runoff/flood forecasting.

Since 2000, he has been with the German Remote Sensing Data Center (DFD), German Aerospace Center (DLR), Wessling, Germany, leading a research group and coordinating with the DLR Center for Satellite-Based Crisis Information (ZKI). From 2001 to 2008, he coordinated an international research initiative on innovative technologies for detection, prevention, and monitoring of uncontrolled coal seam fires in China. He is actively involved in numerous national and international research activities and projects in remote sensing for disaster mitigation, humanitarian relief, and civil security matters.

5.3 Paper 3

Martinis, S. & Twele, A., 2010: A hierarchical spatio-temporal Markov model for improved flood mapping using multi-temporal X-band SAR data. – *Remote Sensing*, 2 (9), 2240-2258.

Article

A Hierarchical Spatio-Temporal Markov Model for Improved Flood Mapping Using Multi-Temporal X-Band SAR Data

Sandro Martinis * and André Twele

German Aerospace Center (DLR), German Remote Sensing Data Center (DFD), Oberpfaffenhofen, 82234 Wessling, Germany; E-Mail: andre.twele@dlr.de

* Author to whom correspondence should be addressed; E-Mail: sandro.martinis@dlr.de; Tel.: +49-8153-283-034; Fax: +49-8153-281-445.

Received: 28 July 2010; in revised form: 10 September 2010 / Accepted: 10 September 2010 / Published: 17 September 2010

Abstract: In this contribution, a hybrid multi-contextual Markov model for unsupervised near real-time flood detection in multi-temporal X-band synthetic aperture radar (SAR) data is presented. It incorporates scale-dependent, as well as spatio-temporal contextual information, into the classification scheme, by combining hierarchical marginal posterior mode (HMPM) estimation on directed graphs with noncausal Markov image modeling related to planar Markov random fields (MRFs). In order to increase computational performance, marginal posterior-based entropies are used for restricting the iterative bi-directional exchange of spatio-temporal information between consecutive images of a time sequence to objects exhibiting a low probability, to be classified correctly according to the HMPM estimation. The Markov models, originally developed for inference on regular graph structures of quadtrees and planar lattices, are adapted to the variable nature of irregular graphs, which are related to information driven image segmentation. Entropy based confidence maps, combined with spatio-temporal relationships of potentially inundated bright scattering vegetation to open water areas, are used for the quantification of the uncertainty in the labeling of each image element in flood possibility masks. With respect to accuracy and computational effort, experiments performed on a bi-temporal TerraSAR-X ScanSAR data-set from the Caprivi region of Namibia during flooding in 2009 and 2010 confirm the effectiveness of integrating hierarchical as well as spatio-temporal context into the labeling process, and of adapting the models to irregular graph structures.

Keywords: Markov random fields (MRFs); hierarchical marginal posterior mode (HMPM) estimation; irregular graph; spatio-temporal context; TerraSAR-X; automatic thresholding; generalized Gaussian distribution; change detection; flood mapping; flood possibility mask; Namibia

1. Introduction

Spaceborne synthetic aperture radar (SAR) remote sensing is currently the most effective technology for a regular observation of the Earth's surface. By analyzing multi-date images, it is possible to get a synoptic view of temporal land-cover/land-use behavior. This is of particular importance in disaster management for the detection of abrupt changes caused by natural catastrophes like earthquakes, hurricanes and tsunamis, as well as for the monitoring of events characterized by a longer temporal evolution such as flooding and forest fires. SAR plays a particularly important role in flood mapping, due to its near all-weather/day-night capabilities and its effectiveness to detect inundation beneath different kinds of vegetation canopies [1-3].

A large portion of the activations (~46%, current as of August 19, 2010) of the International Charter of Space and Major Disasters (<http://www.disasterscharter.org>) are related to flood situations. At the same time, the number of SAR sensors that allow monitoring inundations with a high temporal and spatial resolution has strongly increased. For this reason, automatic methods are necessary to generate detailed flood maps on a near real-time basis to support decision makers as well as humanitarian relief organizations during disaster management. It can further be useful to create maps, which show the probability of correctness related to the classification results. This supplementary information source may be important for performance evaluations of hydrodynamic models.

Many techniques have been presented to identify change areas in remote sensing data [4,5]. The two most common image change detection algorithms are labeling of feature maps (e.g., difference images [6], normalized difference images [7], ratio data [8], and log ratio data [9]) and comparison of individual classification maps [10], usually called Post-Classification Comparison (PCC). In contrast to the classification of feature maps, PCC can provide a complete matrix of change directions. However, its performance naturally depends on the accuracy of each single classification map. It is therefore of great importance to integrate the temporal dimension into the classification process in order to improve results in terms of accuracy and reliability [11,12].

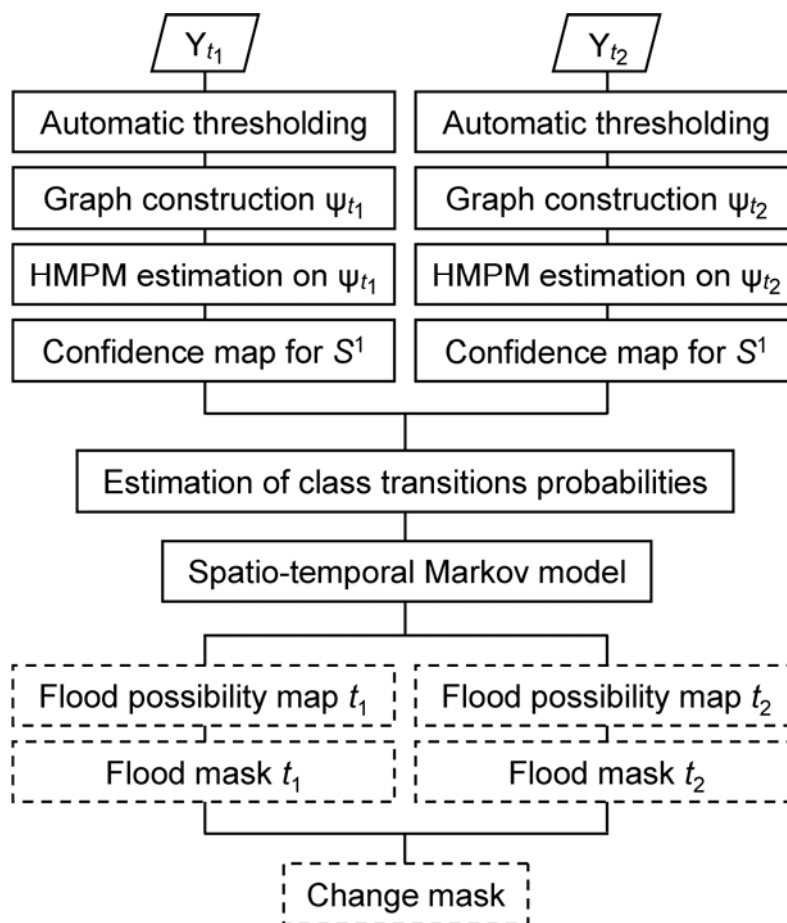
Markov random fields (MRFs) [13,14] represent an effective and theoretically well established probabilistic model for integrating different types of contextual information (e.g., spatial, hierarchical, and temporal) into the image labeling process. MRFs have also been adopted for an improved extraction of changes in remote sensing data. Spatial Markov modeling is applied to feature maps in several studies (e.g., [9,15,16]). A Markovian model considering spatial as well as hierarchical contextual information is presented by [7]. Several methods are proposed to integrate only temporal [12,17], as well as spatio-temporal [11,18,19], information into the Markov model for classification improvement.

The application of MRFs in image analysis is predominantly accomplished by using noncausal (e.g., [9,11,16,19-24]) and planar causal models (e.g., [15,23,25]) on regular planar lattice-based graphs. These models have the disadvantage that they must be applied to all pixels in the image. This results in an enormous computational complexity, which is more pronounced using noncausal MRFs due to their iterative nature of inference, in contrast to the non-iterative character of planar causal models. In addition, only a small neighborhood is considered in the labeling process.

In contrast to noncausal or planar causal models, hierarchical causal Markov models have the capacity to capture the intrinsic hierarchical nature of remote sensing data. These models can be applied in a non-iterative way on simple regular structures of quadtrees [26-31] or on more complex, however still regular, trees which try to overcome the blockiness of the classification result that is related to the nonstationarity of MRFs on quadtrees [26,32].

In just a few works in image analysis, Markov modeling is related to irregular graphs, whose elements have a strong correlation with real objects or areas of the Earth's surface: Feitosa *et al.* [12] use planar graphs for multi-temporal classification based on fuzzy Markov chains. In [33], hierarchical marginal posterior mode (HMPM) estimation is applied to a Multiscale Region Adjacency Tree, however without consideration of the altering relationship between parent and child nodes in the graph architecture. This is taken into account by [7], who adapt hierarchical maximum *a posteriori* (HMAP) estimation to irregular graphs. This work also presents a framework for the supplementary integration of spatial context into the labeling process in a time-efficient manner. This is accomplished by using noncausal Markov modeling on a restricted region of the finest tree-level specified by confidence maps derived from the HMAP labeling result. Even if the integration of spatial context results in an increase in accuracy, the applied noncausal Markov model is not adapted to the irregular nature of the planar graph.

This paper presents an unsupervised method for improved near real-time flood and change detection in multi-temporal TerraSAR-X data using a hybrid generative Markov model (Figure 1). The specific objectives are: (1) the combination of automatically initialized causal and noncausal Markov image models for integrating hierarchical as well as spatio-temporal context into the labeling process of the classes "Water", "No water" and "Potentially flooded vegetation"; (2) the adaptation of these models to irregular hierarchical as well as planar graphs; (3) the use of entropy-based confidence maps, derived in conjunction with hierarchical marginal posterior mode (HMPM) estimation, to restrict the noncausal Markov modeling step to regions that have been probably misclassified by the causal Markov model, and to generate flood possibility (FP) maps.

Figure 1. Block scheme of the proposed workflow.

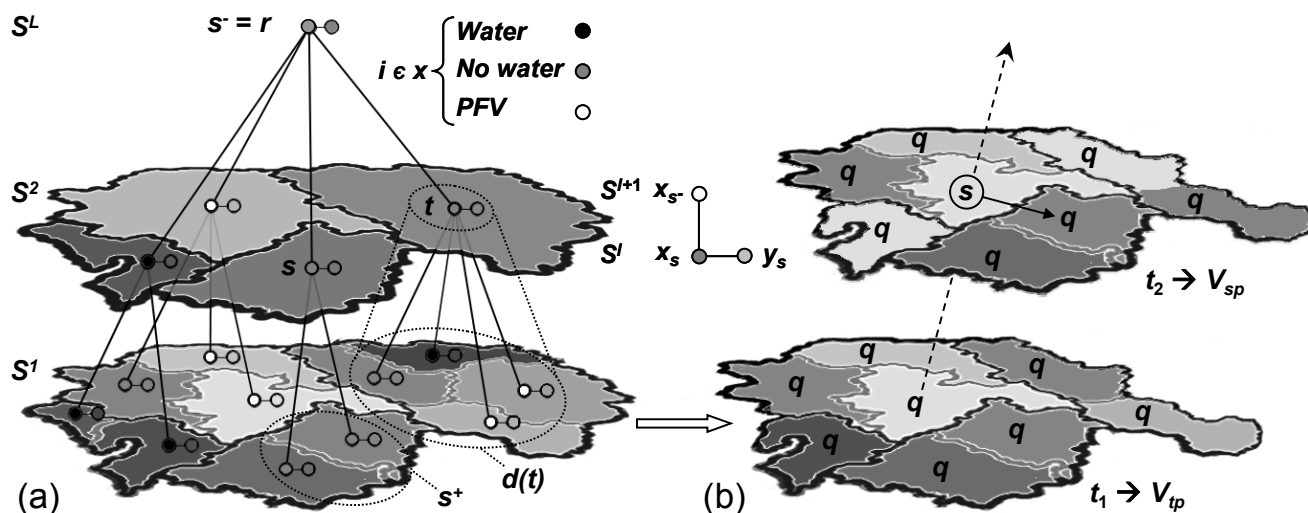
2. Methodology

2.1. Automatic Graph Construction

The multi-level representation of an image Y can be represented as a connected graph Ψ_L with L levels composed of a set of nodes S , where each node s apart from the root r has a unique parent node s^r (Figure 2(a)). A descendant node originating from s is denoted as node t . The set of nodes can be partitioned into different scale levels, $S = S^1 \cup S^2 \cup \dots \cup S^L$. The level decomposed by the lowest homogeneity parameter is S^1 , and the coarsest level consists of only one node $S^L = \{r, l = L\}$ (Figure 2(a)).

Several differences can be determined between the regular structure of quadtrees and irregular hierarchical graphs: in contrast to the predefined architecture of quadtrees, which are represented by four equally sized child objects per parent object, the number and size of child objects per irregular parent object vary as a result of an information-driven segmentation. Therefore, the number of nodes of the whole graph cannot be estimated before image segmentation is accomplished. This is related to problems of over- or under-segmentation. Considering the intra-scale dependencies, it can be stated that, in contrast to regular planar lattices, the size and number of the elements vary, as well as the border length between the center and the adjacent objects in a spatial neighborhood system of an irregular planar graph. These characteristics must be taken into account when generating the irregular graph and when applying the Markov models to this tree structure.

Figure 2. (a) Three-level independency graph corresponding to an irregular tree-structure. Left circles represent labeling of classes “Water”, “No water” and “Potentially flooded vegetation” (PFV), right circles represent the observations at each node s . **(b)** Irregular planar graphs of Y_{t_1} and Y_{t_2} with spatial V_{sp} and temporal V_{tp} neighborhood systems of center node s and its spatially and temporally adjacent objects q at t_2 .



For the automatic generation of the hierarchical graph according to user demands, the procedure described in [7] is adopted: First, several subsets of the SAR image are automatically selected to describe the heterogeneity of the SAR data. In the next step, a pre-segmentation of the subsets is performed by the fractal net evolution approach [34]. The homogeneity parameter is estimated, which leads to a decomposition of the entire image with average object sizes of the segments at each level, which come close to those intended by the user. This is accomplished by generating a database, which contains models describing the relationship between homogeneity parameter and object size according to data of different SAR sensor types and image contents. Finally, this model is selected for creating the whole graph which best fits to the pre-segmentation result.

2.2. Markov Image Modeling

Context is an essential information source for the analysis of remotely sensed data. Its necessity gains in importance with increasing spatial resolution of the data. The use of context means that each image element is not treated in isolation but as part of a spatial pattern. MRFs have been found to be useful tools for integrating different types of context into the classification process. In the following, two different Markov models are described: A causal model using a hierarchical marginal posterior mode (HMPM) estimation on two separated irregular hierarchical graphs, and a noncausal model leading to a bi-directional exchange of spatio-temporal information between multi-temporal planar graphs, represented by the finest levels of the hierarchical tree. Additionally, a hybrid model is proposed, which combines the HMPM estimation with the noncausal model for integrating hierarchical as well as spatio-temporal context into the labeling process in a time efficient manner using confidence maps.

2.2.1. Causal Markov Modeling on Irregular Graphs

Problem Definition and Statistical Modeling

For the set of nodes of an irregular hierarchical graph, two sets of random variables $X = (X_s)_{s \in S}$, $Y = (Y_s)_{s \in S}$, called “random fields” are considered. Each X_s takes its values in a finite set of M classes $\Omega = \{\omega_1, \omega_2, \dots, \omega_M\}$ and each Y_s takes its values in \mathfrak{R} . As common in Bayesian modeling, the labeling problem is then to estimate the “best” unobserved realization $X = x$ given the observed realization $Y = y$, where $y = (y_s)_{s \in S}$ is the observed image element.

Assuming a first-order Markov chain on a directed independence graph, where the conditioning for each node in $S^l (l \neq R)$ reduces to a dependence on its parent node in S^{l+1} , as well as a standard site-wise factorization for the observation model $P(y|x)$, the joint distribution factorizes as a product of local functions [27]:

$$P(x, y) = P(x_r) \prod_{s \neq r} P(x_s | x_{s^-}) \prod_{s \in S} P(y_s | x_s) \quad (1)$$

where $P(x_r)$ are the root prior probability, $\{P(x_s | x_{s^-})\}_{s \neq r}$ are the parent-child transition probabilities and $\{P(y_s | x_s)\}_{s \in S}$ are the data conditional likelihoods.

Model Parameters

For the definition of the prior model $P(X_s | X_{s^-})$ on the graph, the Potts-like distribution is used in [26], which favors likeliness of the labeling at s and s^- . In this work, the computation of an inter-scale transition probability matrix is proposed. This matrix contains the transition probability of each class combination between levels S^l and S^{l+1} ($l \neq R-1$) as the ratio of the area assigned to class ω_j at S^l and ω_i at S^{l+1} among the area of all elements assigned to class ω_j at S^l . At root r , a uniform prior probability with a value of $1/M$ is chosen.

The conditional likelihoods $P(y_s | x_s)$ of each node are modeled as Gaussian mixtures, defined by the scale dependent parameter vector $\theta_i^l = (\mu_i^l, \sigma_i^l)$, with mean μ_i^l and standard deviation σ_i^l of class i at level l . For the estimation of the initial class statistics, an automatic parametric tile-based thresholding procedure [7,35] under the generalized Gaussian assumption is used to estimate threshold values τ_1 between the classes “Water” and “No water” as well as τ_2 between the classes “No water” and “Potentially flooded vegetation (PFV)” in large-size SAR data with small class *a priori* probabilities in a time efficient manner. The threshold computation is accomplished by using a generalized Gaussian Kittler and Illingworth (GG-KI) thresholding algorithm [36,37] on a small number of tiles of the entire image Y selected according to the probability of the tiles to contain a bi-modal mixture distribution of the classes to be separated. The computed values of τ_1 and τ_2 are then applied to each level of the graph to derive θ_i^l .

Inference

One of the most interesting aspects of this model lies in the possibility to reach exact inference of the labels by computing the maximum *a posteriori* (MAP) $P(x|y)$ and marginal posterior mode (MPM)

probabilities $P(x_s|y)$ using an extension of the Viterbi algorithm [38] as well as the Baum algorithm [39] on Markov chains in scales [27,28]. The cost function associated to the MAP criterion is

$$C(\hat{x}, x') = 1 - \delta(\hat{x}, x') \tag{2}$$

with estimated and true class label \hat{x} and x' , and the Kronecker delta function δ . Equation (2) penalizes the discrepancies between configurations without considering how different these configurations are. The cost function

$$C(\hat{x}, x') = \sum_{s \in S} \delta(\hat{x}_s, x'_s) \tag{3}$$

accounts for this aspect and leads to the following Bayesian MPM estimator, which associates the most probable class given all the data to each node (Table 1):

Table 1. HMPM estimation on irregular hierarchical graphs.

Preliminary pass: At this downward recursion, the marginal priors $P(x_s)$ are computed for each s :
 $s \in S^{L-1} \dots S^2$, $P(x_s) = \sum_{x_{s^-}} P(x_s | x_{s^-}) P(x_{s^-})$

Bottom-up sw eep: The distribution of each x_s and couple (x_s, x_{s^-}) given all the data of the descendants (incl. y_s) is provided:
 Initialization ($s \in S^L$):
 $P(x_s | y_s) \propto P(y_s | x_s) P(x_s)$
 $P(x_s, x_{s^-} | y_s) = \frac{P(x_s | x_{s^-}) P(x_{s^-}) P(x_s | y_s)}{P(x_s)}$

Recursion ($s \in S^2 \dots S^L$):
 $P(x_s | y_{d(s)}) \propto P(y_s | x_s) P(x_s) \prod_{t \in s^+} \sum_{x_t} \left(\frac{P(x_t | y_{d(t)}) P(x_t | x_s)}{P(x_t)} \right) \varphi_{HMPM}$
 $P(x_s, x_{s^-} | y_{d(s)}) = \frac{P(x_s | x_{s^-}) P(x_{s^-}) P(x_s | y_{d(s)})}{P(x_s)} \quad \forall s \neq r$

Top-down sw eep: The complete marginal posteriors are reassembled from the partial marginals computed at the bottom-up sweep:
 Initialization (r):
 $P(x_r | y) = P(x_r | y_{d(r)})$
 $\hat{x}_r = \arg \max_{x_r} P(x_r | y)$

Recursion ($s \in S^{L-1} \dots S^1$):
 $P(x_s | y) = \sum_{x_{s^-}} \frac{P(x_s, x_{s^-} | y_{d(s)}) P(x_{s^-} | y)}{\sum_{x_s} P(x_s, x_{s^-} | y_{d(s)})}$
 $\hat{x}_s = \arg \max_{x_s} P(x_s | y)$

The weighting factor φ_{HMPM} takes into account the proportion of the spatial extent of a child node s to its predecessor s^- during the computation of the site-wise partial marginal posteriors $P(x_s | y_{d(s)})$ within the bottom-up pass.

2.2.2 Noncausal Markov Modeling on Bi-Temporal Planar Graphs

Spatio-Temporal Markov Model

Noncausal Markov models are, in contrast to hierarchical approaches, able to incorporate intra-spatial context between adjacent nodes of an undirected graph as well as temporal information into the labeling process. In the following, the pixel-based spatio-temporal Markov model proposed in [11] is reformulated and adapted to irregular planar graphs. In contrast to a uni-directed “cascade” approach [40] analyzing a sequence of images in chronological order, this model accomplishes an iterative mutual exchange of information between a sequence of multi-temporal images.

For the sake of simplicity, a bi-temporal sequence is considered consisting of two registered images Y_{t_1} and Y_{t_2} , which are acquired at times t_1 and t_2 , respectively. Each image is represented by an irregular hierarchical graph and labeled according to the HMPM estimation. For the application of the spatio-temporal model, the lowest levels of both graphs are synchronized by intersecting the two segmentations in order to retrieve equal object borders at t_1 and t_2 (Figure 2(b)).

The sets of possible labels for the related planar graphs are $\Lambda = \{\lambda_1, \lambda_i, \dots, \lambda_N\}$ at t_1 and $\Omega = \{\omega_1, \omega_i, \dots, \omega_M\}$ at t_2 . In the following, the labeling of Y_{t_2} , given Y_{t_1} and Λ is considered. The optimal labeling of all image elements according to the MAP decision criterion is characterized by an enormous computational complexity. The processing demand can be substantially reduced by modeling the conditional prior probability of image elements within a local neighborhood associated with a clique system, which is a subset of adjacent image elements in a neighborhood system. According to the Hammersly-Clifford theorem [41], describing MRFs-Gibbs equivalence, the combination of the MAP estimation with MRFs makes the classification task equivalent to the minimization of the Gibbs energy function U expressed in the following relation:

$$P(x_s | y_s, X_{sp}, X_{tp}) = Z^{-1} \exp^{-U(x_s, y_s, X_{sp}, X_{tp})} \quad (4)$$

where Z is a normalizing factor called the partition function and X_{sp} and X_{tp} are subsets of the labels of the respective images in predefined spatial V_{sp} and temporal V_{tp} neighborhood systems. The Iterated Conditional Modes (ICM) algorithm [42] represents a computationally moderate solution of the MRF-MAP estimates, converging to a local, but usually sufficient minimum of Equation (4). Assuming that the contribution of spatial and temporal context is separable and additive, the Gibbs energy function to be minimized for node s by the ICM algorithm can be formulated as

$$U(x_s, y_s, X_{sp}, X_{tp}) = U_{data}(\cdot) + \gamma_{sp} U_{sp}(\cdot) + \gamma_{tp} U_{tp}(\cdot) \quad (5)$$

where γ_{sp} and γ_{tp} control the influence of spatial and temporal context into the flood detection process, respectively. Assuming conditional independence of y given x , the data term U_{data} can be formulated as:

$$U_{data}(X_s = \omega_i, Y_s = y_s) = -\ln(P(Y_s = y_s | X_s = \omega_i)) \quad (6)$$

The single-time posterior probabilities are modeled as Gaussian mixtures using class statistics derived from the HMPM estimation on the irregular graph. The spatial U_{sp} and temporal U_{tp} energy functions can be expressed as:

$$U_{sp}(X_s = \omega_i, X_{sp}) = - \sum_{\omega_j \in \Omega_{sp}} \varphi_{sp} \delta(\omega_i, \omega_j) \left(\sum_{\omega_j \in X_{sp}} \delta(\omega_i, \omega_j) \frac{\text{card}(q \in V_{sp-sim})}{\text{card}(q \in V_{sp})} \right) \quad (7)$$

and

$$U_{tp}(X_s = \omega_i, X_{tp}) = - \sum_{\lambda_j \in \Lambda_{tp}} \varphi_{tp} P(\omega_i | \lambda_j) \left(\sum_{\lambda_i \in X_{tp}} \delta(\omega_i, \lambda_i) \frac{\text{card}(q \in V_{tp-sim})}{\text{card}(q \in V_{tp})} \right) \quad (8)$$

Index δ is the Kronecker delta function, which is, according to a pair-wise clique system (s - q) between center node s and a spatially or temporally adjacent object q (Figure 2(b)), equal to 1 if $\omega_i = \omega_j$ or $\omega_i = \lambda_i$, respectively, and zero otherwise. Due to the fact that, in contrast to lattice-based graphs, the number of neighbors in V_{sp} and V_{tp} varies on irregular planar graphs, the amount of the spatial and temporal energy may vary significantly in relation to the spectral term. To equalize the influence of the spectral and temporal terms in the ICM estimation over the whole planar graph, an n^{th} -order spatial neighborhood system V_{sp-sim} is simulated, so that for example a first-order system contains four elements q . The temporal neighborhood system V_{tp-sim} is identical to V_{sp-sim} . However, since it considers the central object, it contains one additional element (Figure 2(b)).

In order to account for the varying size of the objects in the irregular neighborhood system V_{tp} , the weighting factor φ_{tp} is integrated, considering the spatial proportion of the respective classes in V_{tp} :

$$\varphi_{tp} = (A(\lambda_i, X_{tp}) / A(V_{tp})) \quad (9)$$

In addition, the weighting of the spatial energy function by φ_{sp} accounts for the varying border length between object s and q in the irregular neighborhood system V_{sp} :

$$\varphi_{sp} = ((A(\omega_i, X_{sp}) / A(V_{sp})) + b_{\omega_i}) / 2 \quad \text{with } b_{\omega_i} = \sum_{q \in \omega_i} b(s, q) / b_s \quad (10)$$

where b_{ω_i} describes the ratio of the shared border length of objects labeled to class ω_i with an adjacent object q to the total border length b_s of s . The greater the size of an object q and the higher the common border to s , the more weight is given to this object at the computation of U_{sp} .

The same formulations of the MRF related to Equations (6–10) can be generated for image Y_{t_1} . The mutual approach couples the two MRFs of the bi-temporal data-set using the ICM algorithm. Starting from an initial labeling produced by the HMPM step, the preceding classification of one image is exploited to update the labeling of the other image at each iteration, and *vice versa*, until convergence. For an extension of this bi-directional approach to a sequence of more than two images, the reader is referred to [11].

Estimation of Temporal Transition Probabilities

The only term that considers correlation between data in (8) is $P(\omega_i | \lambda_i)$. It represents the transition probability from class λ_i at t_1 to class ω_i at t_2 . It is an element of the so-called transition probability matrix (TPM), which can be calibrated from expert's knowledge using ground truth or historic data [11] or estimated directly from the image data using for example the "compound classification rule" [43,44]. This method involves finding the optimal pair of classes (ω_i, λ_i) for each pair of image elements based on the Bayes rule for minimum error. In this work, the method of [44] is used, which replaces the TPM by a joint probability matrix (JPM), and is adapted to an irregular graph structure. The method uses an

iterative fixed-point EM (Expectation-Maximization) -like algorithm [45] for estimating the temporal correlation of multi-date images represented by joint class probabilities $P(\omega_i, \lambda_i)$. The elements of the related JPM of size $N \times M$ are computed recursively for k iterations until convergence is reached according to:

$$P_{k+1}(\omega_i, \lambda_i) = \frac{1}{P(\omega_i)P(\lambda_i)O} \sum_{s=1}^O \frac{P_k(\omega_i, \lambda_i)P(\omega_i|y_s)P(\lambda_i|y_q)\varphi_{jpm}}{\sum_{\omega_n \in \Omega} \sum_{\lambda_m \in \Lambda} \frac{P_k(\omega_n, \lambda_m)}{P_k(\omega_n)P_k(\lambda_m)} P(\omega_n|y_s)P(\lambda_m|y_q)} \quad (11)$$

$P_0(\omega_i, \lambda_i)$ is initialized by $(N \times M)^{-1}$ and O is the number of objects of the planar graph. The *a priori* probabilities $P(\omega_i)$ and $P(\lambda_i)$ are derived by computing the relative occurrence of each class according to the respective HMPM estimation. The factor $\varphi_{jpm} = A_s/A_{\text{card}(s)}$ considers the irregular nature of the planar graph by weighting the influence of each object according to its relative spatial extent in relation to the entire scene. The following normalization generates values of the JPM, summing up to 1:

$$P_{k+1}^{\text{norm}}(\omega_i, \lambda_i) = \frac{P_{k+1}(\omega_i, \lambda_i)}{\sum_{\omega_n \in \Omega} \sum_{\lambda_m \in \Lambda} P_{k+1}(\omega_n, \lambda_m)} \quad (12)$$

2.2.3. Hybrid Multi-Contextual Markov Model

The knowledge of marginal posteriors $P(x_s|y)$ allows to access the degree of confidence for each node s by computing the marginal posterior entropy E_s [28]:

$$E_s(x_s|y) = - \sum_{\omega_i \in \Omega} P(x_s = \omega_i|y) \log P(x_s = \omega_i|y) \quad (13)$$

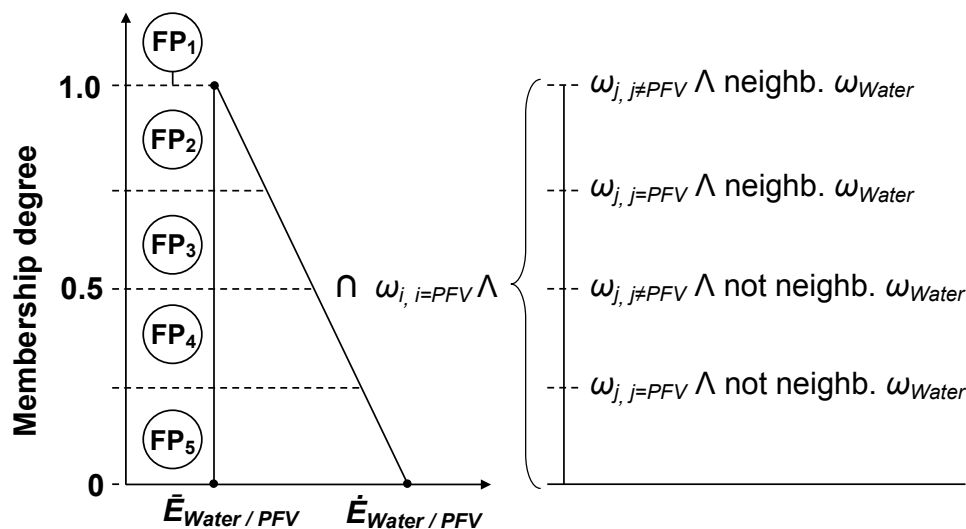
Based on this formulation, a confidence map can be computed for the whole graph. Higher entropy values are indicators of misclassifications of s [46]. These confidence maps are used for the combination of the hierarchical causal and the spatio-temporal noncausal Markov model by restricting the ICM algorithm presented in (4) to values of E_s greater than a defined threshold T_E . This decreases the computational effort since the spatio-temporal context is only integrated for the label estimation of a limited number of elements of the sub-area $S^1_{\text{sub-1}}$. After the first iteration, this number can be further reduced by restricting the ICM algorithm to objects $s \in S^1_{\text{sub-1}}$ with a common border to other elements greater T_E .

2.3. Generation of Flood Probability Maps

A quantification of uncertainty in the labeling of each image element can be valuable for flood disaster management and performance evaluation of hydrodynamic models. Recently, Schumann *et al.* [47] used inundation possibilities derived from multi-algorithm ensembles for calibrating flood models. In this work, entropy-based confidence maps are used created from the final labeling result of ω_{Water} and ω_{PFV} for the generation of a five-class flood possibility (FP) map. Fuzzy theory is used to transform the entropy values to fuzzy memberships in the interval $[0, \dots, 1]$ (Figure 3). Full weight (FP₁) is given to nodes $s \in \omega_{\text{Water}}$ and $s \in \omega_{\text{PFV}}$ with E_s lower than the mean entropy \bar{E}_{ω_i} of ω_{Water} and ω_{PFV} , respectively. Objects with entropies between \bar{E}_{ω_i} and the maximum entropy \hat{E}_{ω_i} are assigned to four different

possibility classes (FP₂₋₅) according to a linearly decreasing fuzzy membership function. The fuzzy set of ω_{PFV} is combined with additional membership values taking into account spatial as well as temporal relationships of $s \in \omega_{PFV}$ from the final classification; e.g. full weight is given to objects with $E_s \leq \bar{E}_{PFV}$, labeled to a different class at Δt and neighboring elements $s \in \omega_{Water}$. In contrast, elements without contact with other flood objects and exhibiting no class change over time are given a lower degree of membership, since these objects exhibit a reduced likelihood of being inundated (Figure 3).

Figure 3. Fuzzy sets for the generation of FP maps using MPM entropies and spatio-temporal labeling information.



3. Experimental Results

3.1. Data-set Description

In order to carry out an experimental analysis aimed at assessing the performance of the proposed approach for a real test case, a bi-temporal data-set consisting of two TerraSAR-X ScanSAR scenes with 8.25 m pixel spacing in range and azimuth direction is used (Figure 4(a,b)). The study area of this work is the Zambezi floodplain situated in the Caprivi Strip in north-eastern Namibia, which is regularly affected by flooding related to heavy seasonal rainfalls. Both images, which were acquired on April 11, 2009 and April 20, 2010, show large scale inundations with a higher flood level in 2009. Since both data-sets were acquired in an identical orbit with similar ordering options (HH-polarization, incidence angle range of 27.1°–36.6°), no major system-related differences are present.

In both data-sets, in comparison to the surrounding dry land, open water areas appear dark due to specular reflection of the incident radar signal. In contrast, flooded vegetation causes very distinct and bright signatures. Indeed, X-band SAR has a strongly reduced ability to detect inundation beneath dense vegetation such as forest due to increased canopy attenuation and volume scattering in comparison to the longer C-, and L-band signals (e.g., [48]). In this study area, however, the emergent vegetation is mainly composed of foliated shrubs and grassland, whose structure admits a multiple-bounce effect, in which the penetrated radar pulse is backscattered from the water surface and lower sections of the vegetation. This causes a high signal return [49]. For simplicity, most flood

mapping algorithms only consider open water areas. This, however, results in an underestimation of the flood extent if the flood plain is interspersed with emergent vegetation. Digital elevation models (DEMs) have been used effectively for detecting flooding beneath vegetation [35,50]. However, since the study area is characterized by a low topographic variability, and a high resolution DEM was not at our disposal within this study, no such information could be used to optimize classification results.

For validation purposes of the water extent in each SAR scene, two optical images from the RapidEye satellite of April 14, 2009 and April 22, 2010, with a spatial resolution of 5 m, were available. The time-offset relative to the SAR data was three days and two days, respectively. However, due to the stable flood conditions, no critical change in the flood extents was observable between the SAR and optical data-sets. For this reason, the RapidEye scenes were used to create a reference map for each date for a small sub-area (256×256 pixel) of the eastern part of Lake Liambezi by visual interpretation and manual digitalization of the open water and flooded vegetation areas. High resolution optical images of historic flood events were available in Google Earth for cross-checking the validation mask.

3.2. Results and Discussion

In this section, the effectiveness of the proposed multi-contextual hybrid Markov model is evaluated by investigating the influence of (1) using irregular graphs, (2) adapting the Markov models to these irregular structures, and (3) combining hierarchical causal with noncausal Markov modeling on irregular graphs. Additionally, the results of the HMPM and HMAP estimation are compared.

For this purpose, several classification results were generated for the chosen reference areas of Y_{t_1} and Y_{t_2} by applying different models to regular and irregular graphs (Table 2). R-T-ICM considers the pixel-based integration of only spatio-temporal information into the labeling process. The sole integration of hierarchical context is accomplished by R-HMAP and R-HMPM on a quadtree as well as by I-HMAP and I-HMPM on an irregular graph, without considering the weighting of the child objects in relation to their parent nodes. The non-weighted hybrid Markov model is represented by R-HMAP-ICM and R-HMPM-ICM on a quadtree as well as I-HMAP-ICM and I-HMPM-ICM on an irregular graph. In contrast, I-HMAP-ICM-w and I-HMPM-ICM-w consider the variable structure of hierarchical and spatio-temporal neighborhood systems of irregular graphs.

Identical threshold values of $\tau_1 = 50.7$ and $\tau_2 = 50.0$ for Y_{t_1} as well as $\tau_1 = 134.1$ and $\tau_2 = 163.2$ for Y_{t_2} derived by the automatic thresholding approach mentioned in Section 2.2.1 are used for the initialization of each model. The regularization parameters γ_{sp} and γ_{tp} are fixed to 1 during the experiment. A real (regular graph) and simulated (irregular graph) first-order neighborhood system is used in the noncausal Markov model, which is only applied to objects with an entropy value greater than the average entropy \bar{E} of Y_{t_1} and Y_{t_2} , respectively. The hierarchical model at times t_1 and t_2 is accomplished on graphs with eight levels. Therefore, on a quadtree, the smallest objects are defined on S^1 by 2×2 pixels. Accordingly, S^1 is partitioned into 16,384 nodes. Due to the fixed decrease of 25% of the object number between adjacent scales, the total number of nodes of the tree is 21,845. The irregular graphs are built with a relative object number of $\sim 50\%$ between S^{l+1} and S^l . The finest levels of Y_{t_1} and Y_{t_2} are partitioned into $\sim 2,000$ homogeneous segments. This results in a total object number

of the respective graphs of ~4,300. After synchronizing the segmentations of the two planar graphs, both levels S^1 are represented by ~12,000 nodes.

In order to assess the performance of the different classifiers, the “Overall Accuracy” (OA) measure is used, which is the percentage of correctly classified pixels in relation to the total number of pixels (Table 2).

The experimental results show a nearly identical mean OA of 79.5% for Y_{t_1} and 80.1% for Y_{t_2} , averaged over all algorithms (Table 2). The non-hierarchical R-T-ICM method provides OA similar to these average values and significantly outperforms the HMAP, HMPM and HMAP-ICM estimation on the quadtree as well as the HMAP-w estimation on the irregular graph. However, the R-T-ICM method is accompanied by a strong computational demand, since it is iteratively applied to every pixel in the images within six iterations until convergence is reached.

Table 2. Overall accuracy of different models according to graph structure chosen. Index “w” marks methods which consider a weighting in the classification according to the irregular nature of the graphs.

Time	Regular (R-)					Irregular (I-)						Mean
	Planar T-ICM	Quadtree Hierarch				ical						
		HMAP	HMPM	HMAP-ICM	HMPM-ICM	HMAP-w	HMPM-w	HMAP-ICM-w	HMPM-ICM-w	HMAP-ICM	HMPM-ICM	
t_1	79.90	77.08	78.50	77.62	80.30	77.80	79.67	80.39	82.97	78.63	81.78	79.5
t_2	79.77	73.80	76.97	78.11	81.04	76.23	80.86	82.48	86.33	80.07	85.20	80.1

It can clearly be seen that the results established with the HMPM estimates show higher OAs than methods that are related to the HMAP approach. The difference is ~1.4% to 2.7% for Y_{t_1} and more distinct for Y_{t_2} with values between ~2.6% and 5.1%. Among the two hierarchical estimators, the HMPM estimator is more time consuming due to the higher computational complexity in the top-down pass. However, it offers the possibility to compute confidence maps based on MPM entropies.

In comparison to the hierarchical modeling results, the OA is consistently higher when taking into account the bi-directional exchange of spatio-temporal information within the ICM algorithm. The increase in accuracy is in the range of ~1.0% to ~2.5% for Y_{t_1} and significantly higher for Y_{t_2} with values of 3.3% to 6.8%.

If one considers the graph structure in the multi-contextual hybrid Markov modeling result, it is notable that the non-weighted models I-HMAP-ICM and I-HMPM-ICM are more efficient for Y_{t_2} with OAs ~2.0% and ~4.2% higher than the quadtree-based models R-HMAP-ICM and R-HMPM-ICM. In contrast, for Y_{t_1} , the respective OAs are only increased by ~1.0% and ~1.5%. By adapting the hybrid models (I-HMAP-ICM-w and I-HMPM-ICM-w) to the irregular graph structures, a further increase in accuracy can be stated for both images compared to the non-weighted models I-HMAP-ICM and I-HMPM-ICM. Highest OAs of ~83.0% for Y_{t_1} and ~86.3% for Y_{t_2} are both related to the proposed method HMPM-ICM-w, which offers an accuracy increase of ~2.7% and ~5.3%, respectively, compared to the quadtree-based model R-HMPM-ICM. This can be explained by reduced

discrepancies in the labeling process using homogeneous irregular objects instead of quadratic segments, which are characterized by a higher probability to contain mixtures of different classes.

Additionally, in contrast to noncausal Markov modeling on a regular planar lattice, spatially larger neighborhood systems can be considered. This is associated with a fast convergence of the ICM algorithm within four iterations. Besides the increased accuracy, the computational demand of the hierarchical models on irregular graphs is reduced by a factor of about five in comparison to quadtrees due to the lower number of nodes (~4,000 vs. ~21,845). Likewise, the application of the ICM algorithm is characterized by less computational complexity on irregular planar graphs due to the reduced number of nodes at S^1 (~12,000 nodes) in comparison to the finest levels (16,384 nodes) of the quadtrees, despite the fact that additional weighting parameters must be computed.

When applied to the sub-area of Y_{t_1} and Y_{t_2} , the proposed multi-contextual Markov model takes 35 s of processing time on two irregular hierarchical graphs with eight levels and a total number of respectively ~4,300 nodes (CPU details: Intel Xeon 5460 Core Duo @ 3.16-GHz processor with a 3-GB RAM). The generation of the hierarchical graph and the HMPM estimation account for ~45%, the estimation of the temporal transition probabilities and the application of the ICM estimator require ~55% of this time. The execution of the proposed method on irregular hierarchical graphs is ~60% faster than on quadtrees with eight levels, even if the generation of the irregular graph is more time consuming and a weighting of the nodes must be taken into account.

The incorporation of contextual information has a smoothing effect on the final classification results, by screening out isolated segments of a certain class in homogeneous regions (Figure 4(c,d)). Errors mainly occur due to an underrepresentation of the open water area at the land-water boundaries. This is due to the coarser resolution of the ScanSAR data in contrast to the RapidEye reference data and the high sensibility of the radar signal to protruding cyperaceous vegetation at the river-banks, which prohibits the perceptibility of a distinct waterline. As is shown in Table 3, this effect is more pronounced at Y_{t_1} (UA: 78.9%) than at Y_{t_2} (UA: 93.2%), where smaller water areas are present. However, producer accuracy (PA) reaches more than 93% for both dates. Highest errors are related to the misclassification of image elements of class “PFV” to “No water”. These errors are mainly caused by flooded vegetation areas with a dense canopy, which prohibits multiple-bounce effects. This results in an attenuated signal return and an underestimation of the class “PFV”. This effect is more pronounced at t_2 with an UA of class “PFV” of ~50.0% which is ~20.0% lower compared to that at t_1 .

If one combines the classes “Water” and “PFV” to one single class “Flood”, the supplementary consideration of bright scatterers into the labeling process enhances flood mapping accuracy (UA) from 33.9% to 73.8% at t_1 and from 62.2% to 78.9% at t_2 . The large difference of the UA of class “Flood” between both dates results from the fact that the proportion of open water areas is significantly higher at t_2 due to a higher flood level. This causes a complete submersion of protruding vegetation areas which act as strong scatterers at t_1 . The main flood areas exhibit a high probability to be classified correctly according to the FP maps (Figure 4(e,f)). Smaller, more isolated open water areas are marked by a higher classification uncertainty given the HMPM estimation.

Presumably, the application of the proposed method to C- or L-band SAR data would result in a higher detectability of flooding beneath vegetation. However, as the contrast between open water and land areas is most distinct in X-band SAR data, a lower classification accuracy of the class “Water” may be expected using SAR systems of greater wavelength.

Figure 4. TerraSAR-X data-sets for Caprivi/Namibia (center coordinate: 17°56'44"S, 24°22'34"E) on (a) April 11, 2009 and (b) April 20, 2010; Classification results derived by using the IR-HMPM-ICM-w model (c, d); FP maps (e, f).

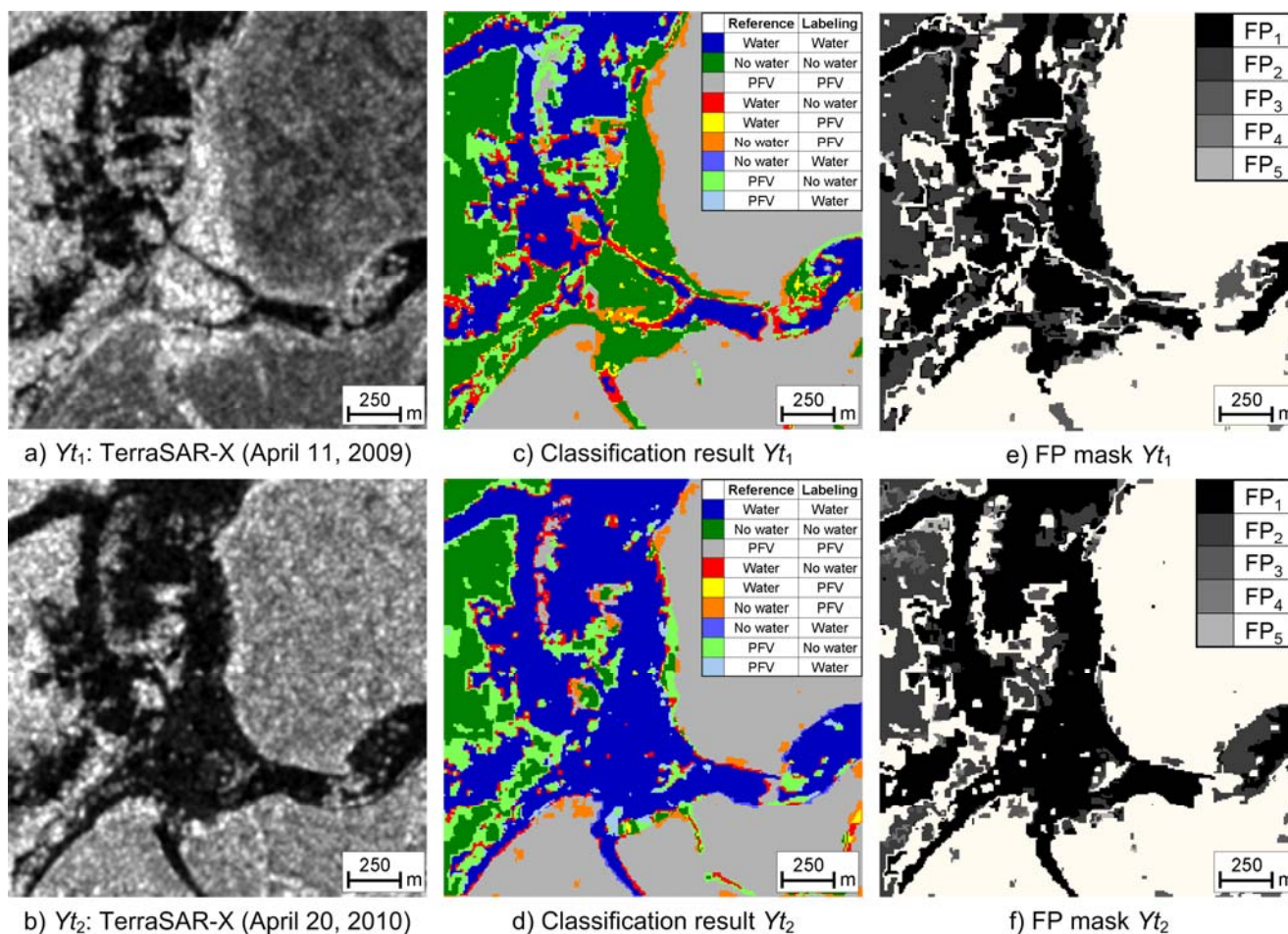


Table 3. Accuracy matrices for the labeling result of HMPM-ICM-w on an irregular graph at t_1 and t_2 (PA = Producer Accuracy, UA = User Accuracy).

Date	Classified	Reference				UA [%]
		Water No	water	PFV		
T1	Water	11129	2857	115	14101	78.92
	No water	541	30261	1895	32697	92.54
	PFV	236	5511	12991	18738	69.32
		11906	38629	15001	65536	
	PA [%]	93.47	78.33	86.60	OA [%]	82.97
					Khat [%]	71.69
T2	Water	21240	1486	61	22787	93.21
	No water	145	29673	1546	31364	94.61
	PFV	744	4976	5665	11385	49.67
		21610	38038	5888	65536	
	PA [%]	95.98	82.18	77.90	OA [%]	86.33
					Khat [%]	77.20

4. Conclusion

In this work, the problem of unsupervised flood detection in SAR data using a hybrid multi-contextual Markov image model on irregular hierarchical graphs is addressed. Experimental results obtained on a bi-temporal TerraSAR-X ScanSAR data-set for Caprivi/Namibia confirm the effectiveness of combining automatically initialized causal hierarchical with noncausal spatio-temporal Markov models with respect to accuracy and computational performance.

The incorporation of hierarchical context into the labeling process is accomplished by a hierarchical marginal posterior mode (HMPM) estimation using Markov chains in scale. The supplementary integration of spatio-temporal context is applied by an iterative bi-directional information exchange between elements of two consecutive planar graphs of a time sequence. This processing step is restricted to elements which offer a certain probability to be wrongly classified according to marginal posterior-based entropies.

It is shown that the application of this hybrid model on irregular graphs helps to reduce classification errors and computational demands in comparison to modeling on the regular graph structure of quadrees. The adaption of this model to the variable nature of irregular hierarchical and spatio-temporal neighborhood systems leads to a further increase in accuracy. Furthermore, it is demonstrated that HMPM estimation outperforms results generated by hierarchical maximum *a posteriori* (HMAP) estimation.

The incorporation of inundated bright scattering vegetation areas into the classification scheme results in a significant enhancement of flood mapping results. Entropy-based confidence maps combined with spatio-temporal relationships of potentially flooded vegetation to open water areas are used for the quantification of the uncertainty in the labeling of each image element in flood possibility masks.

For future work, additional information such as digital elevation models (DEMs) could be used to extend the fuzzy sets describing flood probabilities in areas with terrain of sufficient variability.

Acknowledgements

The major part of this work has been funded by the German Ministry of Education, Science, Research and Technology (BMBF) in the context of the Research Program “Risk Management of Extreme Flood Events” (RIMAX), project SAR-HQ (Grant Reference Number: 0330719). The authors would like to thank the two anonymous reviewers for their helpful comments.

References

1. Ormsby, J.P.; Blanchard, B.J.; Blanchard, A.J. Detection of lowland flooding using active microwave systems. *Photogramm. Eng. Remote Sens.* **1985**, *51*, 317-328.
2. Alsdorf, D.E.; Melack, J.M.; Dunne, T.; Mertes, L.A.K.; Hess, L.L.; Smith, L.C. Interferometric radar measurements of water level changes on the Amazon flood plain. *Nature* **2000**, *404*, 174-177.
3. Horrit, M.S.; Mason, D.C.; Cobby, D.M.; Davenport, I.J.; Bates, P. Waterline mapping in flooded vegetation from airborne SAR imagery. *Remote Sens. Environ.* **2003**, *85*, 271-281.

4. Lu, D.; Mausel, P.; Brindizio, E.; Moran, E. Change detection techniques. *Int. J. Remote Sens.* **2004**, *25*, 2365-2407.
5. Mas, J.F. Monitoring land-cover changes: A comparison of change detection techniques. *Int. J. Remote Sens.* **1999**, *20*, 139-152.
6. Bruzzone, L.; Prieto, D.F. Automatic analysis of the difference image for unsupervised change detection. *IEEE Trans. Geosci. Remote Sens.* **2000**, *38*, 1171-1182.
7. Martinis, S.; Twele, A.; Voigt, S. Unsupervised extraction of flood-induced backscatter changes in SAR data using Markov image modeling on irregular graphs. *IEEE Trans. Geosci. Remote Sens.* **2010**, *48*, Accepted.
8. Moser, G.; Serpico, S.B. Generalized minimum-error thresholding for unsupervised change detection from SAR amplitude imagery. *IEEE Trans. Geosci. Remote Sens.* **2006**, *44*, 2972-2982.
9. Bruzzone, L.; Prieto, D.F. An adaptive semiparametric and context-based approach to unsupervised change detection in multitemporal remote-sensing images. *IEEE Trans. Image Process.* **2002**, *11*, 452-466.
10. Singh, A. Digital change detection techniques using remotely-sensed data. *Int. J. Remote Sens.* **1989**, *10*, 989-1003.
11. Melgani, F.; Serpico, S.B. A Markov random field approach to spatio-temporal contextual image classification. *IEEE Trans. Geosci. Remote Sens.* **2003**, *41*, 2478-2487.
12. Feitosa, R.Q.; Costa, G.; Mota, G.L.A.; Pakzad, K.; Costa, C.O. Cascade multitemporal classification based on fuzzy Markov chains. *ISPRS J. Photogramm. Remote Sens.* **2009**, *64*, 159-170.
13. Geman, S.; Geman, D. Stochastic relaxation, Gibbs distributions and the Bayesian restoration of images. *IEEE Trans. Pattern Anal. Mach. Intell.* **1984**, *6*, 721-741.
14. Li, S.Z. *Markov Random Field Modeling in Image Analysis*, 3rd ed.; Springer-Verlag: London, UK, 2009.
15. Carincotte, C.; Derrode, S.; Bourennane, S. Unsupervised change detection on SAR images using fuzzy hidden Markov chains. *IEEE Trans. Geosci. Remote Sens.* **2006**, *44*, 432-441.
16. Benedek, C.; Szirányi, T. Change detection in optical aerial images by a multilayer conditional mixed Markov model. *IEEE Trans. Geosci. Remote Sens.* **2009**, *47*, 3416-3430.
17. Mota, G.L.A.; Feitosa, R.Q.; Coutinho, H.L.C.; Liedtke, C.E.; Müller, S.; Pakzad, K.; Meirelles, M.S.P. Multitemporal fuzzy classification model based on class transition possibilities. *ISPRS J. Photogramm. Remote Sens.* **2007**, *62*, 186-200.
18. Solberg, H.S.; Taxt, T.; Jain, A.K. A Markov random field model for classification of multisource satellite imagery. *IEEE Trans. Geosci. Remote Sens.* **1996**, *34*, 100-113.
19. Liu, D.; Song, K.; Townshend, J.; Gong, P. Using local transition probability models in Markov random fields for forest change detection. *Remote Sens. Environ.* **2008**, *112*, 2222-2231.
20. Smits, P.; Dellepiane, S. Synthetic aperture radar image segmentation by a detail preserving Markov random field approach. *IEEE Trans. Geosci. Remote Sens.* **1997**, *35*, 844-857.
21. Jackson, Q.; Landgrebe, D. Adaptive Bayesian contextual classification based on Markov random fields. *IEEE Trans. Geosci. Remote Sens.* **2002**, *40*, 2454-2463.
22. Kasetkasem, T.; Varshney, K.V. An image change detection algorithm based on Markov random field models. *Canad. J. Remote Sens.* **2002**, *40*, 1815-1823.

23. Fjørtoft, R.; Delignon, Y.; Pieczynski, W.; Sigelle, M.; Tupin, F. Unsupervised classification of radar images using hidden Markov chains and hidden Markov random fields. *IEEE Trans. Geosci. Remote Sens.* **2003**, *41*, 675-686.
24. Kasetkasem, T.; Arora, M.K.; Varshney, P.K. Super-resolution land cover mapping using a Markov random field based approach. *Remote Sens. Environ.* **2005**, *96*, 302-314.
25. Tso, B.; Olsen, R.C. Combining spectral and spatial information into hidden Markov models for unsupervised image classification. *Int. J. Remote Sens.* **2005**, *26*, 2113-2133.
26. Bouman, C.; Shapiro, M. A multiscale image model for Bayesian image segmentation. *IEEE Trans. Image Process.* **1994**, *3*, 162-177.
27. Laferté, J.M.; Pérez, P.; Heitz, F. Discrete Markov image modeling and inference on the quadtree. *IEEE Trans. Image Process.* **2000**, *9*, 390-404.
28. Pérez, P.; Chardin, A.; Laferté, J.M. Noniterative manipulation of discrete energy-based models for image analysis. *Pattern Recog.* **2000**, *33*, 573-586.
29. Cheng, H.; Bouman, C. Multiscale Bayesian segmentation using a trainable context model. *IEEE Trans. Image Process.* **2001**, *10*, 511-525.
30. Collet, C.; Murtagh, F. Multiband segmentation based on a hierarchical Markov model, *Pattern Recognit.* **2004**, *37*, 2337-2347.
31. Provost, J.-N.; Collet, C.; Rostaing, P.; Pérez, P.; Bouthemey, P. Hierarchical Markovian segmentation of multispectral images for the reconstruction of water depth maps. *Comput. Vis. Image Underst.* **2004**, *93*, 155-174.
32. Kato, Z.; Zerubia, J.; Berthod, M. A hierarchical Markov random field model and multi-temperature annealing for parallel image classification. *Graph. Models Image Process* **1996**, *58*, 18-37.
33. Katartzis, A.; Vanhamel, I.; Sahli, H. A hierarchical Markovian model for multiscale region-based classification of vector-valued images. *IEEE Trans. Geosci. Remote Sens.* **2005**, *43*, 548-558.
34. *eCognition Developer 8 User Guide*; Definiens AG: Munich, Germany, 2009.
35. Martinis, S.; Twele, A.; Voigt, S. Towards operational near real-time flood detection using a split-based automatic thresholding procedure on high resolution TerraSAR-X data. *Nat. Hazards. Earth Syst. Sci.* **2009**, *9*, 303-314.
36. Kittler, J.; Illingworth, J. Minimum error thresholding. *Pattern Recog.* **1986**, *19*, 41-47.
37. Bazi, Y.; Bruzzone, L.; Melgani, F. An unsupervised approach based on the generalized Gaussian model to automatic change detection in multitemporal SAR images. *IEEE Trans. Geosci. Remote Sens.* **2005**, *43*, 874-887.
38. Forney, G.D. The Viterbi algorithm. *IEEE Proc.* **1973**, *61*, 268-278.
39. Baum, L.; Petrie, T.; Soules, G.; Weiss, N. A maximization technique occurring in the statistical analysis of probabilistic functions of Markov chains. *IEEE Ann. Math. Stat.* **2005**, *41*, 164-171.
40. Swain, P.H. Bayesian classification in a time-varying environment. *IEEE Trans. Syst. Man Cybern.* **1978**, *8*, 879-833.
41. Besag, J. Spatial interaction and the statistical analysis of lattice systems. *J. R. Stat. Soc. Ser. B* **1974**, *36*, 192-236.
42. Besag, J. On the statistical analysis of dirty pictures. *J. R. Stat. Soc. Ser. B* **1986**, *48*, 259-302.

43. Bruzzone, L.; Serpico, S.B. An iterative technique for the detection of land-cover transitions in multispectral remote sensing images. *IEEE Trans. Geosci. Remote Sens.* **1997**, *35*, 858-867.
44. Bruzzone, L.; Prieto, D.F.; Serpico, S.B. A neural-statistical approach to multitemporal and multisource remote-sensing image classification. *IEEE Trans. Geosci. Remote Sens.* **1999**, *37*, 1350-1359.
45. Granville, V.; Rassin, J.P. Multivariate discriminant analysis and maximum penalized likelihood density estimation. *J. R. Stat. Soc. Ser. B* **1995**, *57*, 501-517.
46. Feng, X.; Williams, C.K.I.; Felderhof, S.N. Combining belief networks and neural networks for scene segmentation. *IEEE Trans. Pattern Anal. Mach. Intell.* **2002**, *24*, 467-483.
47. Schumann, G.; Baldassarre, G.D.; Paul, P.D. The utility of spaceborne radar to render flood inundation maps based on multialgorithm ensembles. *IEEE Trans. Geosci. Remote Sens.* **2009**, *47*, 2801-2807.
48. Richards, J.A.; Woodgate, P.W.; Skidmore, A.K. An explanation of enhanced radar backscattering from flooded forests. *Int. J. Remote Sens.* **1987**, *8*, 1093-1100.
49. Hong, S.-H.; Wdowinski, S.; Kim, S.-W. Evaluation of TerraSAR-X observations for wetland InSAR application. *IEEE Trans. Geosci. Remote Sens.* **2010**, *48*, 864-873.
50. Mason, D.C.; Horritt, M.S.; Dall'Amico, J.T.; Scott, T.R.; Bates, P.D. Improving river flood extent delineation from synthetic aperture radar using airborne laser altimetry. *IEEE Trans. Geosci. Remote Sens.* **2007**, *45*, 3932-3943.

© 2010 by the authors; licensee MDPI, Basel, Switzerland. This article is an open access article distributed under the terms and conditions of the Creative Commons Attribution license (<http://creativecommons.org/licenses/by/3.0/>).

6 Summary and outlook

Flood situations seem to become more frequent and destructive in many regions of the world. A rising awareness of the availability of satellite based cartographic information has led to an increase in requests to corresponding mapping services to support civil-protection and relief organizations with disaster-related mapping and analysis activities. Due to the rising number of satellite systems with high revisit frequencies, a strengthened pool of SAR data is available during operational flood mapping activities. This offers the possibility to observe the whole extent of even large-scale flood events and their spatio-temporal evolution, but also calls for automatic near real-time flood detection methods, which should drastically reduce the user input required by an active image interpreter.

The aim of this thesis was the development of methods for the near real-time derivation of detailed flood parameters from the new generation of high resolution X-band SAR satellite imagery. These data are, in comparison to data from conventional medium-resolution SAR sensors, characterized by an increased intra-class and decreased inter-class variability due to the reduced mixed pixel phenomenon. Assuming smooth to moderately roughened water surfaces contrasting with the surrounding land areas, hydrologic parameters such as flood extent, flood-related backscatter changes as well as flood probabilities are derived in a completely unsupervised way. For this purpose, automatically initialized multi-contextual models on irregular hierarchical graphs are used, which consider that semantic image information is less represented in single pixels but in homogeneous objects and their mutual relation.

In chapter 5.1, an automatic tile-based thresholding approach is developed, which solves the flood detection problem in large-size single-temporal SAR data with small *a priori* class probabilities in near real-time. Combining global and local scene statistics out of the entire SAR image, a small number of square tiles is automatically selected, which seem to be useful for the derivation of threshold positions between the pixel-populations of classes “Water” and “No water” due to clearly separated class distributions. Using tile-inherent information, parametric thresholding algorithms are adopted for the computation of the class-separating gray-level position which causes the minimum classification error according to the Gaussian distribution assumption. Mathematical combination techniques of (sub)histogram derived local thresholds as well as (sub)histogram merging strategies are applied for the calculation of one global threshold value. This method has been effectively extended in chapter 5.2 for thresholding of global histograms consisting of a mixture of three class

distributions by parameterization of local bi-modal class-conditional density functions with generalized Gaussian (GG) distributions. This parametric model is well adapted to approximate a large number of symmetric, leptokurtic and platycurtic distributions. It has been successfully used for deriving the thresholds between the classes “Positive change” and “Unchanged” as well “Unchanged” and “Negative change” in multi-temporal feature maps such as normalized change index (NCI) data (chapter 5.2) as well as for separating between “Water” and “No water” as well as “No water” and bright scattering “Potentially flooded vegetation” (chapter 5.3) in amplitude imagery.

The threshold values are used for the initialization of the class statistics of different contextual object-based classification algorithms: In chapter 5.1, an alternating multi-scale image decomposition and thresholding process is developed, which combines the advantages of three different hierarchical levels into the per-parcel classification scheme by restricting automatic flood detection of small- and medium-scale image objects to regions neighboring large-scale flood segments. This causes a compact core flood area with fine detailed flood objects at the land/water boundaries. In chapter 5.2 and 5.3, a hybrid Markov random field (MRF) model is developed on SAR images represented by irregular hierarchical graphs, which integrates scale-dependent as well as spatio- or spatio-temporal contextual information into the classification process in a time efficient manner.

Causal Markov model have the capacity to capture the intrinsic hierarchical nature of remote sensing data and to incorporate long range label relationships. Inference is obtained using hierarchical maximum *a posteriori* (HMAP) or hierarchical marginal posterior mode (HMPM) estimation. To avoid over- or under-segmentation of the SAR data, the graph structure is generated fully automatically by modeling the decomposition parameter of each segmentation level according to image content, sensor type and acquisition mode. The supplementary integration of spatio- or spatio-temporal context is accomplished by noncausal MRF modeling. To decrease the computational demand of the Iterated Conditional Modes (ICM) algorithm, the iterative energy minimization process is only applied to a restricted region of the finest level of the graph defined using HMAP- or HMPM-based confidence maps. The Markov models, originally developed for inference on regular graphs structures of quadrees and planar lattices, are adapted to the variable nature of irregular graphs, which are related to information-driven multi-scale image decomposition.

Experiments performed on TerraSAR-X StripMap data of Southwest England and ScanSAR data of north-eastern Namibia during large-scale flooding have revealed that per-parcel classification proves superior to pixel-based context-insensitive procedures. Further,

the incorporation of multi-contextual information and the modeling of the mutual relationships between networked homogeneous objects efficiently enhanced classification accuracy and reliability by screening out isolated segments of a certain class in homogeneous image regions while still preserving geometric details in the image.

It could be demonstrated that hierarchical causal Markov models are effective tools for modeling the hierarchical context of X-band SAR data for flood detection as well as change detection purposes. Even if the HMPM estimator is computationally more demanding than the HMAP estimator, it was found to be more suitable in terms of classification accuracy. Further, it offers the possibility to compute marginal posterior entropy-based confidence maps, which were used for the generation of flood possibility maps expressing the uncertainty in labeling of each image element. The supplementary integration of intra-spatial and, optionally, temporal contextual information into the Markov model resulted in a reduction of classification errors. As the monitoring frequency of flood situations can be intensified using the increasing number of highly revisiting SAR sensors in orbit, the incorporation of the temporal dimension by iteratively exchanging bi-directional information between elements of two consecutive planar graphs of a time sequence may gain in importance.

It was observed that the application of the hybrid multi-contextual Markov model on irregular graphs was able to reduce classification errors in comparison to modeling on regular graphs structures of quadtrees. This resulted from reduced discrepancies in the labeling process using homogenous irregular objects instead of quadratic segments, which are characterized by a higher probability to contain mixtures of different classes. Also the computational performance of the hybrid Markov model was higher on irregular graphs, as the number of nodes is significantly lower than on quadtrees.

An additional increase in classification accuracy could be achieved by adapting the formulation of the Markov models to the variable nature of irregular hierarchical and spatio-temporal neighborhood systems. Further, it was found that the graph structure and the chosen model parameters have a significant influence on the labeling result. An increasing number of levels in the graph enhanced classification accuracies and decreased the sensitivity of the remaining parameters such as mean relative object number of each graph level and the choice of the regularization parameters, which control the influence of the spatial and temporal context into the labeling process.

Generally, the obtained results confirm the effectiveness of the contextual approaches over smooth to moderately roughened open water areas within rural areas. A low land/water contrast caused by strongly roughened surface prohibits the automatic delineation of flood

zones. However, this effect mostly occurs on sea surfaces and large inland water bodies such as lakes and can be mitigated through data acquisitions in HH polarization.

In urban regions classification errors are amplified due to strong backscattering effects of anthropogenic structures and shadowing, layover and foreshortening effects on buildings. X-band SAR systems are generally not suited for detecting flooding under dense vegetation canopies such as forests due to the low capability of the X-band signal to penetrate into media. However, in chapter 5.3, the applicability of TerraSAR-X data for detecting flooding beneath shrubs and grasses in the Caprivi region of Namibia due to enhanced double bounce effects between the water surface and lower parts of the vegetation was demonstrated. Furthermore, in chapter 5.1, a method has successfully been developed which combines high resolution topographic information with multi-scale segmentation to enhance the mapping accuracy in areas consisting of flooded vegetation and anthropogenic objects as well as to remove non-water look-alike areas.

Even if results were satisfying, in future work it would be desirable to extend the presented automatic thresholding approach by a method which reacts more flexibly to the variable distribution of classes in heterogeneous multi-modal SAR image histograms using generalized mixture models. Within this context, El-Zaar & Ziou (2007) present the GGBL system, which uses four parametric distributions (Gaussian, Gamma, Beta, and Log-Normal) for modeling inhomogeneous SAR histograms consisting of separable modes that follow different statistical laws. Also the classification performance of the presented hybrid Markov approach, which models the conditional likelihoods at each node of the graph as Gaussian distribution, could possibly be improved by using more complex data models. However, as more parameter will have to be estimated for the parameterization of the class-conditional density functions, one has to trade off increasing classification accuracy against reduced computational performance.

In terms of flood detection, it would be an interesting topic to compare the developed hybrid Markov random field model with discriminated random fields (DRFs) (Kumar & Hebert 2003, Kumar 2005), which recently have become popular for classification tasks with the introduction of conditional random fields (CRFs) (Lafferty et al. 2001). Several authors report improvements of the CRFs over MRF-based generative models (e.g. Kumar and Hebert 2003, He et al. 2004, Yuan et al. 2007). Generally, MRFs are used in a probabilistic generative framework modeling the joint probability of the SAR data and its corresponding labels using Bayes rule (Geman & Geman 1984, Li 2009). On the contrary, the discriminative approach offers the capability to model the posterior distribution directly as a MRF without

estimating the prior and likelihood individually (Yuan et al. 2007, Li 2009). DRFs allow capturing arbitrary dependencies in the observed data without resorting to any model approximations. This is enabled by relaxing the restrictive assumption of conditional independence of the observed data typically used in the MRF framework for computational tractability (Kumar & Hebert 2003), which forces simplifying assumptions to get a factorized form of the likelihood model (Kumar 2005). Additionally, the interaction potentials in DRFs can be a function of labels and observations, while in the generative framework the prior term is only based on labels (Yuan et al. 2007, Li 2009). According to these advantages, DRFs appear promising tools for rapid mapping purposes.

Since most of the casualties and economic losses during inundations occur within urban areas, flood mapping within these areas is of high importance. However, just a few studies tackled the topic of SAR-based flood detection in urban areas due to the complexity of radar geometry and scattering mechanisms within these regions. Recently, Mason et al. (2010) proposed a supervised method to perform flood mapping in the town of Tewkesbury, UK, combining TerraSAR-X StripMap data with a high resolution digital surface model. In future, methods would be desirable which automatize this approach. The application of repeat-pass SAR Interferometry (InSAR) could become an effective tool to support flood detection in urban areas, since interferometric phase differences over water areas, which maintain coherence due to double bounce scattering between water surfaces and buildings, may be used to derive water-level changes from multi-temporal data.

At the end of 2010, single-pass interferometry will be possible through the TanDEM-X mission. The short-baseline interferometric measurements will enable the generation of detailed coherence maps, which will be useful for flood mapping activities as in comparison to repeat-pass interferometry, non-water areas will offer higher coherence due to lower temporal decorrelation. Therefore, it would be an interesting research topic to adapt the proposed hybrid Markov model to the automatic multi-contextual analysis of coherence maps.

Using X-band SAR, monitoring of flooding beneath vegetation is limited to short vegetation such as shrubs and grasses. Future L-band SAR missions such as TanDEM-L will have high potential for the derivation of flooding beneath forest canopies with high spatial resolution.

Continuing improvements in spatial, spectral, radiometric and temporal resolution can be expected for future remote sensing systems. However, there is still need to improve and update existing methodologies to extract the relevant physical parameters required for operational rapid mapping activities in terms of disaster and crisis-management support.

References

- Ahtonen, P., Euro, M., Hallikainen, M., Solbø, S., Johansen, B. & Solheim, I., 2004: SAR and optical based algorithms for estimation of water bodies. – Technical Report, FloodMan Project, Helsinki University of Technology, Helsinki, Finland.
- Alsdorf, D. E., Melack, J. M., Dunne, T., Mertes, L. A. K., Hess, L. L. & Smith, L. C., 2000: Interferometric radar measurements of water level changes on the Amazon flood plain. – *Nature*, 404: 174–177.
- Anys, H., Bannari, A., He, D. C. & Morin, D., 1994: Texture analysis for the mapping of urban areas using airborne MEIS-iii images. – Proceedings of the 1st International Remote Sensing Conference and Exhibition, Strasbourg, France, 231–245.
- Aronica, G., Bates, P. D. & Horritt, M. S., 2002: Assessing the uncertainty in distributed model predictions using observed binary pattern information within GLUE. – *Hydrological Processes*, 16: 2001–2016.
- Besag, J., 1986: On the statistical analysis of dirty pictures. – *Journal of the Royal Statistical Society: Series B*, 48: 259–302.
- Baatz, M. & Schäpe, A., 1999: Object-oriented and multi-scale image analysis in semantic networks. – Proceedings of the 2nd International Symposium on Operationalization of Remote Sensing, Enschede, Netherlands.
- Bamler, R. & Schättler, B., 1993: SAR data acquisition and image formation. – In Schreier, G. (ed.): *SAR geocoding: Data and Systems*, Wichmann-Verlag, Karlsruhe, Germany.
- Bates, P. D. & Anderson, M. G., 1995: Issues of hydraulic model validation and design using remotely sensed data. – Proceedings of the 1st ERS Thematic Working Group Meeting on Flood Monitoring, ESA/ESRIN, Frascati, Italy.
- Bates, P. D., Horritt, M. S., Smith, C. N. & Mason, D. C., 1997: Integrating remote sensing observations of flood hydrology and hydraulic modelling. – *Hydrological Processes*, 11 (14): 1777–1795.
- Baum, L., Petrie, T., Soules, G. & Weiss, N., 1970: A maximization technique occurring in the statistical analysis of probabilistic functions of Markov chains. – *Annals of Mathematical Statistics*, 41 (1): 164–171.
- Bazi, Y., Bruzzone, L. & Melgani, F., 2005: An unsupervised approach based on the generalized Gaussian model to automatic change detection in multitemporal SAR images. – *IEEE Transactions on Geoscience and Remote*, 43 (4): 874–887.
- Bazi, Y., Bruzzone, L. & Melgani, F., 2007: Image thresholding based on the EM algorithm and the generalized Gaussian distribution. – *Pattern Recognition*, 40 (2): 619–634.
- Berz, G., 2001: Climatic change: Effects on and possible responses by the insurance industry. – In Lozán, J. L., Graßl, H. & Hupfer, P. (eds.): *Climate of the 21st Century: Changes and risks* – Office of Wissenschaftliche Auswertungen, Hamburg, Germany, 392–399.
- Benedek, C. & Szirányi, T., 2009: Change detection in optical aerial images by a multilayer conditional mixed Markov model. – *IEEE Transactions on Geoscience and Remote*, 47 (10): 3416–3430.
- Benz, U., Hofmann, P., Wilhauck, G., Lingenfelder, I. & Heynen, M., 2004: Multi-resolution, object-oriented fuzzy analysis of remote sensing data for GIS-ready information. – *ISPRS Journal of Photogrammetry and Remote Sensing*, 58 (3/4): 239–258.
- Besag, J., 1974: Spatial Interaction and the Statistical Analysis of Lattice Systems. – *Journal of the Royal Statistical Society: Series B*, 36 (2): 192–236.
- Besag, J., 1986: On the statistical analysis of dirty pictures. – *Journal of the Royal Statistical Society: Series B*, 48 (3): 259–302.

- Blaschke, T. & Strobl, J., 2001: What's wrong with pixels? Some recent developments interfacing remote sensing and GIS. – *GIS - Zeitschrift für Geoinformationssysteme*, 6: 12–17.
- Blasco F., Bellan, M. F. & Chaudury, M. U., 1992: Estimating the extent of floods in Bangladesh using SPOT data. – *Remote Sensing of Environment*, 39: 167–178.
- Bouman, C. & Shapiro, M., 1994: A multiscale image model for Bayesian image segmentation. – *IEEE Transactions on Image Processing*, 3 (2): 162–177.
- Bourgeau-Chavez, L. L., Kasischke, E. S., Brunzell, S. M., Mudd, J. P., Smith, K. B. & Frick, A. L., 2001: Analysis of space-borne SAR data for wetland mapping in Virginia riparian ecosystems. – *International Journal of Remote Sensing*, 22 (18): 3665–3687.
- Bovolo, F. & Bruzzone, L., 2007: A split-based approach to unsupervised change detection in large-size multitemporal images: Application to tsunami-damage assessment. – *IEEE Transactions on Geoscience and Remote Sensing*, 45 (8): 1658–1669.
- Brakenridge, G. R. & Anderson, E., 2005: MODIS-based flood detection, mapping, and measurement: the potential for operational hydrological applications. – *Proceedings of the NATO Advanced Research Workshop, Baile Felix – Oradea, Romania*.
- Brázdil, R., Kotyza, O. & Dobrovolný, P., 2006: July 1432 and August 2002—two millennial floods in Bohemia? – *Hydrological Sciences Journal*, 51 (5): 848–863.
- Brivio, P. A., Colombo, R., Maggi, M. & Tomasoni, R., 2002: Integration of remote sensing data and GIS for accurate mapping of flooded areas. – *International Journal of Remote Sensing*, 23 (3): 429–441.
- Bruzzone, L. & Carlin, L., 2006: A multilevel context-based system for classification of very high spatial resolution images. – *IEEE Transactions on Geoscience and Remote Sensing*, 44 (9): 2587–2600.
- Bruzzone, L. & Prieto, D. F., 2000: Automatic analysis of the difference image for unsupervised change detection. – *IEEE Transactions on Geoscience and Remote Sensing*, 38 (3): 1171–1182.
- Bruzzone, L. & Prieto, D. F., 2002: An adaptive semiparametric and context-based approach to unsupervised change detection in multitemporal remote-sensing images. – *IEEE Transactions on Geoscience and Remote Sensing*, 11 (4): 452–466.
- Bruzzone, L., Prieto, D. F. & Serpico, S. B., 1999. A neural-statistical approach to multitemporal and multisource remote-sensing image classification. – *IEEE Transactions on Geoscience and Remote Sensing*, 37 (3): 1350–1359.
- Bruzzone, L. & Serpico, S. B., 1997: An iterative technique for the detection of land-cover transitions in multispectral remote sensing images. – *IEEE Transactions on Geoscience and Remote Sensing*, 35 (4): 858–867.
- Buck, C. H. & Monni, S., 2000: Application of SAR interferometry to flood damage assessment. – *Proceedings of the Committee on Earth Observation Satellites SAR Workshop, Toulouse, France, SP-450*.
- Carincotte, C., Derrode, S. & Bourennane, S., 2006: Unsupervised change detection on SAR images using fuzzy hidden Markov chains. – *IEEE Transactions on Geoscience and Remote Sensing*, 44 (2): 432–441.
- Carleer, A. P., Debeir, O. & Wolff, E., 2005: Assessment of very high spatial resolution satellite image segmentations. – *Photogrammetric Engineering & Remote Sensing*, 71, (11): 1285–1294.
- Chen, P., Liew, S. C. & Lim, H., 1999: Flood detection using multitemporal RADARSAT and ERS SAR data. – *Proceedings of the 20th Asian Conference of Remote Sensing, Hong Kong, China, 1185–1189*.

- Cheng, H. & Bouman, C., 2001: Multiscale Bayesian segmentation using a trainable context model. – *IEEE Transactions on Image Processing*, 10 (4): 511–525.
- Christensen, O. B. & Christensen, J. H., 2003: Severe summertime flooding in Europe. – *Nature*, 421: 805–806.
- Clark, L. A. & Pregibon, D., 1993: Tree-based models. – In Chambers, J. M. & Hastie, T. J. (eds.): *Statistical Models in S*, Chapman and Hall, New York, USA.
- Collet, C. & Murtagh, F., 2004: Multiband segmentation based on a hierarchical Markov model. – *Pattern Recognition*, 37 (12): 2337–2347.
- Costa, M. P. F., 2004: Use of SAR satellites for mapping zonation of vegetation communities in the Amazon floodplain. – *International Journal of Remote Sensing*, 25 (10): 1817–1835.
- Cyberski, J., Grześ, M., Gutry-Korycka, M., Nachlik, E. & Kundzewicz, Z., 2006: History of floods on the River Vistula. – *Hydrological Sciences Journal*, 51 (5): 799–817.
- Danklmayer, A., Döring, B. J., Schwerdt, M. & Chandra, M., 2009: Assessment of atmospheric propagation effects in SAR images. – *IEEE Transactions on Geoscience and Remote Sensing*, 47 (10): 3507–3518.
- Deer, P., 1998: Digital change detection in remotely sensed imagery using fuzzy set theory. – PhD thesis, University of Adelaide, Adelaide, USA.
- Definiens AG, 2008: *Definiens Developer 7 User Guide*, Munich, Germany.
- Definiens AG, 2009: *eCognition Developer 8 User Guide*, Munich, Germany.
- Dellepiane, S., Monni, S., Bo G. & Buck, C., 2000: SAR images and interferometric coherence for flood monitoring. – *Proceedings of the IEEE Geoscience and Remote Sensing Symposium*, Honolulu, Hawaii, USA, 2608–2610.
- De Moel, H., Van Alphen, J. & Aerts, J. C. J. H., 2009: Flood maps in Europe, methods, availability and use. – *Natural Hazards and Earth System Sciences*, 9: 289–301.
- Derrode, S., Mercier, G. & Pieczynski, W., 2003: Unsupervised change detection in SAR images using a multicomponent HMC model. – *2nd International Workshop on the Analysis of Multi-temporal Remote Sensing Images*, Ispra, Italy, 195–203.
- De Roo, A., Van der Knijff, J., Horritt, M. S., Schmuck, G., De Jong, S., 1999: Assessing flood damages of the 1997 Oder flood and the 1995 Meuse flood. – *Proceedings of the 2nd International Symposium on Operationalisation of Remote Sensing*, Enschede, The Netherlands.
- Drake, B. & Patton, K., 1980: Land use/cover mapping from SEASAT-A radar of the greater part of the Delmarva Peninsula, USA. – *Proceedings of the 14th International Symposium on Remote Sensing of Environment*, Environmental Research Institute of Michigan, Ann Arbor, USA, 1565–1575.
- Drake, B. & Shuchman, R. A., 1974: Feasibility of using multiplexed SLAR imagery for water resources management and mapping vegetation communities. – *Proceedings of the 9th International Symposium on Remote Sensing of Environment*, Environmental Research Institute of Michigan, Ann Arbor, USA, 714–724.
- Dubes, R. C. & Jain, A. K., 1989: Random field models in image analysis. – *Journal of Applied Statistics*, 16 (2): 131–164.
- EC, 2007: Directive 2007/60/EC of the European parliament and of the council of 23 October 2007 on the assessment and management of flood risks. Available at: <http://eur-lex.europa.eu/LexUriServ/LexUriServ.do?uri=OJ:L:2007:288:0027:0034:EN:PDF>, accessed July 26, 2010.
- EEA (European Environment Agency), 2008: *River floods - Assessment* published September 2008.

- Elachi, C., 1987: Introduction to the physics and techniques of remote sensing. – John Wiley & Sons, New York, USA.
- Elachi, C., 1988: Spaceborne Radar Remote Sensing: Applications and Technology. – IEEE Press, New York, USA.
- El-Zaart, A. & Ziou, D., 2007: Statistical modeling of multimodal SAR images. – *International Journal of Remote Sensing*, 28 (10): 2277–2294.
- EM-DAT, 2010: The OFDA/CRED international disaster database, Université catholique de Louvain, Brussels, Belgium. Available at: <http://www.emdat.be>, accessed July 07, 2010.
- Evans, D. C, Farr, T. G., Forf, J. P., Thompson, T. W. & Werner, C. L., 1986: Multipolarization radar images for geologic mapping and vegetation discrimination. – *IEEE Transactions on Geoscience and Remote Sensing*, 24 (2): 246–257.
- Feitosa, R. Q., Costa, G., Mota, G. L. A., Pakzad, K. & Costa, C. O, 2009: Cascade multitemporal classification based on fuzzy Markov chains. – *ISPRS Journal of Photogrammetry and Remote Sensing*, 64 (2): 159–170.
- Feng, X., Williams, C. K. I. & Felderhof, S. N., 2002: Combining belief networks and neural networks for scene segmentation. – *IEEE Transactions on Pattern Analysis and Machine Intelligence*, 24 (4): 467–483.
- Ferreira, J. P. G. & Bioucas-Dias, J. M., 2008: Bayesian land and sea segmentation of SAR imagery. – *Proceedings of the 3rd TerraSAR-X Science Team Meeting*, Oberpfaffenhofen, Germany.
- Fjørtoft, R., Delignon, Y., Pieczynski, W., Sigelle, M. & Tupin, F., 2003: Unsupervised classification of radar images using hidden Markov chains and hidden Markov random fields. – *IEEE Transactions on Geoscience and Remote Sensing*, 41 (3): 675–686.
- Forney, G. D., 1973: The Viterbi algorithm. – *Proceedings of the IEEE*, 61 (3): 268–278.
- Foster, J. L. & Hall, D. K., 1981: Multisensor analysis of hydrologic features with emphasis on the Seasat SAR. – *Photogrammetric Engineering and Remote Sensing*, 47 (5): 655–664.
- Fritz, T. & Eineder, M., 2009: TerraSAR-X ground segment: Basic product specification document. – TX-GS-DD-3302, 1.6.
- Geman, S. & Geman, S., 1984: Stochastic relaxation, Gibbs distributions and the Bayesian restoration of images. – *IEEE Transactions on Pattern Analysis and Machine Intelligence*, 6: 721–741.
- Giacomelli, A., Mancini, M. & Rosso, R., 1995: Assessment of flooded areas from ERS-1 PRI data: An application to the 1994 flood in Northern Italy. – *Physics and Chemistry of the Earth*, 20 (5-6): 469–474.
- Giordana, N. & Pieczynski, W., 1997: Estimation of generalized multisensor hidden Markov chains and unsupervised image segmentation. – *IEEE Transactions on Pattern Analysis and Machine Intelligence*, 19 (5): 465–475.
- Granville, V. & Rassin, J. P., 1995: Multivariate discriminant analysis and maximum penalized likelihood density estimation. – *Journal of the Royal Statistical Society: Series B*, 57 (3): 501–517.
- Haralick, R. M. & Sharipo, L. G, 1985: Image segmentation techniques. – *Computer Vision Graphics and Image Processing*, 29 (1): 100–132.
- Haykin, S., 1999: *Neural Networks: A Comprehensive Foundation*. – Prentice Hall, New Jersey, USA.
- He, X., Zemel, R. S. & Carreira-Perpiñán, M. Á., 2004: Multiscale conditional random fields for image labeling. – *IEEE Computer Society Conference on Computer Vision and Pattern Recognition*, Washington D.C., USA, 695–702.

- Henderson, F. M., 1987: Consistency of open surface detection with L-band SEASAT SAR imagery and confusion with other hydrologic features. – Proceedings of the 13th Annual Conference of Remote Sensing Society (Advances in Digital Image Processing), University of Nottingham, UK, 69–78.
- Henderson, F. M., 1995: Environmental factors and the detection of open surface water using X-band radar imagery. – *International Journal of Remote Sensing*, 16 (13): 2423–2437.
- Henry, J. B., Chastanet, P., Fellah, K. & Desnos, Y. L., 2006: ENVISAT multi-polarised ASAR data for flood mapping. – *International Journal of Remote Sensing*, 27 (10): 1921–1929.
- Heremans, R., Willekens, A., Borghys, D., Verbeeck, B., Valckenborg, J., Acheroy, M. & Perneel, C., 2003: Automatic detection of flooded areas on ENVISAT/ASAR images using an object-oriented classification technique and an active contour algorithm. – Proceedings of the IEEE Conference on Recent Advances in Space Technologies, Istanbul, Turkey, 289–294.
- Herrera-Cruz, V. & Koudogbo, F., 2009: TerraSAR-X Rapid mapping for flood events. – Proceedings of the International Society for Photogrammetry and Remote Sensing (Earth Imaging for Geospatial Information), Hannover, Germany, 170–175.
- Hess, L. L., Melack, J. M. & Simonett, D. S., 1990: Radar detection of flooding beneath the forest canopy: a review. – *International Journal of Remote Sensing*, 11 (7): 1313–1325.
- Hess, L. L. & Melack, J. M., 1994: Mapping wetland hydrology and vegetation with synthetic aperture radar. – *International Journal of Ecology and Environmental Sciences*, 20: 197–205.
- Hess, L. L. & Melack J. M., 2003: Remote sensing of vegetation and flooding on Magela Creek floodplain (Northern Territory, Australia) with the SIR-C synthetic aperture radar. – *Hydrobiologia*, 500: 65–82.
- Hess, L. L., Melack, J. M., Filoso, S. & Wang, Y., 1995: Delineation of inundated area and vegetation along the Amazon floodplain with the SIR-C synthetic aperture radar. – *IEEE Transactions on Geoscience and Remote Sensing*, 33 (4): 896–904.
- Hess, L. L., Melack, J. M., Novo, E. M. L. M., Barbosa, C. C. F. & Gastil, M., 2003: Dual-season mapping of wetland inundation and vegetation for the central Amazon basin. – *Remote Sensing of Environment*, 87: 404–428.
- Hong, S.-H., Wdowinski, S. & Kim, S.-W, 2010: Evaluation of TerraSAR-X observations for wetland InSAR application. – *IEEE Transactions on Geoscience and Remote Sensing*, 48 (2): 864–873.
- Horritt, M., 1999: A statistical active contour model for SAR image segmentation. – *Image and Vision Computing*, 17 (3/4): 213–224.
- Horritt, M. S., 2000: Calibration of a two-dimensional finite element flood flow model using satellite radar imagery. – *Water Resources Research*, 36 (11): 3279–3291.
- Horritt, M. S., Mason, D. C., Luckman, A. J., 2001: Flood boundary delineation from synthetic aperture radar imagery using a statistical active contour model. – *International Journal of Remote Sensing*, 22 (13): 2489–2507.
- Horritt, M. S., Mason, D. C., Cobby, D. M., Davenport, I. J. & Bates, P., 2003: Waterline mapping in flooded vegetation from airborne SAR imagery. – *Remote Sensing of Environment*, 85: 271–281.
- Horritt, M. S., 2006: A methodology for the validation of uncertain flood inundation models. – *Journal of Hydrology*, 326 (1–4): 153–165.
- Hostache, R., Matgen, P., Schumann, G., Puech, C. Hoffmann, L. & Pfister, L., 2009: Water level estimation and reduction of hydraulic model calibration uncertainties using

- satellite SAR images of floods. – *IEEE Transactions on Geoscience and Remote Sensing*, 47 (2): 431–441.
- Hunter, N. M., Bates, P. D., Horritt, M. S., De Roo, P. J. & Werner, M., 2005: Utility of different data types for flood inundation models within a GLUE framework. – *Hydrology and Earth System Sciences*, 9: 412–430.
- Imhoff, M., Story, M., Vermillion, C., Khan, F. & Polcyn, F., 1986: Forest canopy characterization and vegetation penetration assessment with space-borne radar. – *IEEE Transactions on Geoscience and Remote Sensing*, 24 (4): 535–542.
- IPCC, 2001: Human Settlements, Energy, and Industry. – In McCarthy, J. J., Canziani, O. F., Leary, N. A., Dokken, D. J. & White K. S. (eds.): *Climate Change 2001: Impacts, adaptation and vulnerability. Contribution of Working Group II to the Third Assessment Report of the Intergovernmental Panel on Climate Change*. – Cambridge University Press, Cambridge, UK, 384–416.
- IPCC, 2007a: Freshwater resources and their management. – In Parry, M. L., Canziani, O. F., Palutikof, J. P., van der Linden, P. J. & Hanson, C. E. (eds.): *Climate change 2007: Impacts, adaptation and vulnerability. Contribution of Working Group II to the Fourth Assessment Report of the Intergovernmental Panel on Climate Change*. – Cambridge University Press, Cambridge, UK, 173–210.
- IPCC, 2007b: Summary for policymakers. – In Parry, M. L., Canziani, O. F., Palutikof, J. P., van der Linden, P. J. & Hanson, C. E. (eds.): *Climate change 2007: Impacts, adaptation and vulnerability. Contribution of Working Group II to the Fourth Assessment Report of the Intergovernmental Panel on Climate Change*. – Cambridge University Press, Cambridge, UK, 7–22.
- Irving, P., Fieguth & Willsky, A., 1997: An overlapping tree approach to multiscale stochastic modeling and estimation. – *IEEE Transactions on Image Processing*, 6 (1): 1517–1529.
- Ivins, J. & Porill, J., 1995: Active region models for segmenting textures and colours. – *Image and Vision Computing*, 13 (5): 431–438.
- Jackson, Q. & Landgrebe, D., 2002: Adaptive Bayesian contextual classification based on Markov random fields. – *IEEE Transactions on Image Processing*, 40 (11): 2454–2463.
- Kasetkasem, T., Arora, M. K. & Varshney, P. K., 2005: Super-resolution land cover mapping using a Markov random field based approach. – *Remote Sensing of Environment*, 96: 302–314.
- Kasetkasem, T. & Varshney, K. V, 2002: An image change detection algorithm based on Markov random field models. – *Canadian Journal of Remote Sensing*, 40: 1815–1823.
- Kasischke, E. S. & Bourgeau-Chavez, L. L. (1997): Monitoring south Florida wetlands using ERS-1 SAR imagery. – *Photogrammetric Engineering and Remote Sensing*, 33: 281–291.
- Kasischke, E. S., Melack, J. M. & Dobson, M. C., 1997: The use of imaging radars for ecological applications - a review. – *Remote Sensing of Environment*, 59: 141–156.
- Kass, M., Witkin, A. & Terzopoulos, D., 1988: Snakes: Active contour models. – *International Journal of Computer Vision*, 1 (4): 321–331.
- Katartzis, A., Vanhamel, I. & Sahli, H., 2005: A hierarchical Markovian model for multiscale region-based classification of vector-valued images. – *IEEE Transactions on Geoscience and Remote Sensing*, 43 (3): 548–558.
- Kato, Z., Zerubia, J. & Berthod, M., 1996: A hierarchical Markov random field model and multi-temperature annealing for parallel image classification. – *Graphical Models and Image Processing*, 58 (1): 18–37.
- Kittler, J. & Illingworth, J., 1986: Minimum error thresholding. – *Pattern Recognition*, 19 (1): 41–47.

- Klausing, H. & Holpp, W. (eds.), 2000: Radar mit realer und synthetischer Apertur: Konzeption und Realisierung. – Oldenbourg Verlag München, Wien, Austria.
- Kohonen, T., 1995: Self-organizing maps. – Third edition, Springer-Verlag, Heidelberg, Germany.
- Kolmogorov, V. & Zabih, R., 2004: What energy functions can be Minimized via graph cuts? – *IEEE Transactions on Pattern Analysis and Machine Intelligence*, 26 (2): 147–159.
- Kussul, N., 2008: Intelligent computations for flood monitoring. – 14th International Conference of Knowledge-Dialogue-Solution, Varna, Bulgaria, 48–54.
- Kumar, S. & Hebert, M., 2003: Discriminative random fields: A discriminative framework for contextual interaction in classification. – *Proceedings of the IEEE International Conference on Computer Vision*, Nice, France, 1150–1159.
- Kumar, S., 2005: Models for learning spatial interactions in natural images for context-based classification. – PhD thesis, Carnegie Mellon University, Pittsburgh, USA.
- Kundzewicz, Z. W. & Schellnhuber, H.-J., 2004: Floods in the IPCC TAR perspective. – *Natural Hazards*, 31: 111–128.
- Kundzewicz, Z. W., Graczyk, D., Maurer, T., Pinskiwar, I., Radziejewski, M., Svensson, C. & Szwed, M., 2005: Trend detection in river flow series: 1. Annual maximum flow. – *Hydrological Sciences Journal*, 50 (5): 797–810.
- Kundzewicz, Z. W., 2008: Flood risk and vulnerability in the changing climate. – *Annals of Warsaw University of Life Sciences – SGGW, Land Reclamation*, 39: 21–30.
- Laferté, J. M., Pérez, P. & Heitz, F., 2000: Discrete Markov image modeling and inference on the quadtree. – *IEEE Transactions on Image Processing*, 9 (3): 390–404.
- Lang, M. W., Townsend, P. A. & Kasischke, E. S., 2008: Influence of incidence angle on detecting flooded forests using C-HH synthetic aperture radar data. – *Remote Sensing of Environment*, 112: 3898–3907.
- Lafferty, J., McCallum, A. & Pereira, F., 2001: Conditional random fields: Probabilistic models for segmenting and labeling sequence data. – *Proceedings of the 18th International Conference on Machine Learning*, Williams College, Massachusetts, USA, 282–289.
- Leberl, F., 1990: Radargrammetric image processing. – Artech House, Boston, USA.
- Leckie, D. G., 1998: Forestry applications using imaging radar. – In Henderson, F. M. & Lewis, A. J. (eds.): *Manual of remote sensing: Principles and applications of imaging radar*. – Third edition, John Wiley & Sons, New York, USA.
- Lewis, A. J., 1998: Geomorphic and hydrologic applications of active microwave remote sensing. – In Henderson, F. M. & Lewis, A. J. (eds.): *Manual of remote sensing: Principles and applications of imaging radar*. – Third edition, John Wiley & Sons, New York, USA.
- Lewis, A. J., Henderson, F. M. & Holcomb, D. W., 1998: Radar fundamentals: The geoscience perspective. – In Henderson, F. M. & Lewis, A. J. (eds.): *Manual of remote sensing: Principles and applications of imaging radar*. – Third edition, John Wiley & Sons, New York, USA.
- Li, C. H. & Lee, C. K., 1993: Minimum cross entropy thresholding. – *Pattern Recognition*, 26 (4): 617–625.
- Li, S. Z., 2009: Markov random field modeling in image analysis – Third edition, Springer-Verlag, London, UK.
- Lillesand, T. M., Kiefer, R. W. & Chipman, J. W., 2004: Remote sensing and image interpretation. – Fifth edition, John Wiley & Sons, New York, USA.

- Liu, D., Song, K., Townshend, J. & Gong, P., 2008: Using local transition probability models in Markov random fields for forest change detection. – *Remote Sensing of Environment*, 112: 2222–2231.
- Lopes, A., Nezry, E., Touzi, R. & Laur, H., 1990: Maximum a posteriori speckle filtering and first order texture models in SAR images. – *International Geoscience and Remote Sensing Symposium*, Washington D.C., USA, 2409–2412.
- Lu, D., Mausel, P., Brindizio, E. & Moran, E., 2004: Change detection techniques. – *International Journal of Remote Sensing*, 25 (12): 2365–2407.
- Lucchese, L. & Mitra, S. K., 1998: An algorithm for unsupervised color image segmentation. – *Proceedings of the IEEE 2nd Workshop on Multimedia Signal Processing*, Redondo Beach, USA, 33–38.
- Luetzgen, M., Karl, W. & Willsky, A., 1994: Efficient multiscale regularization with applications to the computation of optical flow. – *IEEE Transactions on Image Processing*, 3 (1): 41–64.
- Malladi, R., Sethian, J. & Vemuri, B., 1995: Shape modeling with front propagation: A level set approach. – *IEEE Transactions on Pattern Analysis and Machine Intelligence*, 17 (2): 158–175.
- Malnes, E., Guneriusson, T. & Høgda, K. A., 2002: Mapping of flood-area by RADARSAT in Vannsjø, Norway. – *Proceedings of the 29th International Symposium on Remote Sensing of the Environment*, Buenos Aires, Argentina.
- Marinelli, L., Michel, R., Beaudoin, A. & Astier, J., 1997: Flood mapping using ERS tandem coherence image: a case study in south France. – *Proceedings of the 3rd ERS Symposium*, Florence, Italy, 531–536.
- Martinis, S., Twele, A. & Voigt, S., 2009: Towards operational near real-time flood detection using a split-based automatic thresholding procedure on high resolution TerraSAR-X data. – *Natural Hazards and Earth System Sciences*, 9: 303–314.
- Martinis, S., Twele, A. & Voigt, S., 2011: Unsupervised extraction of flood-induced backscatter changes in SAR data using Markov image modeling on irregular graphs. – *IEEE Transactions on Geoscience and Remote Sensing*, in print.
- Mas, J. F., 1999: Monitoring land-cover changes: A comparison of change detection techniques. – *International Journal of Remote Sensing*, 20 (1): 139–152.
- Mason, D. C. & Davenport, I. J., 1996: Accurate and efficient determination of the shoreline in ERS-1 images. – *IEEE Transactions on Geoscience and Remote Sensing*, 34 (5): 1243–1253.
- Mason, D. C., Horritt, M. S., Dall'Amico, J. T., Scott, T. R. & Bates, P. D., 2007: Improving river flood extent delineation from synthetic aperture radar using airborne laser altimetry. – *IEEE Transactions on Geoscience and Remote Sensing*, 45 (12): 3932–3943.
- Mason, M. S., Speck, R., Schumann, G., Neal, J. & Bates, P. D., 2008: Using TerraSAR-X data for improved urban flood model validation. – *Proceedings of the 3rd TerraSAR-X Science Team Meeting*, Oberpfaffenhofen, Germany.
- Mason, D. C., Speck, R., Devereux, B., Schumann, G. J.-P., Neal, J. C. & Bates, P. D., 2010: Flood detection in urban areas using TerraSAR-X. – *IEEE Transactions on Geoscience and Remote Sensing*, 48 (2): 882–894.
- Matgen, P., Henry, J. B., Pappenberger, F., De Fraipont, P., Hoffmann, L. & Pfister, L., 2004: Uncertainty in calibrating flood propagation models with flood boundaries observed from synthetic aperture radar imagery. – *Proceedings of the 20th Congress of the International Society of Photogrammetry and Remote Sensing*, Istanbul, Turkey, 352–358.

- Matgen, P., Schumann, G., Henry, J. B., Hoffmann, L. & Pfister, L., 2007: Integration of SAR derived river inundation areas, high precision topographic data and a river flow model toward near real-time flood management. – *International Journal of Applied Earth Observation and Geoinformation*, 9 (3): 247–263.
- McMillan, A. Morley, J. G., Adams, B. J. & Chesworth, S., 2006: Identifying optimal SAR imagery specifications for urban flood monitoring: A hurricane Katrina case study. – 4th International Workshop on Remote Sensing for Disaster Response, Magdalene College, Cambridge.
- Meinel, G., Neubert, M. & Reder, J., 2001: The potential use of very high resolution satellite data for urban areas – First experiences with IKONOS data, their classification and application in urban planning and environmental monitoring. – *Proceedings of Regensburger Geographische Schriften*, 35: 196–205.
- Meinel, G. & Neubert, M., 2004: A comparison of segmentation programs for high resolution remote sensing data. – *Proceedings of the 20th Congress of the International Society of Photogrammetry and Remote Sensing*, Istanbul, Turkey, 1097–1102.
- Melack, J. M. & Wang, Y., 1998: Delineation of flooded area and flooded vegetation in Balbina Reservoir (Amazonas, Brazil) with synthetic aperture radar. – *Verhandlungen Internationale Vereinigung für Limnologie*, 26: 2374–2377.
- Melgani, F., Moser, G. & Serpico, S. B., 2002: Unsupervised change detection methods for remote sensing images. – *Optical Engineering*, 41 (12): 3288–3297.
- Melgani, F. & Serpico, S. B., 2003: A Markov random field approach to spatio-temporal contextual image classification. – *IEEE Transactions on Geoscience and Remote*, 41 (11): 2478–2487.
- Miasnikov, A. D., Rome, V. & Haralick, R. M., 2004: A hierarchical projection pursuit clustering algorithm. – *Proceedings of the 17th International Conference on Pattern Recognition*, Cambridge, UK, 268–271.
- Milly, P. C. D., Wetherald, R. T., Dunne, K. A. & Delworth, T. L., 1987: Increasing risk of great floods in a changing climate. – *Nature*, 415: 514–517.
- Moser, G. & Serpico, S. B., 2006: Generalized minimum-error thresholding for unsupervised change detection from SAR amplitude imagery. – *IEEE Transactions on Geoscience and Remote Sensing*, 44 (10): 2972–2982.
- Moser, G. & Serpico, S. B., 2009: Unsupervised change detection from multichannel SAR data by Markovian data fusion. – *IEEE Transactions on Geoscience and Remote Sensing*, 47 (7): 2114–2128.
- Mota, G. L. A., Feitosa, R. Q., Coutinho, H. L. C., Liedtke, C. E., Müller, S., Pakzad, K. & Meirelles, M. S. P., 2007: Multitemporal fuzzy classification model based on class transition possibilities. – *ISPRS Journal of Photogrammetry and Remote Sensing*, 62 (1): 186–200.
- Mouchot, M.-C. & Garello, R., 1998: SAR for Oceanography. – In Henderson, F. M. & Lewis, A. J. (eds.): *Manual of remote sensing: Principles and applications of imaging radar*. – Third edition, John Wiley & Sons, New York, USA.
- Moughinis-Mark, P. J., Gaddis, L. R. & Ferall, C., 1984: The Mississippi river delta: the monitoring of coastal processes with spaceborne and airborne radar and multispectral experiments. – *Proceedings of the International Symposium on Remote Sensing of the Environment*, Colorado, USA, 875–884.
- Mudelsee, M., Börngen, M., Tetzlaff, G. & Grünewald, U., 2003: No upward trends in the occurrence of extreme floods in Central Europe. – *Nature*, 425: 166–169.
- Neubert, M. & Herold, H., 2008: Assessment of remote sensing image segmentation quality. – *Proceedings of GEO-Object-Based Image Analysis*, Calgary, Canada.

- Neubert, M. Herold, H. & Meinel, G., 2006: Evaluation of remote sensing image segmentation quality - Further results and concepts. – *The International Archives of the Photogrammetry, Remote Sensing and Spatial Information Science*, XXXVI (4): Vienna, Austria, 6–11.
- Nghiem, S. V., Liu, W. T., Tsai, W.-Y. & Xie, X., 2000: Flood mapping over the Asian continent during the 1999 summer monsoon season. – *Proceedings of the IEEE International Geoscience and Remote Sensing Symposium*, Honolulu, Hawaii, 2027–2028.
- Nico, G., Pappalepore, M., Pasquariello, G., Refice, S. & Samarelli, S., 2000: Comparison of SAR amplitude vs. coherence flood detection methods – a GIS application. – *International Journal of Remote Sensing*, 21 (8): 1619–1631.
- Niedermeier, A., Hoja, D. & Lehner, S., 2005: Topography and morphodynamics in the German Bight using SAR and optical remote sensing data. – *Ocean Dynamics*, 55 (2): 100–109.
- Oberstadler, R., Honsch, H. & Huth, D., 1997: Assessment of the mapping capabilities of ERS-1 SAR data for flood mapping: A case study of Germany. – *Hydrological Processes*, 10 (10): 1415–1425.
- Oliver, C. & Quegan, S., 1998: *Understanding Synthetic Aperture Radar images*. – Artech House, London, UK.
- Ormsby, J. P., Blanchard, B. J. & Blanchard, A. J., 1985: Detection of lowland flooding using active microwave systems. – *Photogrammetric Engineering and Remote Sensing*, 51 (3): 317–328.
- Pal, N. R. & Pal, S. K., 1993: A review on image segmentation techniques. – *Pattern Recognition*, 26 (9): 1277–1294.
- Palmer, T. N. & Räisänen, 2002: Quantifying the risk of extreme seasonal precipitation in a changing climate. – *Nature*, 415: 512–514.
- Pappenberger, F., Frodsham, K., Beven, K., Romanowicz, R. & Matgen, P., 2007: Fuzzy set approach to calibrating distributed flood inundation models using remote sensing observations. – *Hydrology and Earth System Sciences*, 11 (2): 739–752.
- Peng, W., Pan, C. & Prinnet, V., 2004: Unsupervised change detection for flood analysis in SAR images. – *Proceedings of the 6th Asian Conference on Computer Vision*, Jeju Island, Korea, 652–657.
- Pérez, P., Chardin, A. & Laferté, J. M., 2000: Noniterative manipulation of discrete energy-based models for image analysis. – *Pattern Recognition*, 33 (4): 573–586.
- Pierdicca, N., Chini, M., Pulvirenti, L. & Macina, F., 2008: Integrating physical and topographic information into a fuzzy scheme to map flooded area by SAR. – *Sensors*, 8: 4151–4164.
- Pope, K. O., Rey-Benayas, J. M. & Paris, J. F., 1994: Radar remote sensing of forest and wetland ecosystems in the Central American tropics. – *Remote Sensing of Environment*, 48: 205–219.
- Provost, J.-N., Collet, C., Rostaing, P., Pérez, P. & Bouthemy, P., 2004: Hierarchical Markovian segmentation of multispectral images for the reconstruction of water depth maps. – *Computer Vision and Image Understanding*, 93 (2): 155–174.
- Ramsey, E. W., 1995: Monitoring flooding in coastal wetlands by using radar imagery and ground-based measurements. – *International Journal of Remote Sensing*, 16 (13): 2495–2502.
- Raney, R. K., 1998: Radar fundamentals: Technical perspective. – In Henderson, F. M. & Lewis, A. J. (eds.): *Manual of remote sensing: Principles and applications of imaging radar*. – Third edition, John Wiley & Sons, New York, USA.

- Rao, B. R. M., Dwivedi, R. S., Kushwaha, S. P. S., Bhattacharya, S. N., Anand, J. B. & Dasgupta, S., 1999: Monitoring the spatial extent of coastal wetlands using ERS-1 SAR data. – *International Journal of Remote Sensing*, 20 (13): 2509–2517.
- Rémi, A. & Hervé, Y., 2007: Change detection analysis dedicated to flood monitoring using ENVISAT Wide Swath mode data. – *Proceedings of the ENVISAT Symposium 2007*, Montreux, Switzerland, SP-636.
- Richards, J. A., Woodgate, P. W. & Skidmore, A. K., 1987: An explanation of enhanced radar backscattering from flooded forests. – *International Journal of Remote Sensing*, 8 (7): 1093–1100.
- Saatchi, S. S., Nelson, B., Podest, E. & Holt, J., 2000: Mapping land cover types in the Amazon Basin using 1 km JERS-1 mosaic. – *International Journal of Remote Sensing*, 21 (6-7): 1201–1234.
- Sahoo, P. K., Soltani, S. & Wong, A. K. C., 1988: A survey of thresholding techniques. *Computer Vision, Graphics, and Image Processing*, 41 (2): 233–260.
- Sanjal, J. & Lu, X. X., 2003: Application of remote sensing in flood management with special reference to Monsoon Asia: A Review. – *Natural Hazards*, 33: 283–301.
- Sarti, F., Inglada, J., Landry R. & Pultz, T., 2001: Risk management using remote sensing data: moving from scientific to operational applications. – *Proceedings of the X Simpósio Brasileiro de Sensoriamento Remoto*, Foz do Iguaçu, Brasil.
- Schreier, G., 1993: Geometrical properties of SAR images. – In Schreier, G. (ed.): *SAR geocoding: Data and Systems*, Wichmann-Verlag, Karlsruhe, Germany.
- Schumann, G., Black, A., Cutler, M., Henry, J. B., Hoffmann, L., Matgen, P. & Pfister, L., 2006: Hydraulic and event knowledge to reduce the positional uncertainty in SAR flood images for improved flood model calibration and development. – *Proceedings of Accuracy 2006: 7th International Symposium on Spatial Accuracy Assessment in Natural Resources and Environmental Sciences*, Lisbon, Portugal, 633–642.
- Schumann, G., Hostache, R., Puech, C., Hoffmann, L., Matgen, P., Pappenberger, F. & Pfister, L., 2007: High-resolution 3-D flood information from radar imagery for flood hazard management. – *IEEE Transactions on Geoscience and Remote Sensing*, 45 (6): 1715–1725.
- Schumann, G., Baldassarre, G. D. & Paul, P. D., 2009: The utility of spaceborne radar to render flood inundation maps based on multialgorithm ensembles. – *IEEE Transactions on Geoscience and Remote Sensing*, 47 (8): 2801–2807.
- Sharifi, K. & Leon-Garcia, A., 1995: Estimation of shape parameter for generalized Gaussian distributions in subband decompositions of video. – *IEEE Transactions on Circuits and Systems for Video Technology*, 5 (1): 52–56.
- Silveira, M. & Heleno, S., 2009: Separation between water and land in SAR images using region-based level sets. – *IEEE Geoscience and Remote Sensing Letters*, 6 (3): 471–475.
- Singh, A., 1989: Digital change detection techniques using remotely-sensed data. – *International Journal of Remote Sensing*, 10 (6): 989–1003.
- Smith, L. C., 1997: Satellite remote sensing of river inundation area, stage, and discharge: A review. – *Hydrological Processes*, 11: 1427–1439.
- Smits, P. & Dellepiane, S., 1997: Synthetic aperture radar image segmentation by a detail preserving Markov random field approach. – *IEEE Transactions on Geoscience and Remote Sensing*, 35 (4): 844–857.
- Solberg, H. S., Taxt, T. & Jain, A. K., 1996: A Markov random field model for classification of multisource satellite imagery. – *IEEE Transactions on Geoscience and Remote Sensing*, 34 (1): 100–113.

- Solbø, S. & Solheim, I., 2004: Towards operational flood mapping with satellite SAR. – Proceedings of the ENVISAT/ERS Symposium 2004, Salzburg, Austria.
- Solbø, S., Pettinato, S., Paloscia, S., Santi, E., Brusotti, P. & Solheim, I., 2004: Mapping of flooding in the Alessandria area with ERS. – Proceedings of IEEE Geoscience and Remote Sensing Society 2004, Anchorage, Alaska, 4689–4692.
- Solomon, S. I., 1993: Methodological considerations for the use of ERS-1 SAR imagery for the delineation of river networks in tropical forest areas. – Proceedings of the 1st ERS-1 Symposium (SP-359), ESA/ESRIN, Frascati, Italy, 595–600.
- Swain, P. H., 1978: Bayesian classification in a time-varying environment. – IEEE Transactions on Systems, Man, and Cybernetics, 8 (12): 879–833.
- Touzi, R., Lopes, A. & Bousquet, P., 1988: A statistical and geometrical edge detector for SAR images. – IEEE Transactions on Geoscience and Remote Sensing, 26 (6): 764–773.
- Townsend, P. A. & Walsh, S. J., 1998: Modeling floodplain inundation using an integrated GIS with radar and optical remote sensing. – *Geomorphology*, 21: 295–312.
- Townsend, P. A., 2001: Mapping seasonal flooding in forested wetlands using multi-temporal RADARSAT SAR. – *Photogrammetric Engineering and Remote Sensing*, 67: 857–864.
- Townsend, P. A., 2002: Relationships between forest structure and the detection of flood inundation in forest wetlands using C-band SAR. – *International Journal of Remote Sensing*, 23 (3): 332–460.
- Tso, B. & Olsen, C., 2005: Combining spectral and spatial information into hidden Markov models for unsupervised image classification. – *International Journal of Remote Sensing*, 26 (10): 2113–2133.
- Ulaby, F. T., Moore, R. K. & Fung, A. K., 1982: *Microwave Remote Sensing: Active and passive. Vol. II – Radar remote sensing and surface scattering and emission theory.* – Addison-Wesley Publishing Company, Advanced Book Program, Reading, Massachusetts, USA.
- Ulaby, F. T., Moore, R. K. & Fung, A. K., 1986: *Microwave Remote Sensing: Active and Passive. Vol. III – From theory to applications.* – Artech House, Dedham, Massachusetts, USA.
- Van der Sande, C. J., de Jong, S. M. & De Roo, A. P. J., 2003: A segmentation and classification approach of IKONOS-2 imagery for land cover mapping to assist flood risk and flood damage assessment. – *International Journal of Applied Earth Observation and Geoinformation*, 4: 217–229.
- Voigt, S., Kemper, T., Riedlinger, T., Kiefl, R., Scholte, K. & Mehl, H., 2007: Satellite image analysis for disaster and crisis-management support. – *IEEE Transactions on Geoscience and Remote Sensing*, 45 (6): 1520–1528.
- Vos, F., Rodriguez, J., Below, R. & Guha-Sapir, D., 2010: Annual disaster statistical review 2009: The numbers and trends. – Centre for research on the epidemiology of disasters, Brussels, Belgium.
- Wang, Y., 2004: Seasonal change in the extent of inundation on floodplains detected by JERS-1 Synthetic Aperture Radar data. – *International Journal of Remote Sensing*, 25 (13): 2497–2508.
- Wang, Y., Colby, J. D. & Mulcahy, K. A., 2002: An efficient method for mapping flood extent in a coastal flood plain using Landsat TM and DEM data. – *International Journal of Remote Sensing*, 23 (18): 3681–3696.
- Wang, Y., Hess, L. L., Filoso, S. & Melack, J. M., 1995: Understanding the radar backscattering from flooded and non-flooded Amazonian forests: Results from canopy backscatter modeling. – *Remote Sensing of Environment*, 54: 324–332.

-
- Wang, Y. & Imhoff, M. L., 1993. Simulated and observed L-HH radar backscatter from tropical mangrove forests. – *International Journal of Remote Sensing* 14 (15): 2819–2828.
- Wegmüller, U., Werner, C. L., Nüesch, D. & Borgeaud, M., 1995: Forest mapping using ERS repeat-pass SAR interferometry. – *Earth Observation Quarterly*, 49: 4–7.
- Wilson, R. & Li, C., 2003: A class of discrete multiresolution random fields and its application to image segmentation. – *IEEE Transactions on Pattern Analysis and Machine Intelligence*, 25 (1): 42–56.
- Williams, D. J. & Shah, M., 1992: A fast algorithm for active contours and curvature estimation. – *Computer Vision Graphics and Image Processing: Image Understanding*, 55 (1): 14–26.
- Wu, S. T., 1984: Analysis of synthetic aperture radar data acquired over a variety of landcover. – *IEEE Transactions on Geoscience and Remote Sensing*, 22 (6): 550–554.
- Wu, S. T. & Sader, S. A., 1987: Multipolarization SAR data for surface feature delineation and forest vegetation characterization. – *IEEE Transactions on Geoscience and Remote Sensing*, 25 (1): 67–76.
- Yuan, J., Li, J. & Zhang, B., 2007: Exploiting spatial context constraints for automatic image region annotation. – *Proceedings of the 15th International Conference on Multimedia*, Augsburg, Bavaria, Germany, 595–604.
- Zhang, Y. J., 1996: A survey on evaluation methods for image segmentation. – *Pattern Recognition*, 29 (8): 1335–1346.

Acknowledgments

This work has been accomplished in the framework of the project SAR-HQ at the German Remote Sensing Data Center (DFD) of the German Aerospace Center (DLR) in Oberpfaffenhofen, department for Civil Crisis Information and Georisks. The financial funding of SAR-HQ by the Federal Ministry of Education and Research (BMBF) is gratefully acknowledged.

I am glad now for the opportunity to thank those people who directly and indirectly contributed to the fulfilment of this thesis.

First of all, I would like to thank Prof. Dr. Ralf Ludwig from the Department of Geography of the Ludwig-Maximilians-University Munich that he spontaneously agreed to be the first referee of my thesis during the final phase of this work. He helped me a lot to finish my dissertation.

I am very grateful to Prof. Dr. Richard Bamler (Remote Sensing Technology Institute of the DLR and Technical University Munich) for his thoughtful comments and suggestions on several aspects of my work. I am glad to have him as second referee and that he encouraged me to prepare this thesis cumulatively.

I would like to express my appreciation to Dr. Stefan Voigt, leader of DFD's/DLR's Center for Satellite based Crisis Information (ZKI) that he gave me the great possibility to work within the interesting and exciting field of natural disasters.

Additionally, many thanks to Dr. Monika Gähler, leader of the team Natural and Technical Disasters, DLR, who supported me particularly during the final phase of this thesis.

I owe special thanks to André Twele, leader of the project SAR-HQ at the DLR. He supported me with a lot of inspiration, practical help and endless time for discussions. This thesis would not be what it is without his tremendous support.

I am also very grateful to Prof. Dr. Stefan Hinz from the Technical University Karlsruhe for his scientific advice on image analysis.

I greatly appreciate the friendly spirit at my working place and would like to thank all my colleagues of the team Natural and Technical Disasters, former Crisis Information and Emergency Mapping, for the excellent working atmosphere. Special thanks go to all my former office roommates Jens Kersten, Hendrik Zwenzner, Dr. Tobias Schneiderhan, Stefan Plattner, and Martin Geyer.

Finally, I am deeply grateful to Diana and my family for their unlimited support, patience and understanding.

Curriculum Vitae

Personal:

Name: Sandro Martinis
Date of Birth: 19.08.1980
Place of Birth: Ebersberg, Germany
Nationality: German
Degree: Dipl. Geogr. (phys.)
Email: Sandro.Martinis@dlr.de

Professional Career:

Since 08/2010 Research associate at the German Aerospace Center (DLR), Oberpfaffenhofen
08/2007 – 07/2010 PhD studies at the German Aerospace Center (DLR), Oberpfaffenhofen
10/2006 – 07/2007 Research associate at the Ludwig-Maximilians-University (LMU) of Munich, Munich (Germany)
06/2005 – 08/2005 Internship at GAF AG, Munich (Germany)
08/2004 – 10/2004 Internship at the German Aerospace Center (DLR), Oberpfaffenhofen (Germany)
03/2004 – 04/2004 Internship at Vista – Remote Sensing Applications GmbH, Munich (Germany)
12/2003 – 07/2004 Student assistant at LMU Munich

Education:

09/2006 Degree in physical geography, LMU Munich
03/2006 – 09/2006 Diploma thesis: Derivation of flow dynamics of Skeiðarárjökull outlet, Iceland, by means of Terra ASTER and ENVISAT ASAR data.
10/2003 – 09/2006 Advanced studies of physical geography, remote sensing, and physics, LMU Munich
07/2010 Intermediate diploma in physical geography, LMU Munich
10/2001 – 10/2003 Basic studies of physical geography, remote sensing, and physics, LMU Munich
10/2000 – 08/2001 Civilian Service at the Environmental Agency of Vaterstetten (Germany)
1991 – 2000 Gymnasium, Vaterstetten (Germany)
1987 – 1991 Primary school, Baldham (Germany)

References:

Peer-reviewed journals

- Martinis, S. & Twele, A., 2010: A hierarchical spatio-temporal Markov model for improved flood mapping using multi-temporal X-band SAR data. – *Remote Sensing*, 2 (9), 2240-2258.
- Martinis, S., Twele, A. & Voigt, S., 2011: Unsupervised extraction of flood-induced backscatter changes in SAR data using Markov image modeling on irregular graphs. –

IEEE Transactions on Geoscience and Remote Sensing, (in print).

Martinis, S., Twele, A. & Voigt, S., 2009: Towards operational near real-time flood detection using a split-based automatic thresholding procedure on high resolution TerraSAR-X data. – *Natural Hazards and Earth System Sciences*, 9: 303-314.

Martinis, S., Scharrer, K., Münzer, U., Mayer, C. & Gudmundsson, Á., 2007: Influences of the 2004 jökulhlaup on ice dynamics of Skeiðarárjökull, Iceland, using Terra-ASTER imagery. – *Photogrammetrie, Fernerkundung und Geoinformation*, 5: 337-347.

Book chapters

Hahmann, T., Twele, A., Martinis, S. & Buchroithner, M., 2010: Strategies for the automatic extraction of water bodies from TerraSAR-X / TanDEM-X data. – In Konecny, M., Zlatanova, S. & Bandrova, T. L. (eds.): *Geographioc and Cartography for risk and crisis management*. Springer-Verlag, Berlin, Heidelberg, Germany, 129-141.

Conference papers

Hahmann, T., Martinis, S., Twele, A. & Buchroithner, M., 2009: Strategies for the automatic mapping of flooded areas and other water bodies from high resolution TerraSAR-X data. – In Konecny, M., Zlatanova, S., Bandrova, T. L. & Friedmannova, L. (eds.): *Cartography and Geoinformatics for Early Warning and Emergency Management: Towards Better Solutions*, Joint Symposium of ICA Working Group on CEWaCM and JBGIS Gi4DM "Cartography and Geoinformatics for Early Warning and Emergency Management: Towards Better Solutions", Prag, Czech Republic, 207-214.

Voigt, S., Martinis, S., Zwenzner, H., Hahmann, T., Twele, A. & Schneiderhan, T., 2008: Extraction of flood masks using satellite based very high resolution SAR data for flood management and modeling. – *Proceedings of the 4th International Symposium on Flood Defence, Managing Flood Risk, Reliability & Vulnerability*, Toronto, Canada.

Hahmann, T., Martinis, S., Twele, A., Roth, A. & Buchroithner, M., 2008: Extraction of water and flood areas from SAR data. – *7th European Conference on Synthetic Aperture Radar (EUSAR)*, Friedrichshafen, Germany, 177-180.

Hahmann, T., Roth, A., Martinis, S., Twele, A. & Gruber, A., 2008: Automatic Extraction of Water Bodies from TerraSAR-X Data. In: *IEEE International Geoscience and Remote Sensing Symposium (IGARSS) 2008*, Boston, USA.

Scharrer, K., Mayer, C., Martinis, S., Münzer, U. & Gudmundsson, Á., 2007: Ice dam fluctuations at the marginal lake Grænalón (Iceland) before and during a GLOF. – *Proceedings of ENVISAT Symposium 2007*, Montreux, Switzerland, SP-636.

Conference abstracts

Martinis, S. & Twele, A., 2010: Automatic detection of inundation-related change areas in TerraSAR-X data using Markov image modeling on irregular graphs. – *Geophysical Research Abstracts*, EGU General Assembly 2010, Vienna, Austria.